Project No. 11-3176

High Fluency Low Flux Embrittlement Models of LWR Reactor Pressure Vessel Embrittlement and a Supporting Database from the UCSB ATR-2 Irradiation Experiment

---

Reactor Concepts

G. Robert Odette
University of California, Santa Barbara

Richard Reister, Federal POC
Thomas Rosseel, Technical POC

NEUP Nuclear Energy University Programs
U.S. Department of Energy

US DOE NUCLEAR ENERGY UNIVERSITY PROGRAM

Final Report – High Fluency Low Flux Embrittlement Models of LWR Reactor Pressure Vessel Embrittlement and a Supporting Database from the UCSB ATR-2 Irradiation Experiment

Milestone: M2NU-11CA-UCSB-0304-023

Document Completed: January 24, 2016

G. R. Odette, T. Yamamoto, P. B. Wells and N. Almirall

University of California, Santa Barbara

Contents

List of Figures

List of Tables

1. FLUX EFFECTS

1.1 Introduction

Reactor pressure vessel embrittlement may limit the lifetime of light water reactors (LWR). Embrittlement is primarily caused by formation of nano-scale precipitates, which cause hardening and a subsequent increase in the ductile-to-brittle transition temperature of the steel. While the effect of Cu has historically been the largest research focus of RPV embrittlement, there is increasing evidence that Mn, Ni and Si are likely to have a large effect at higher fluence, where Mn-Ni-Si precipitates can form, even in the absence of Cu. Therefore, extending RPV lifetimes will require a thorough understanding of both precipitation and embrittlement at higher fluences than have ever been observed in a power reactor. To address this issue, test reactors that irradiate materials at higher neutron fluxes than power reactors are used. These experiments at high neutron flux can reach extended life neutron fluences in only months or several years. The drawback of these test irradiations is that they add additional complexity to interpreting the data, as the irradiation flux also plays a role into both precipitate formation and irradiation hardening and embrittlement. This report focuses on developing a database of both microstructure and mechanical property data to better understand the effect of flux. In addition, a previously developed model that enables the comparison of data taken over a range of neutron flux is discussed.

1.2 Neutron Flux Database

1.2.1 Irradiation Conditions

Table 1.1 and Table 2 show the irradiation conditions in this study from test reactor and surveillance irradiations, respectively.

Table 1.1. Primary irradiation conditions from materials test reactors.

Condition	Reactor	Neutron Flux ϕ*	Neutron Fluence ϕt*	Neutron Eff. Fluence	Dose Rate	Dose	T_{irr}
T1	U Mich.	7.8E+11	7.0E+17	8.9E+17	1.3E-09	0.001	290
T2	U Mich.	7.8E+11	1.8E+18	2.3E+18	1.3E-09	0.003	290
T3	U Mich.	7.8E+11	3.4E+18	4.3E+18	1.3E-09	0.005	290
T4	U Mich.	9.7E+11	7.5E+18	1.0E+19	1.6E-09	0.011	290
T5	U Mich.	7.8E+11	1.4E+19	1.7E+19	1.3E-09	0.020	290
T6	U Mich.	1.0E+12	3.4E+19	4.6E+19	1.7E-09	0.051	290
T11	U Mich.	2.6E+11	4.0E+17	3.9E+17	4.4E-10	0.001	290
T12	U Mich.	3.2E+11	1.0E+18	1.0E+18	5.4E-10	0.002	290
T13	U Mich.	3.1E+11	2.4E+18	2.4E+18	5.3E-10	0.004	290
T14	U Mich.	3.2E+11	4.8E+18	4.9E+18	5.4E-10	0.007	290
T15	U Mich.	2.6E+11	8.5E+18	8.2E+18	4.5E-10	0.013	290
T16	U Mich.	3.0E+11	1.6E+19	1.6E+19	5.1E-10	0.024	290
T21	U Mich.	1.0E+11	3.0E+17	2.3E+17	1.7E-10	0.000	290

T22	U Mich.	1.0E+11	1.1E+18	8.4E+17	1.7E-10	0.002	290
T23	U Mich.	8.4E+10	2.4E+18	1.7E+18	1.4E-10	0.004	290
T24	U Mich.	8.4E+10	4.0E+18	2.9E+18	1.4E-10	0.006	290
G1	BR2	1.0E+14	1.3E+20	3.0E+19	1.5E-07	0.2	300
TU	BR2	3.0E+13	2.5E+20	7.9E+19	4.5E-08	0.38	290
ATR1	ATR	2.3E+14	1.1E+21	2.1E+20	3.4E-07	1.66	290
ATR2	ATR	3.6E+12	1.2E+20	6.5E+19	5.4E-09	0.18	290

*For neutron energies > 1 MeV

Table 1.2. Surveillance program irradiation conditions.

Condition	Reactor	Neutron Flux* (n/cm2/s)	Neutron Fluence* (n/cm2)	Dose Rate (dpa/s)	Dose (dpa)	T_{irr} (°C)
N	Ringhals	1.49E+11	6.03E+19	2.24E-10	0.09	284

*For neutron energies > 1 MeV

1.2.2 Mechanical Property Measurements

1.2.2.1 Tensile Testing

SSJ-2 type tensile specimens, shown in Figure 1.1, are nominally 16 mm long with a gauge section width of 1.2 mm and thickness of 0.5 mm. It should be noted that approximately half of the specimens have a nominal gauge length of 5.0 mm, while the others have a 2.2 mm gauge length. No significant differences in the tensile properties have been observed between the two gauge lengths. Groups of ≈ 18 specimens were loaded in boxes designed to maximize heat transfer.

The dog-bone tensile specimens are clamped by grips in an alignment fixture prior to placement in on an MTS 810 load frame. The specimens were loaded at a rate of 0.008 mm/s at strain rates of 0.002 to 0.003/min. Standard engineering stress-strain curves are recorded based on precise measurements of the width and thickness of the gauge section of individual specimens. A best fit to the elastic loading region is used to establish the 0.2% offset yield stress ($\sigma_y \approx s_y$). The ultimate engineering stress (s_u) at maximum load is also recorded. The tensile tests on irradiated specimens are generally stopped at a load that is ≈ 70% of the maximum to keep the specimen intact.

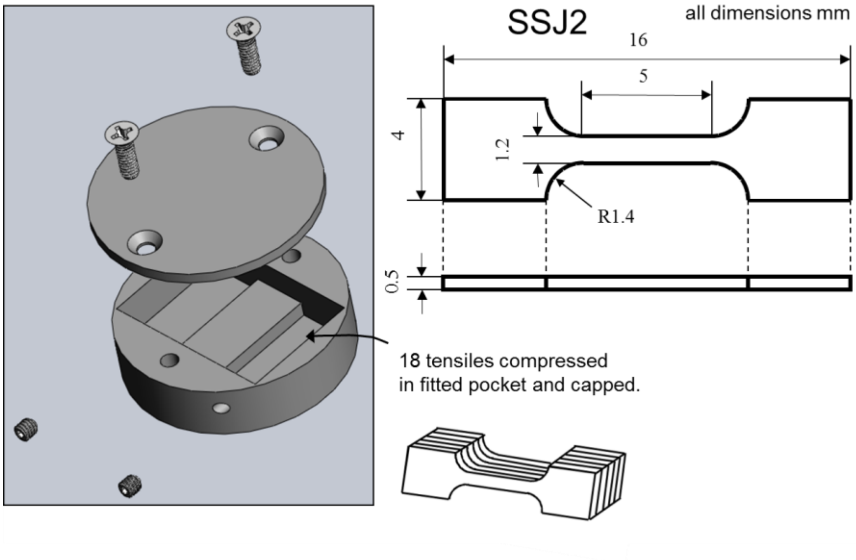

Figure 1.1. Schematic of the tensile loading box (left) and SSJ-2 tensile specimens (right). Note that half of the specimens have a gauge length of 5.00 mm (showed), while the others have a 2.2 mm gauge length.

1.2.2.2 Microhardness Testing

Microhardness tests at UCSB were carried out on a Leco M400 hardness tester with at least 10 indents per sample at a load of 500 grams. The mean and standard error were calculated for the hardness of each alloy in both the baseline and irradiated conditions. For the high flux irradiations, the as irradiated hardness was taken after a mild post irradiation anneal at 350°C for 5 h to remove the thermally unstable damage that is associated only with high flux [1, 3, 5]. The yield stress increase was estimated using the relation $\Delta\sigma_y \approx 3.3\Delta H_v$. The uncertainty in the $\Delta\sigma_y$ was calculated from the root mean square of the standard errors of the baseline and as irradiated measurements.

1.2.3 Microstructural Characterization

In order to measure precipitation the complementary experimental techniques of Atom Probe Tomography (APT) and Small Angle Neutron Scattering (SANS) were utilized. A particular focus of these techniques was measuring the volume fraction, size, number density and composition of embrittling precipitates that form under irradiation. APT also enables the quantitative and qualitative observation of Radiation Induced Segregation (RIS) effects to other microstructural features such as grain boundaries, dislocations and dislocation loops.

1.2.3.1 Atom Probe Tomography

Atom probe tomography (APT) is a destructive microscopy technique that measures compositional distributions on the nano-scale, including precipitates and solute segregation. An APT specimen is fabricated, by electropolishing or FIB milling (FIBing), a needle typically ≈ 100 nm in diameter with a smoothly rounded tip. The needle is then mounted on a stage in an atom probe, in this case a Local Electrode Atom Probe (LEAP), in ultrahigh vacuum ($< 10^{-10}$ torr) and cooled to cryogenic temperatures (20-60K). In LEAPs, a high voltage electrode is located close to the needle tip to create a very high local electric field at the needle tip. A standing voltage is applied that is just below that needed to electrostatically evaporate the atoms from the tip surface, where the field is highly concentrated. High frequency voltage pulses (100-200 kHz) are then used to increase the field to the point that there is a significant probability that a tip atom will be ionized and evaporated, typically at a steady rate of 0.2-0.5% per pulse, that can be controlled by modifying the standing voltage. The tip is sequentially evaporated along the needle axis until a sufficient number of ions are collected or the tip breaks, which is often the case.

The evaporated ions are accelerated by the electric field and pass through an aperture in the local electrode prior to being individually counted by a position sensitive detector. The position of the on the detector is determined by the x-y timing of a voltage pulse in the cross wire detector after charge amplification by a microchannel plate. A schematic of a LEAP is tip-electrode configuration is shown in Figure 1.2.

The time-of-flight between the voltage pulse causing evaporation and detection is used to determine the field emitted ion's mass-to-charge ratio, which is specific, with some overlaps, to a particular element and isotope. The detector position is used to determine the ion's location on the tip surface based on application of simple electrostatic field optics to a perfectly rounded needle tip. If ions evaporate prior to or slightly after the peak of the voltage pulse, then they acquire slightly less energy than those that evaporate at the peak voltage. Thus, there is a spread in the time-of-flight and corresponding mass-to-charge ratio spectrum. The LEAPs used for this report are equipped with so-called reflectrons, which alter the flight paths of ions with varying energies, and significantly reduce spread in the time-of-flight, thus improving mass resolution. The drawback to the high mass resolution instruments is that some ions are lost in the reflectron, reducing the collection efficiency from ≈ 65% to 37%.

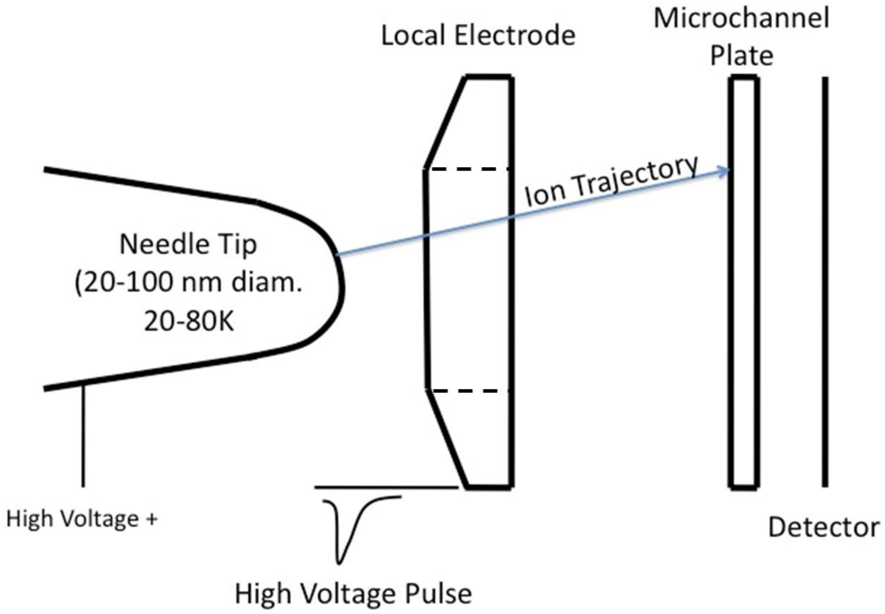

Figure 1.2 Schematic of a Local Electrode Atom Probe. Note that it is not to scale [6].

Three-dimensional (3D) reconstruction of the atomic positions is carried out with a proprietary software package, here the Cameca Integrated Visualization and Analysis Software (IVAS) by assuming there is a uniform layer-by-layer removal of atoms from the tip. After each ion is evaporated, the associated volume is divided by the area of the evaporating surface within the field of view of the detector, incrementally changing the needle length in the z-direction, hence the position of the reconstructed tip surface. The next ion that evaporates is assumed to come from the repositioned surface. By continuously repeating this process a full 3D map of the element specific map of the atomic positions can be created. Note field emission of multi-atom/element ions is common, as is multiple ion charge to mass ratios for a particular isotope.

The resulting 3-dimensional datasets are then used to measure spatial distribution of the solutes, in this case the precipitates formed under irradiation. Precipitates are characterized by IVAS cluster analysis algorithms. The basic premise is that the atomic density of solute atoms is higher in precipitates than in the matrix. First, the distance (d) between specific solutes, here Cu, Ni, Mn and Si, and their Nth nearest solute neighbor is found, where the Nth atom is defined as the order (K). If d is less than a cutoff distance defined by the user (d_{max}), the solute is considered to be a core atom. After all core has been defined, all atoms within d_{max}, even those that are not solutes, are considered to be in the cluster. Clusters that have fewer than N_{min} atoms are excluded from the analysis. In addition to characterizing the precipitate size distribution, <r>, N and f_p, APT also measures the local bulk, matrix and precipitate compositions. Note the typical maximum volume of a sampled tip is less than 600,000 nm^3, equivalent to $\approx$ 50 million atoms. Nanoscale precipitation is governed by the local tip composition, which is seldom completely uniform from tip to tip. However, fluctuations in local compositions can be exploited to establish the relation between the alloy composition and the characteristics of the precipitates. For example, in this work the f_p closely tracks the local alloy Cu, Ni, Mn and Si contents. However, APT may not be practically applicable to highly heterogeneous materials, or when number of feature of interest is low in the sampled tip volume. Of course many tips can be examined, but beyond a point this becomes impractical, especially in the cases of activated materials.

While APT is arguably the best tool for measuring the detailed nature of the precipitates that form under irradiation, the data must be cautiously interpreted in the face of a number of measurement artifacts. The most significant artifact is so-called trajectory aberrations. Trajectory aberrations are due to flattened or dimpled regions that form around a precipitate, deviating from an ideally rounded tip. In the case of RPV steels the deviation in local curvature causes surrounding matrix atoms to be focused onto the detector in the precipitate region. The flattened or dimpled region is caused by the lower potential needed to evaporate the precipitate solutes compared to the surrounding Fe matrix. Non-physically high precipitate atomic densities, which can be as high as 3 to 4 times that of the surrounding bcc matrix, signal trajectory aberrations. The reconstruction algorithm does not have any information on the incoming ion trajectory, only the location they hit the detector. As a result both focused matrix and actual precipitate solutes are reconstructed as if they originated from the same tip region. Although significant progress has been made in understanding trajectory aberrations, and other APT artifacts, this knowledge has not been converted to a standard practice and improving the fidelity of APT reconstructions is still work in progress. In this report, all Fe that is nominally reconstructed in a precipitate is treated as an artifact and excluded from compositional and size measurements.

APT needle preparation was performed at the Center for Advanced Energy Studies (CAES) Microscopy and Characterization Suite (MaCS) using their Focused Ion Beam dedicated to working with activated specimens. After liftouts were created, they were welded to posts on a 22 grid coupon and partially sharpened to minimize the activated material on the coupon. The coupons were then shipped to UCSB where the final tip shaping was completed. A Cameca LEAP 3000X HR was used to run all samples using voltage mode with a 20% pulse fraction, a detection rate of 0.4 to 0.8%/pulse and a specimen temperature < 50K.

1.2.3.2 Small Angle Neutron Scattering

Small Angle Neutron Scattering (SANS) is based on coherent scattering of cold neutrons by atomic nuclei around the $\theta = 0$, Bragg peak. In the case of solute rich precipitates embedded in a solvent rich matrix, the coherent scattering cross section, $d\Sigma/d\Omega$, is a function of θ, or more precisely the scattering vector, $q = 4\pi\sin\theta/\lambda$, where λ is the neutron (or x-ray) wavelength. As shown in Figure 1.3, 2θ is the angle between the incident beam and detector x-y position. The magnitude $d\Sigma/d\Omega(q)$ depends on the square of the coherent scattering length density difference between the matrix and precipitate. The coherent nuclear scattering length (b) is a property of a specific nuclear isotope. The coherent magnetic b is a function of the atomic magnetization of in the precipitate or matrix phase. Scattering length density (SLD), ρ, is the product of the atomic density and the scattering length, usually taken as the averages for the matrix and precipitate, respectively. The amplitude of $d\Sigma/d\Omega(q)$ is a function of $\Delta\rho^2$ between the matrix and precipitate, and the corresponding q dependence is a function of the size, or size distribution, of the precipitates. The $d\Sigma/d\Omega(q)$ generally scales with $(1/qr)^2$, hence, smaller precipitates produce scattering at higher q. This makes it relatively easy to characterize nm-scale precipitates formed during irradiation in a matrix phase that is would otherwise be free of features in this size range in the unirradiated condition. The precipitate scattering is reflected in the difference between irradiated (with nano precipitates) versus unirradiated (without nano precipitates) steels. If $\Delta\rho^2$ is known, SANS can be used to determine the precipitate size distribution, $<r_p>$, N_p and f_p.

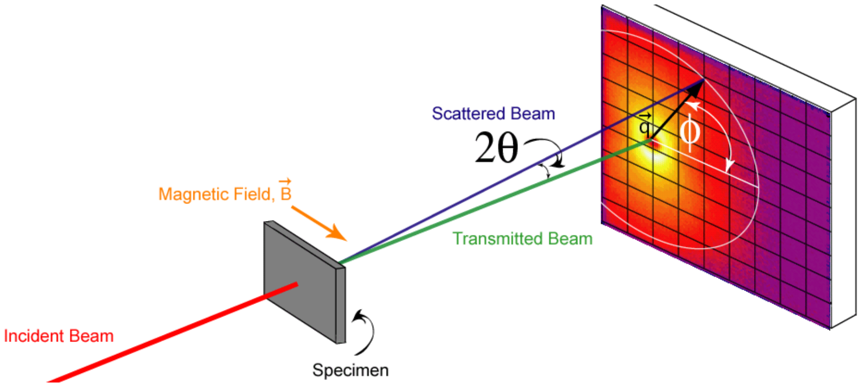

Figure 1.3 SANS experimental setup.

SANS (and SAXS) measures the number of scattered neutron counts, I, at a detector position at q and ϕ where ϕ is the azimuthal angle around the beam, $I(q,\phi)$, for a specified total beam fluence on the specimen. The total $I(q,\phi)$ for the steel is isolated by appropriate adjustments for background and beam attenuation. The corresponding precipitate $I_p(q,\phi)$ is found by subtracting an unirradiated (nano precipitate free) control. The $I_p(q,\phi)$ is then converted to a $d\Sigma/d\Omega(q,\phi)_p$, using a known isotropic scattering standard, in this case water.

Precipitates in ferromagnetic Fe produce both nuclear (N) and magnetic (M) small angle scattering, depending on their respective SLD. The nuclear SLD depends on the precipitate and matrix compositions that are not known a priori, so $\Delta\rho_n^2$ is also unknown. However, the Cu, Mn, Ni, Si solute rich precipitates are believed to be non-magnetic, or only weakly magnetic. Thus when the Fe matrix is magnetically fully saturated with a known magnetic SLD, $\Delta\rho_m^2$, the $d\Sigma/d\Omega(q)_m$ is known. The magnitude of the magnetic scattering varies with $\sin(\phi)^2$, ranging from 0 parallel to 1 perpendicular to the magnetic field, respectively. In practice, a fitted magnetic to nuclear scattering ratio (M/N) is used to convert the data at all ϕ to a magnetic scattering cross section, that is then fit to extract the precipitate size distribution $<r_p>$, N_p and f_p.

SANS measurements were carried on out the NG7 beam line at the National Institute of Standards and Technology Center for Neutron Research. Small (dimensions) coupons were mounted in an automated sample changer in a 1.5 T horizontal magnetic field. The average neutron wavelength was 5 Å. A 2D ^{3}He detector measured the scattering intensity, I, as a function of q and ϕ. The $I(q, \phi)$ are measured for both unirradiated controls, that do not contain nano precipitates, and the irradiated steels. The $I(q,\phi)$ are corrected and normalized to one another by background subtraction and transmission measurements, as well as adjustments for different sample volumes probed by the neutron beam; the differences are generally minimal. Variations in detector pixel efficiencies are accounted for in converting $I_p(q, \phi)$ the to an absolute $d\Sigma/d\Omega(q)_{n/m}$ differential scattering cross-sections using a isotropic scattering water standard. After conversion of the entire set of detector cross sections to an equivalent $d\Sigma/d\Omega(q)_m$, the data are least square fit using the assumed $\Delta\rho_m^2$ and a spherical q-dependent form factor and log normal size distribution. The fitting parameters are the precipitate size-distribution mode radius (r_m) and width parameter (β) and $d\Sigma/d\Omega(0)_m$. The fitted parameters are then used to calculate the precipitate $<r>$, N_p and f_p. Multiple scattering features can be fit simultaneously. Multiple feature fits are also used to remove scattering artifacts due to experimental uncertainties and bias. Finally we note that scattering at very high the q is due to an essentially isotropic incoherent background from various sources, but discussion is beyond the scope of this report. The irradiated and unirradiated $d\Sigma/d\Omega(q)$ are approximately the same at high q which is a useful check on the data. The major difference is due to the removal of solutes from the matrix by precipitation that can be readily accounted for is necessary. Further details regarding SANS theory, experimental details and data analysis can be found elsewhere [3, 6–9].

The major assumption in the SANS analysis is that the precipitates are non-magnetic. This assumption has been shown to be valid for Cu rich precipitates that are dominant at lower fluence. However, this assumption may not be valid at high fluences where Mn, Si and most importantly, Ni, are the dominant solutes in the precipitates. Specifically, if the precipitates are partially magnetic, then the magnetic scattering contrast, $\Delta\rho_m^2$, assumed in the analysis is too large, resulting in an underestimate of the precipitate f_p and N_p. Work is ongoing to address this issue, including magnetic property measurements of the bulk precipitate phases, as well as SANS measurements at various temperatures.

1.3 Flux Effects & Effective Fluence model

The main effect of concern with regards to increasing ϕ is a delay in precipitation and hardening to a higher ϕt. This is illustrated Figures 4-9 for (a) irradiation hardening, represented by an equivalent change in yield stress ($\Delta\sigma_y$), and (b) precipitate volume fractions (f_v) in various split melt steels plotted as a function of the square root of fluence (ϕt) for low ϕ irradiations in the previous UCSB Irradiation Variables (IVAR) Program and high ϕ BR2 irradiations [29]. The delay in both precipitation and hardening with increasing ϕ is obvious.

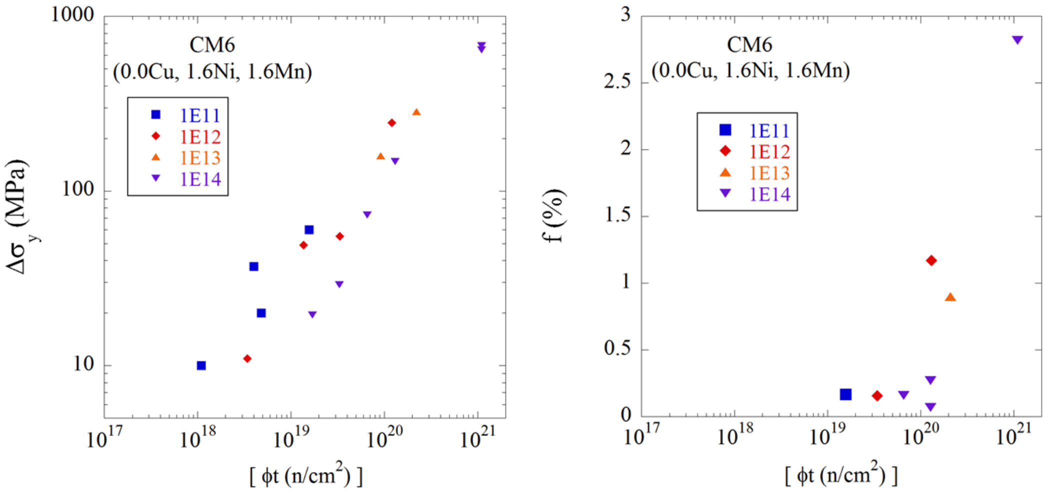

Figure 1.4. $\Delta\sigma_y$ (left) and f (right) as a function of fluence for the 0.01% Cu, 1.6% Ni alloy CM6 for irradiations over a range of neutron flux.

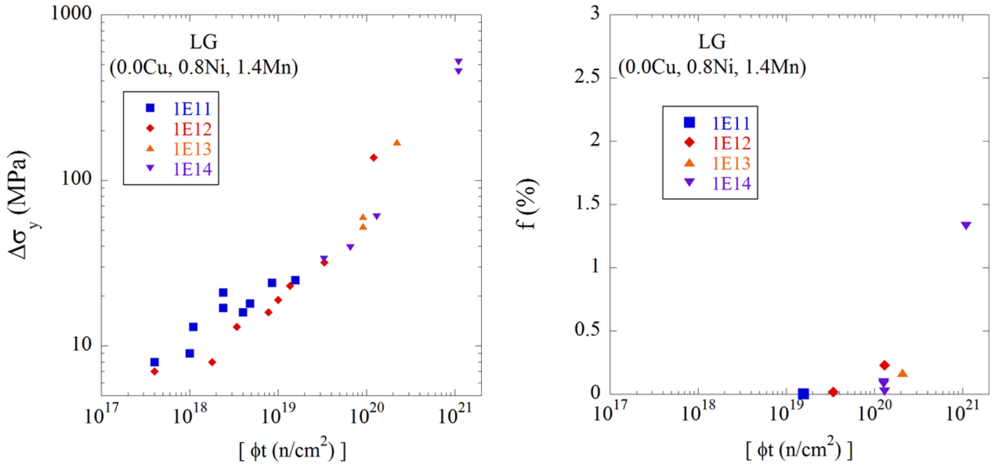

Figure 1.5. Δσy (left) and f (right) as a function of fluence for the 0.01% Cu, 0.8% Ni alloy LG for irradiations over a range of neutron flux.

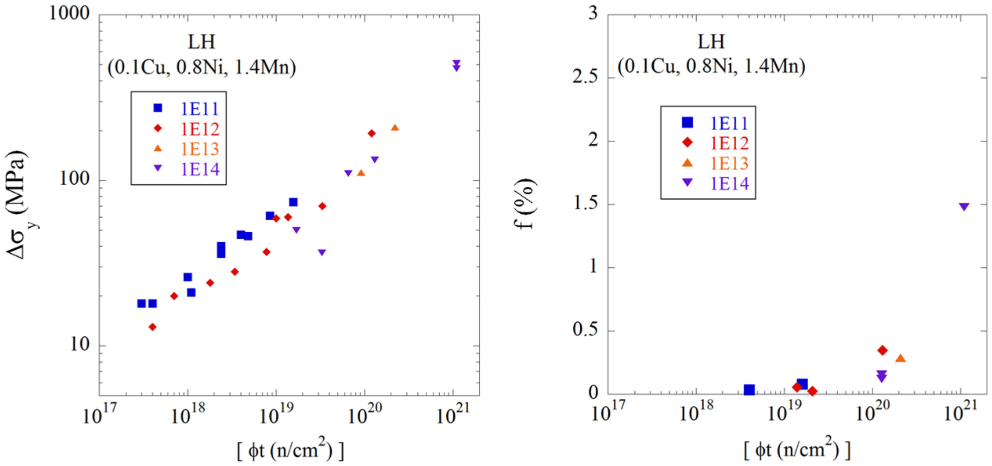

2

Figure 1.6. Δσy (left) and f (right) as a function of fluence for the 0.1% Cu, 0.8% Ni alloy LH for irradiations over a range of neutron flux.

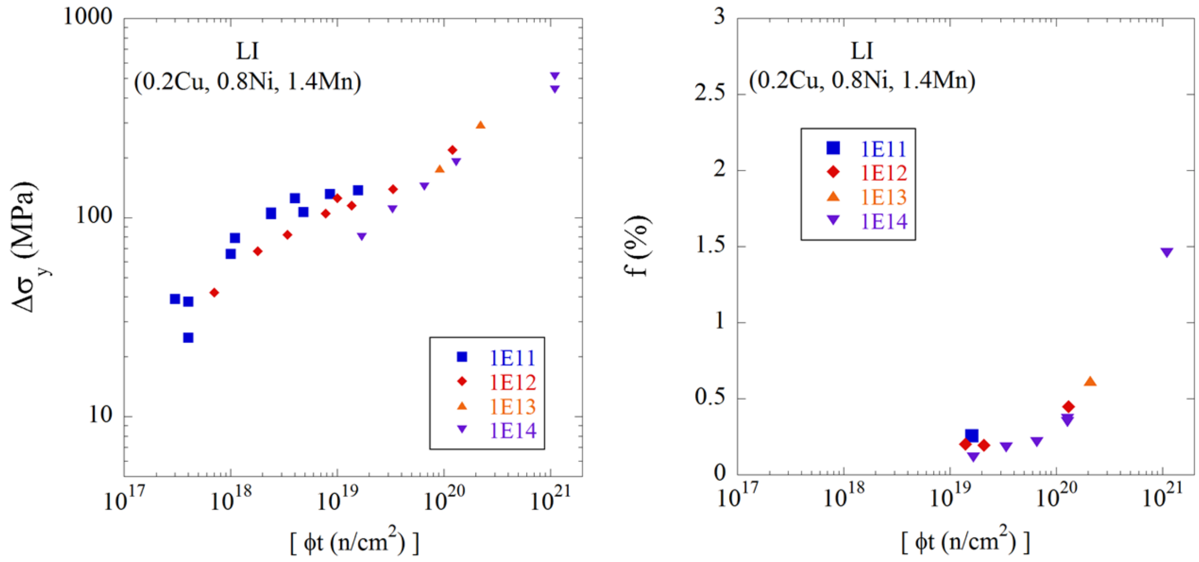

Figure 1.7. Δσy (left) and f (right) as a function of fluence for the 0.2% Cu, 0.8% Ni alloy LI for irradiations over a range of neutron flux.

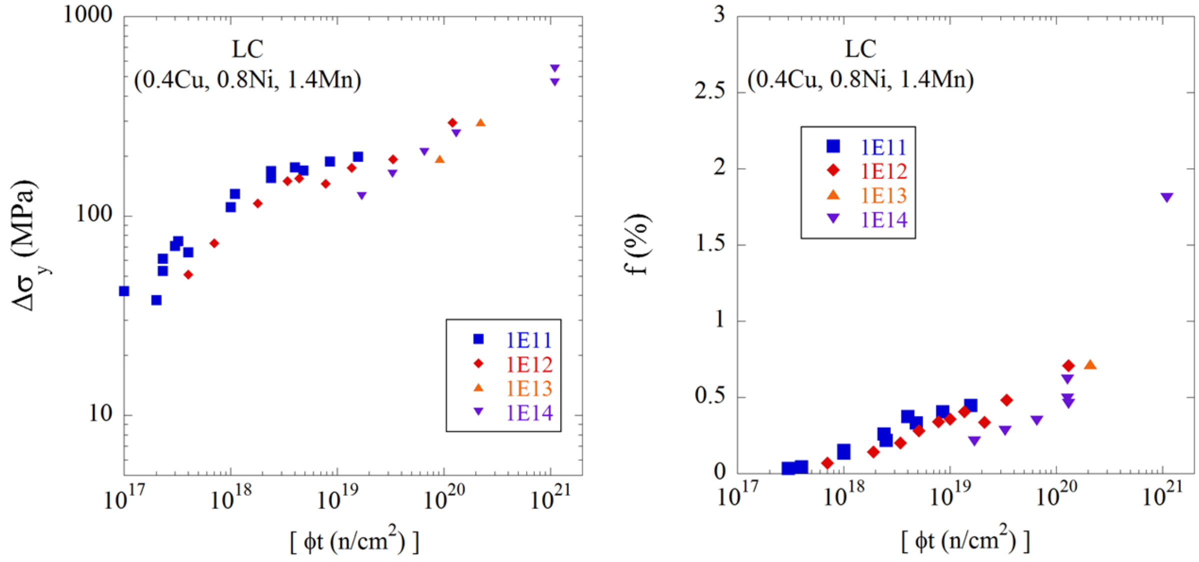

Figure 1.8.Δσy (left) and f (right) as a function of fluence for the 0.4% Cu, 0.8% Ni alloy LC for irradiations over a range of neutron flux.

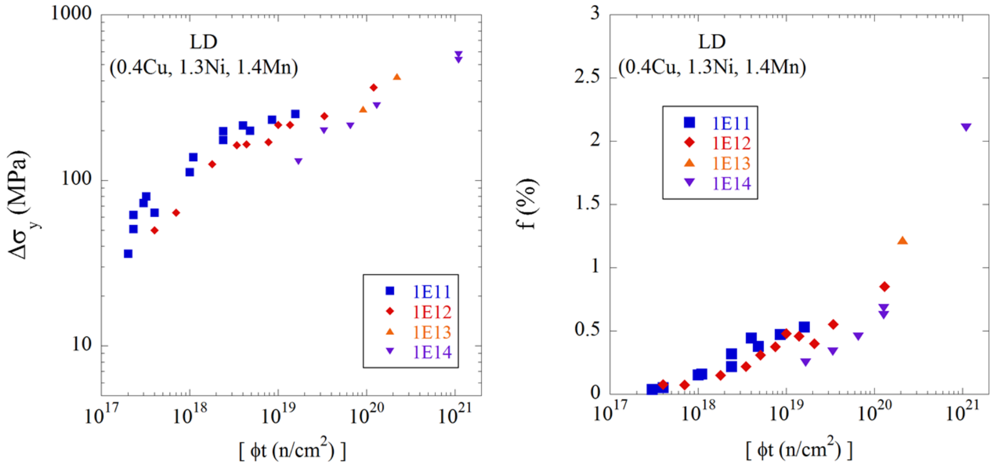

Figure 1.9. Δσy (left) and f (right) as a function of fluence for the 0.4% Cu, 1.3% Ni alloy LD for irradiations over a range of neutron flux.

These delays can be rationalized by considering the role ϕ plays with regards to the kinetics of precipitation. The average diffusion distance, d, of a solute atom under radiation is given by d = √(D*t). Higher ϕ irradiations lead to a higher D*, since more vacancies are created per unit time, but also simultaneously reduce the time is takes to reach a given ϕt. In flux regimes where defects are predominantly annihilated at sinks, an increase in ϕ directly results in an increase in the vacancy concentration and D*. Here, the total diffusion distance of atoms, given by √(D*t), is constant and there is no effect of increasing ϕ. At very high ϕ, the steady state concentration of defects is so high that newly created defects quickly recombine with other defects in the matrix. Thus, an asymptotic limit on the vacancy concentration and the corresponding D* is reached. In this regime, called the defect recombination regime, an increase in ϕ with a constant D* results in a decrease in the average diffusion distance of atoms, and consequently the amount of precipitation. While this explanation is overly simplified, it is presented here simply to show that the precipitation hardening in these high ϕt test reactor irradiation conditions would likely occur at much lower ϕt under low ϕ power reactor conditions.

As was shown in Figures 4-9 it is misleading to compare $\Delta\sigma_y$ and f_v for steels irradiated at different ϕ, since higher ϕ irradiations delay precipitation to higher ϕt. Odette has proposed a model for correcting these flux variations to plot data on an equivalent scale by defining an effective fluence, ϕt_e, for a given reference flux, ϕ_r, given by

$$\phi t_e = \phi t \left(\frac{\phi_r}{\phi}\right)^p \tag{1.1}$$

where ϕt is the actual fluence, ϕ is the actual flux, ϕ_r is a reference flux and p is a scaling parameter that varies with ϕ [2, 4].

It should be stressed that while this effective fluence model reduces very complex physics into a simple equation, the scaling parameter, p, varies based on the ϕ regime, such as thermal diffusion dominated, sink dominated or recombination dominated. The best fit p for high flux test irradiations has been found to be ≈ 0.2-0.25 [4]. An example flux correction can be seen in Figure 1.10 for a high Cu, medium Ni steel respectively. The $\Delta\sigma_y$ as a function of ϕt, can be seen to be delayed with increasing ϕ, but shows ≈ consistent trends at all ϕ when plotted in terms of ϕt_e. Below, in Figures10-15 are additional examples of split melt steels showing flux corrections in RPV alloys from various irradiations over a range of neutron flux.

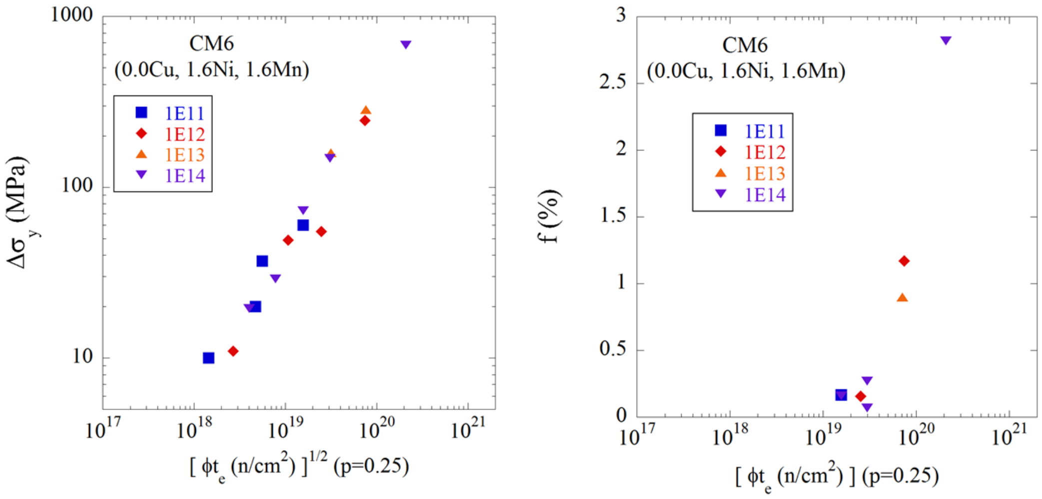

Figure 1.10. $\Delta\sigma_y$ (left) and f (right) as a function of fluence for the 0.01% Cu, 1.6% Ni alloy CM6 for irradiations over a range of neutron flux.

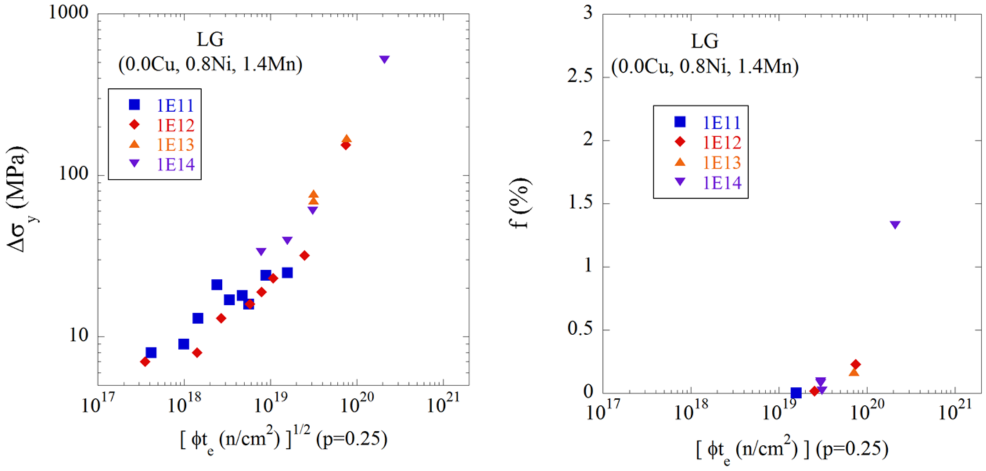

Figure 1.11. Δσy (left) and f (right) as a function of fluence for the 0.01% Cu, 0.8% Ni alloy LG for irradiations over a range of neutron flux.

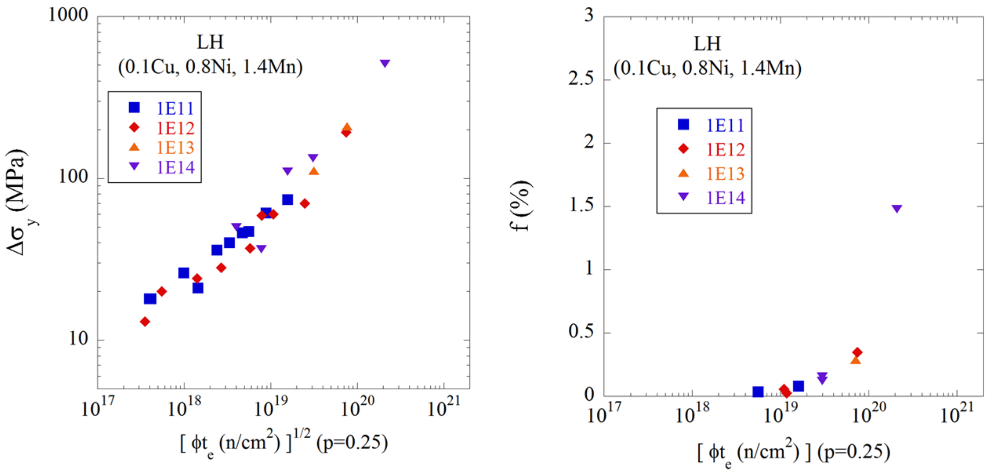

2

Figure 1.12. Δσy (left) and f (right) as a function of fluence for the 0.1% Cu, 0.8% Ni alloy LH for irradiations over a range of neutron flux.

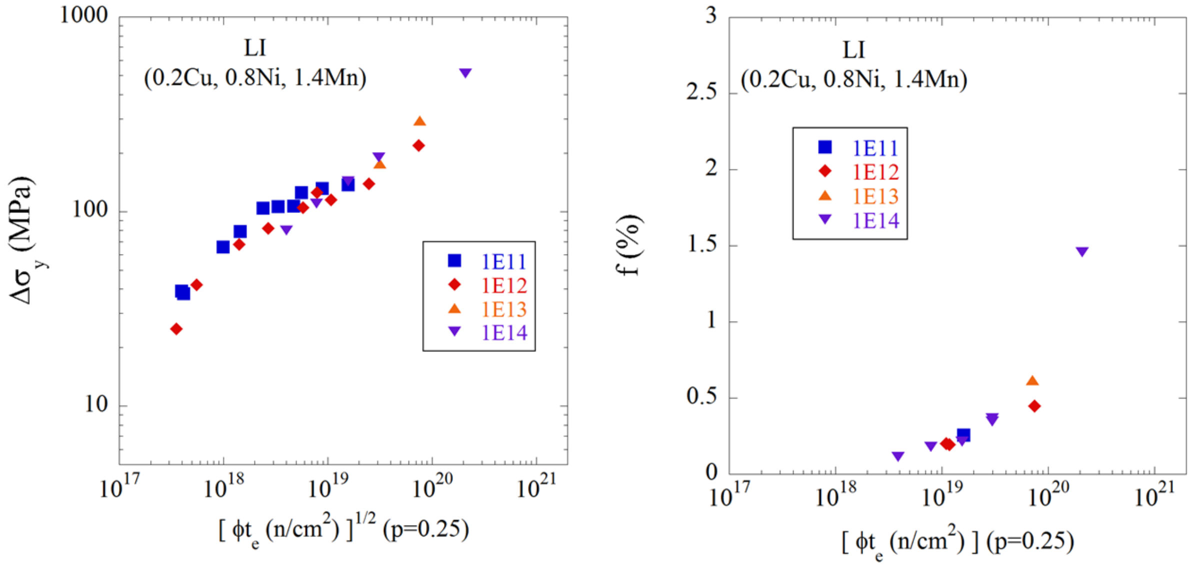

Figure 1.13. Δσy (left) and f (right) as a function of fluence for the 0.2% Cu, 0.8% Ni alloy LI for irradiations over a range of neutron flux.

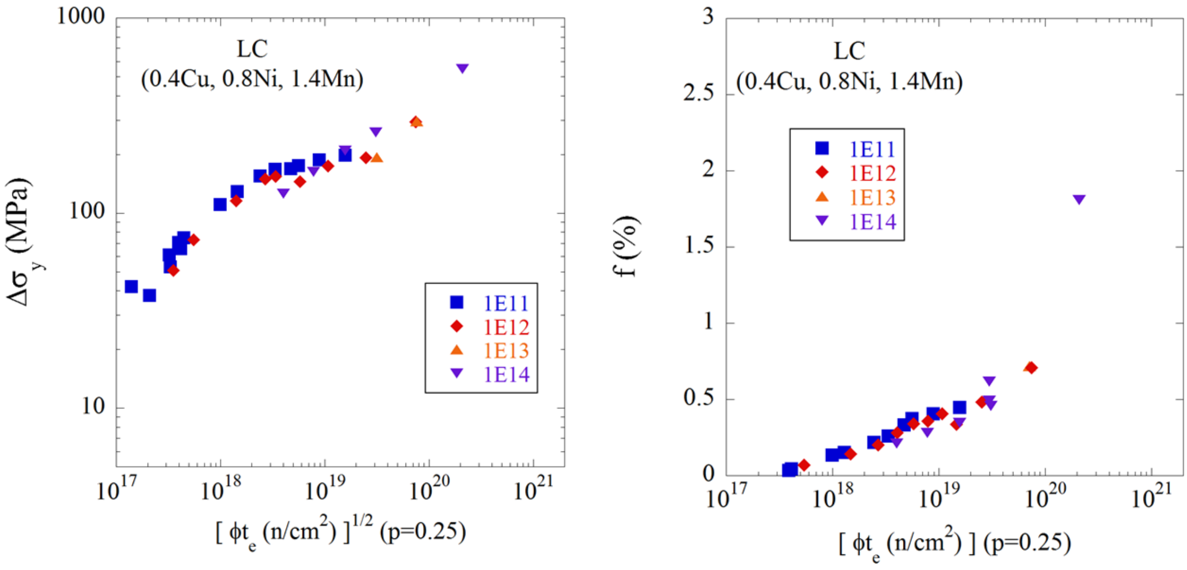

Figure 1.14.Δσy (left) and f (right) as a function of fluence for the 0.4% Cu, 0.8% Ni alloy LC for irradiations over a range of neutron flux.

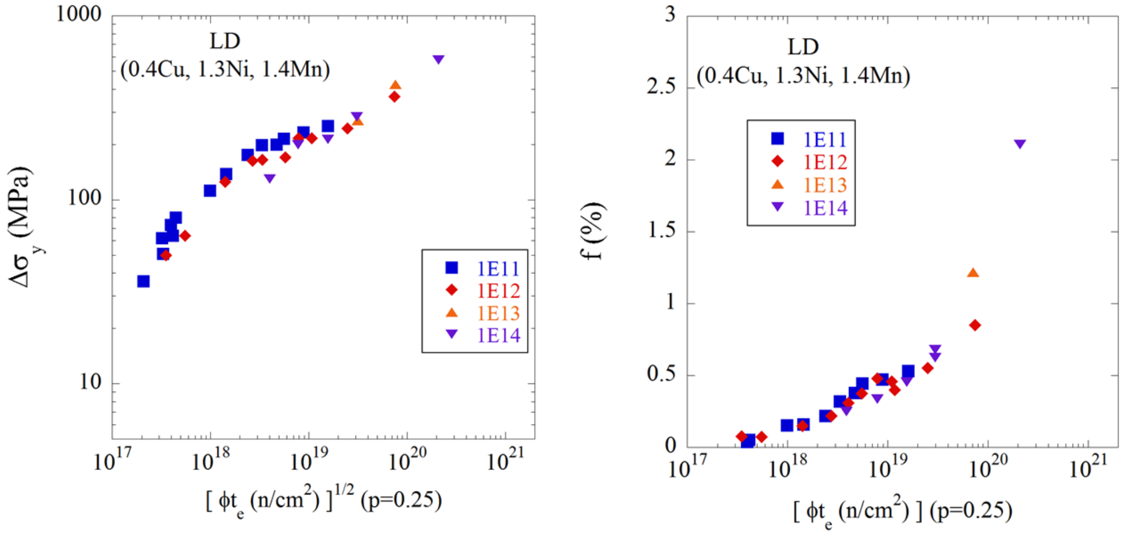

Figure 1.15. Δσy (left) and f (right) as a function of fluence for the 0.4% Cu, 1.3% Ni alloy LD for irradiations over a range of neutron flux.

1.4 References

1. Odette GR and Nanstad RK. "Predictive reactor pressure vessel steel irradiation embrittlement models: Issues and opportunities", JOM 2009;61(7):17–23.

2. Odette GR, Yamamoto T and Klingensmith D. "On the effect of dose rate on irradiation hardening of RPV steels", Philos. Mag. 2005;85(4–7):779–797.

3. Mader E. "Kinetics of irradiation embrittlement and the post-irradiation annealing of nuclear reactor pressure vessel steels" [PhD Thesis]. University of California, Santa Barbara, 1995.
4. Eason ED, Odette GR, Nanstad RK and Yamamoto T. "A physically based correlation of irradiation-induced transition temperature shifts for RPV steels," Oak Ridge National Lab, 2007; ORNL/TM-2006/530.
5. Odette GR, Mader E V., Lucas GE, Phythian WJ, et al. "The Effect of Flux on the Irradiation Hardening of Pressure Vessel Steels", In: 16th International Symposium on the Effects of Radiation on materials, 1993. p. 373.
6. Cunningham NJ. "Study of the Structure, Composition, and Stability of Y-Ti-O nm-Scale Features" [PhD Thesis]. University of California, Santa Barbara, 2012.
7. Wirth BD. "On the Character of the Nano-Scale Features in Reactor Pressure Vessel Steels" [PhD Thesis]. University of California, Santa Barbara, 1998.
8. Alinger MJ. "On the Formation and Stability of Nanometer Scale Precipitates in Ferritic Alloys during Processing and High Temperature Service" [PhD Thesis]. University of California, Santa Barbara, 2004.
9. Alinger MJ, Odette GR and Hoelzer DT. "On the role of alloy composition and processing parameters in nanocluster formation and dispersion strengthening in nanostuctured ferritic alloys", Acta Mater. 2009;57(2):392–406.

2. MICROSTRUCTURAL STUDIES OF LATE BLOOMING PHASES

2.1 Introduction

This report focuses on results from high ϕt test reactor and surveillance irradiations. First, APT results for six steels from two irradiation conditions, G1 and ATR1, are presented. The G1 condition, with $\phi t_e \approx 3.0\text{x}10^{19}$ n/cm^2, is very consistent with previous studies at low to medium ϕt, where Cu has a dominant effect of the formation of precipitates and the corresponding hardening. On the other hand, precipitates from ATR1 condition, at very high $\phi t_e \approx 2.1\text{x}10^{20}$ n/cm^2, are heavily dominated by the Mn, Ni and Si. In this condition, contrary to the current embrittlement prediction models, Cu has little effect on the total volume fractions or hardening. It should be noted that the highest ϕt that will be seen at an 80 year extended life is $\approx 1\text{x}10^{20}$ n/cm^2, so these two conditions span from well before to well after the predicted end of life. While the ATR1 results are beyond the maximum ϕt that will experienced by RPVs at 80 years of operation, the main purpose of the condition was to generate significant quantities of MNSP that could be readily characterized and modeled.

Next, the role of Ni at very high ϕt_e is examined in further detail, including the effect of reducing or removing Ni on the formation of precipitates. Following this, results from a low ϕ surveillance program are presented and compared to a similar alloy from the very high ϕt_e ATR1 condition. Finally, the report concludes with a brief discussion on the relationship between the precipitates and hardening.

2.2 Measured Compositions and Compositional Variation

APT was carried out on 6 steels in two irradiation conditions, G1 and ATR1. The average APT bulk solute compositions, in at.%, are given in Table 2.1 and Table 2.2 for the medium (G1) and very high (ATR1) ϕt_e conditions, respectively. The nominal bulk chemistries are given in parenthesis. Observed differences between the measured total and nominal values are largely expected. For example, the alloys that nominally contain ≈ 0.34% Cu have a lower average total APT content of ≈ 0.25%. This value is consistent with previous observations of lower residual amounts in solution due to coarse scale pre-precipitation during tempering and stress relief heat treatments, when the total Cu is beyond the solubility limit [1–4]. Likewise the Mn contents are lower than the nominal value since this element is partially sequestered in coarse $Mn_{0.6}Fe_{2.4}C$ and MnS precipitates. The quantitative differences between the nominal and measured bulk compositions are shown in Table 2.1 and Table 2.2.

These overall composition averages do not reflect the tip-to-tip variations in individual alloys, which are significant in some cases. For example, the standard error for the bulk Mn measurements of a given alloy is as large as 0.20%. While seemingly an esoteric detail, it is show below that the effects of the tip-to-tip composition variations in a given alloy are directly reflected in the precipitates, and are also consistent with observed alloy-to-alloy trends. A corollary is that it is important to use the actual local compositions in analyzing the APT precipitate data.

Table 2.1. Bulk APT and nominal (in parentheses) compositions in at.% for the medium ϕt_e condition (G1).

Alloy	Cu	+/-	Ni	+/-	Mn	+/-	Si	+/-
LC	0.21 (0.36)	0.02	0.91 (0.81)	0.10	0.97 (1.46)	0.20	0.53 (0.46)	0.06
LD	0.21 (0.33)	0.01	1.00 (1.16)	0.01	1.08 (1.37)	0.10	0.52 (0.45)	0.03
LG	0.01 (0.01)	0.00	0.86 (0.69)	0.05	1.09 (1.36)	0.09	0.49 (0.43)	0.02
LH	0.08 (0.09)	0.00	0.72 (0.69)	0.01	0.97 (1.38)	0.03	0.45 (0.47)	0.01
LI	0.15 (0.17)	0.01	0.72 (0.69)	0.01	1.21 (1.36)	0.03	0.43 (0.46)	0.01
CM6	0.00 (0.02)	0.01	1.34 (1.57)	0.10	1.09 (1.50)	0.20	0.33 (0.33)	0.06

**Note that these steels also contain Mo, C, P, and other trace impurities*

Table 2.2. Bulk APT and nominal (in parentheses) compositions in at.% for the very high ϕt_e condition (ATR1).

Alloy	Cu	+/-	Ni	+/-	Mn	+/-	Si	+/-
LC	0.28 (0.36)	0.01	0.80 (0.81)	0.03	1.16 (1.46)	0.01	0.43 (0.46)	0.02
LD	0.25 (0.33)	0.02	1.18 (1.16)	0.05	1.08 (1.37)	0.08	0.54 (0.45)	0.02
LG	0.00 (0.01)	0.01	0.71 (0.69)	0.01	0.87 (1.36)	0.08	0.43 (0.43)	0.01
LH	0.08 (0.09)	0.01	0.73 (0.69)	0.02	1.19 (1.38)	0.06	0.42 (0.47)	0.01
LI	0.15 (0.17)	0.01	0.70 (0.69)	0.01	0.97 (1.36)	0.10	0.42 (0.46)	0.01
CM6	0.00 (0.02)	0.01	1.69 (1.57)	0.04	1.42 (1.50)	0.03	0.39 (0.33)	0.01

**Note that these steels also contain Mo, C, P, and other trace impurities*

2.3 Medium ϕt_e G1 Condition

Figure 2.1 shows atom maps for the highest Ni content, Cu-free steel (CM6) and the high Ni-Cu content steel (LD) in the medium ϕt_e condition. The precipitates are numerous and well defined in the Cu-bearing steel, but are not as easy to observe in the Cu-free alloy; however, they are readily characterized by the cluster search algorithm.

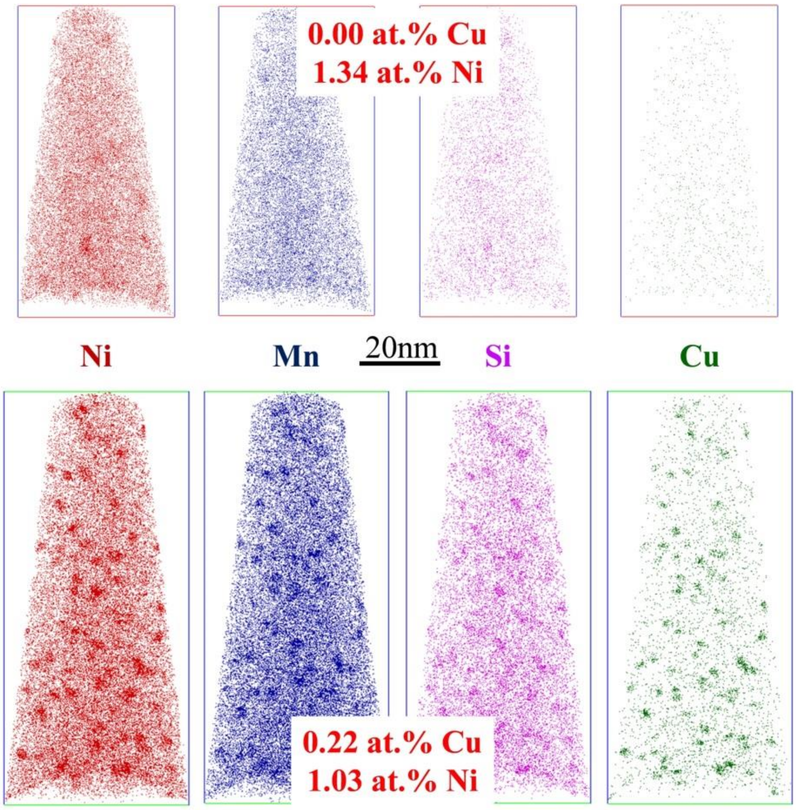

Figure 2.1. Atom Maps for the highest Ni, Cu free (top) and high Ni-Cu (bottom) alloys irradiated to medium ϕt_e.

Table 2.3 and Table 2.4 summarize the corresponding APT precipitate measurements and matrix compositions, respectively. The left portion of Table 2.3 gives the Cu-Mn-Ni-Si compositions of the precipitates. The nominal precipitate Fe content is also shown to the right of the precipitate compositions. While it is thought that the Fe is largely an APT artifact, it is included for those who might seek an alternative analysis. The right portion of Table 2.3 gives the average radius (<r>), number density (N) and mole fraction (f_v) of the MNSP, as well as the standard error uncertainties in the measurements.

Table 2.3. Precipitate compositions and <r>, N and f_v at medium ϕt_e (G1).

Alloy	Precipitate Relative Compositions (at.%)								Fe*	<r> (nm), N (1E23 m^{-3}), f_v (%)					
	Cu	+/-	Ni	+/-	Mn	+/-	Si	+/-		<r>	+/-	N	+/-	f	+/-
LC	25.7	1.4	35.1	5.0	23.6	7.2	15.7	3.8	60.8	1.15	0.10	9.2	1.4	0.58	0.08
LD	22.2	0.7	37.8	0.5	24.6	1.2	15.5	0.7	58.6	1.13	0.02	11.5	0.7	0.68	0.04
LG	0.5	0.1	46.8	2.3	25.5	3.6	27.2	1.9	53.3	0.72	0.04	5.3	1.5	0.08	0.02
LH	14.8	0.9	39.8	2.5	25.1	1.8	20.3	0.1	58.7	0.92	0.05	4.9	0.5	0.16	0.01
LI	24.2	1.0	34.2	0.5	27.4	0.8	14.2	0.4	57.2	1.10	0.03	6.9	0.6	0.37	0.04
CM6	0.1	0.1	58.9	5.0	25.6	7.2	15.5	3.8	49.6	0.70	0.10	4.6	3.0	0.07	0.04

** Nominal Fe assumed to be an artifact, but provided for alternative interpretations.*

Table 2.4. Matrix compositions at medium ϕt_e (G1).

Alloy	Cu	+/-	Ni	+/-	Mn	+/-	Si	+/-
LC	0.06	0.01	0.70	0.08	0.84	0.18	0.43	0.06
LD	0.06	0.00	0.74	0.02	0.91	0.08	0.41	0.03
LG	0.01	0.00	0.81	0.04	1.07	0.09	0.46	0.02
LH	0.06	0.01	0.66	0.01	0.93	0.03	0.41	0.01
LI	0.06	0.00	0.59	0.00	1.11	0.02	0.37	0.01
CM6	0.00	0.01	1.27	0.08	1.05	0.18	0.31	0.06

The bar chart in Figure 2.2a summarizes the precipitate f_v and corresponding compositions. It will later be show that the f_v directly scales with the individual tip solute contents. Thus Figure 2.2a shows the mole fraction for individual tips with bulk compositions close to the average values of the alloy. The trends for Ni content in Cu-free steels, Cu content at medium Ni content, and Cu content at both the higher and the highest Ni content, are individually highlighted in the three sections. The corresponding <r> and N are plotted in Figure 2.2b.

The major observed trends are as follows:

- The highest Ni content, Cu-free steel has only a slightly larger f_v than the Cu-free, medium Ni content alloy (Fig. 3a left). The Cu-Mn-Ni-Si mole fraction of the precipitates, hence the total f_v, increase with increasing Cu content in the medium Ni content steels (Fig. 3a center). The mole fraction of Cu in the precipitates increases from ≈ 0, in the Cu-free steel, to 0.15% in the highest Cu content steel. The average residual matrix Cu content is 0.06% in the Cu-bearing steels, indicating incomplete phase separation for this highly insoluble element (Table 2.4).

- The increase in f_v with higher Ni content in the 0.21% Cu steels is due to higher contents of Ni, Mn and Si in the precipitates (Fig. 3a center and right). These results clearly demonstrate the thermodynamically driven synergisms between these elements, and the very important role played by

Ni. The corresponding effect of increasing Ni content on f_v in the Cu-free and high Cu content steels is minimal in this case (Fig. 3a right) because f_v is so strongly dependent on Cu.

- Both N and <r> increase with Cu content (Fig. 3b). N also increases with Ni content, except in the Cu-free steels. It should be noted that at these small f_v and <r>, the uncertainties in N are larger.

- The relative Mn-Ni-Si compositions are generally similar in the medium and high Ni content steels (LG, LH, LI, LC, LD) with fractional averages and standard deviations of: 0.31±0.04 Mn, 0.47±0.01 Ni and 0.22±0.03 Si. The precipitate Ni fraction is higher and the Si is lower in the highest Ni content, Cu-free steel (CM6) averaging 0.26 Mn, 0.59 Ni and 0.15 Si.

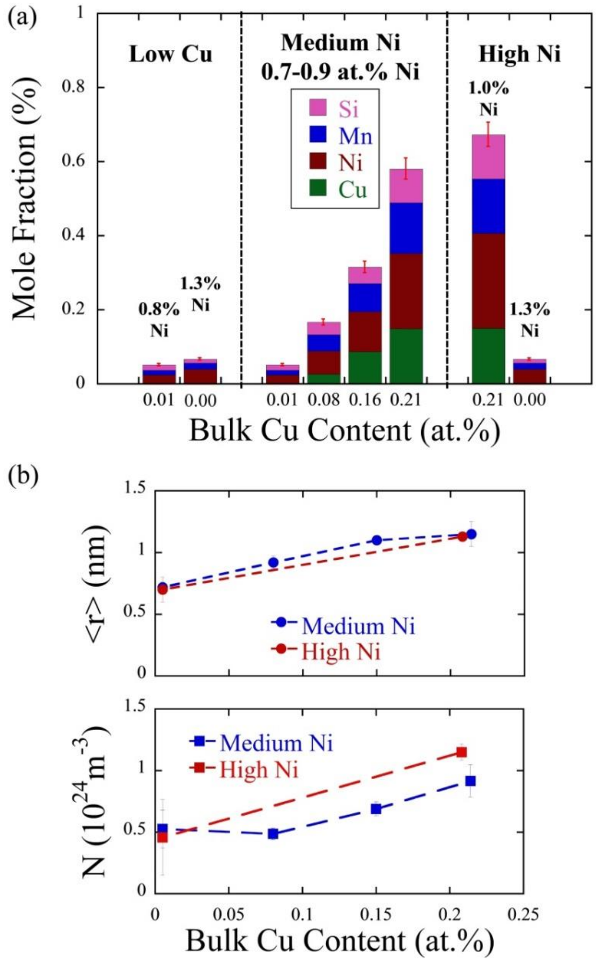

Figure 2.2. (a) The precipitate f_v for the individual constituent elements in a single run of all 6 alloys; and, (b) <r> and N plotted as a function of Cu. Note that in some cases, the error bars were smaller than the size of the symbols.

The most important observation for the medium ϕt_e condition is that Cu and Ni play a combined role in mediating f_v, although Cu seems to have a stronger influence over the range of Ni compositions studied here. While the features in the Cu-bearing steels contain more than 75% Mn-Ni-

Si, the total f_v of these elements roughly scales with the alloy Cu content. This can be seen in Figure 2.3, which plots the Mn-Ni-Si f_v, i.e. ignores the Cu portion of the total f_v, as a function of a) Cu and b) Ni. Each point represents the bulk Cu or Ni along with the measured MNSP f_v for a given atom probe tip. Thus higher Cu content clearly leads to larger amounts of Mn, Ni and Si coming out of solution.

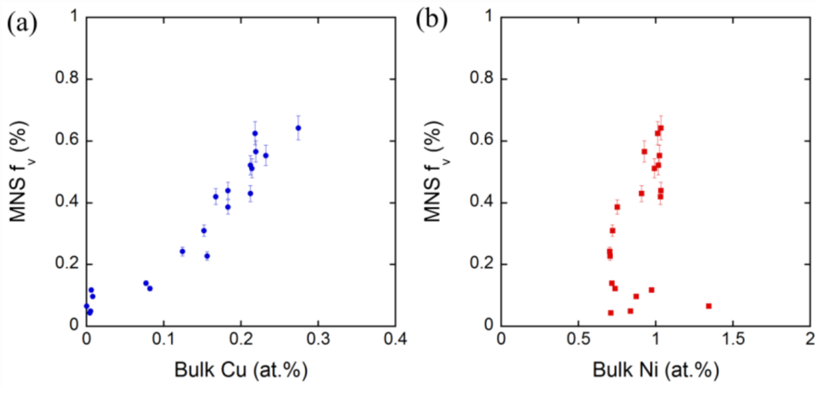

Figure 2.3. MNSP f_v as a function of a) bulk Cu and b) bulk Ni.

The most plausible hypothesis for explaining these observations is that in the Cu-free steels, the clusters are still predominantly matrix features. However, the presence of Cu catalyzes the formation of MNSP. The Cu is highly supersaturated, thus precipitates quickly, while simultaneously being enriched in the other solutes. In the presence of Cu, the difficult nucleation step for nearly pure Mn-Ni-Si phases is largely avoided by co-precipitation, and these solutes subsequently flow to the Cu-catalyzed precipitates starting at relatively low ϕt.

2.4 Very High ϕt_e ATR-1 Condition

Atom maps, for the same alloys as Figure 2.1, but from the very high ϕt_e condition (ATR1) are shown in Figure 2.4. They clearly demonstrate the large changes that occur when going from medium to very high ϕt_e. It should again be stressed that in this case, the $\phi t_e \approx 2.1\text{x}10^{20}$ n/cm^2 is over twice that any RPV is expected to experience even at an 80 year extended life. The average precipitate parameters are summarized in Table 2.5. These large changes are not surprising, since the ϕt_e increased by a factor of ≈ 7 between the medium and very high ϕt_e conditions. The major observations can be summarized as follows:

There is a large increase in f_v between the medium and very high ϕt_e conditions. The histograms in Figure 2.5a, again for individual tips with bulk compositions close to the average values, show both the total f_v and precipitate composition for each alloy. These results demonstrate that the effect of Cu is not nearly as significant at very high versus medium ϕt_e, and that Ni plays a much stronger role than in the former case. At very high ϕt_e, the MNSP no longer need Cu to form.

The precipitate f_v more than doubles in the Cu-free steels with increasing bulk Ni from ≈ 0.7% to 1.6% (Fig. 5a left). In contrast, at medium Ni contents, increasing the bulk Cu only slightly increases f_v (Fig. 5a center); this increase is almost entirely caused by the higher amount of co-precipitate Cu itself. Notably, the highest ≈ 1.6% Ni, Cu-free steel (CM6) has a larger f_v than in the high 1.2% Ni, 0.25% Cu (LD) alloy (Fig. 5a right).

Figure 2.5c shows that <r> modestly increases with Cu in both medium and higher Ni content steels. In contrast, the corresponding N decreases with Cu. In the case of the high Ni-Cu content steel (LD), the very high ϕt_e N is lower than for the medium ϕt_e condition, perhaps suggesting that the precipitates have begun to coarsen.

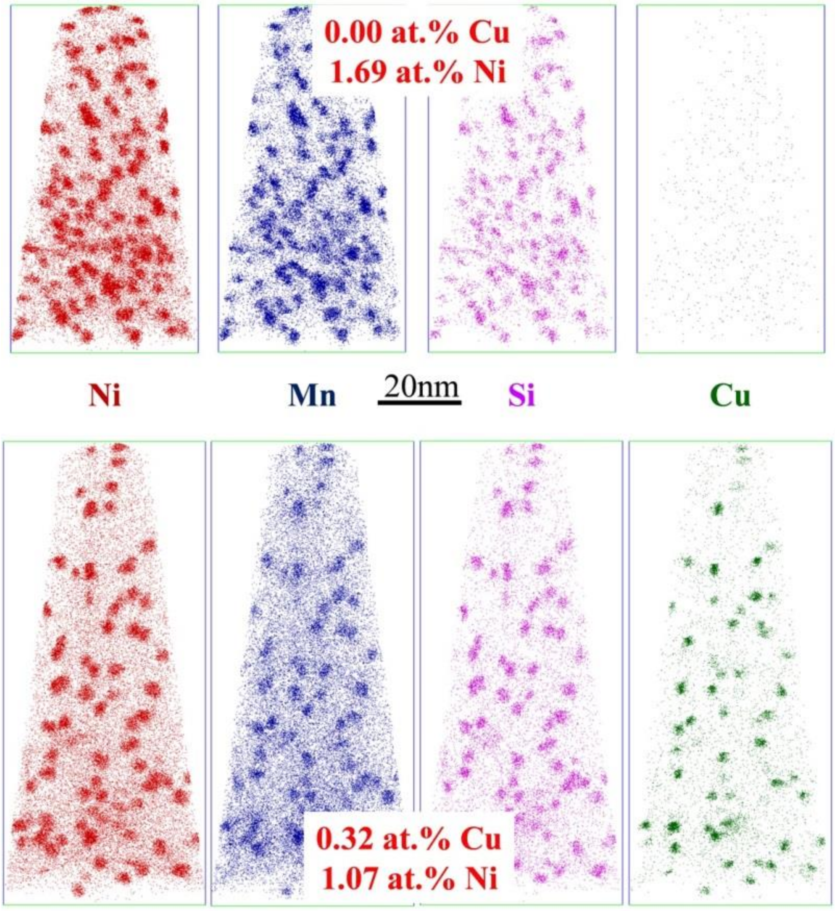

Figure 2.4. Atom Maps for the highest Ni, Cu free (top) and high Ni-Cu (bottom) alloys irradiated to very high ϕt_e.

Table 2.5 shows that at the very high ϕt_e, the precipitates in the nominally Cu-free steel contain < 0.01 of this element. In the medium Ni content steels, the precipitate Cu composition increases (LH, LI, LC) with this element up to ≈ 15% (LC).

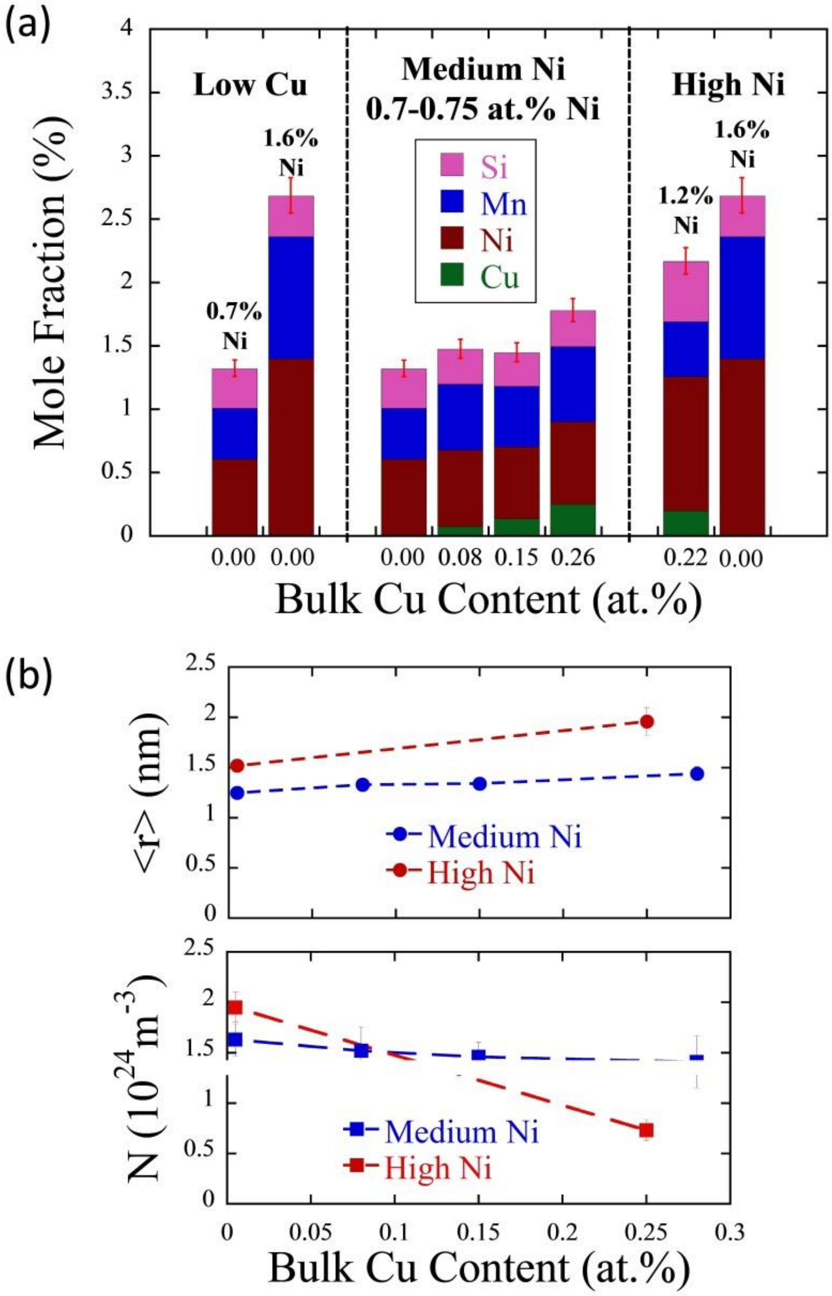

Figure 2.5. The Cu dependence of: (a) f_v showing the constituent elements for individual runs of each alloy and (b) <r> and N at very high ϕt_e. Note that in some cases, the error bars were smaller than the size of the symbols.

Table 2.5. Precipitate compositions and <r>, N and f_v at very high ϕt_e (ATR1).

Alloy	Precipitate Relative Compositions (at.%)								Fe*	<r> (nm), N ($10^{23}m^{-3}$), f_v (%)					
	Cu	+/-	Ni	+/-	Mn	+/-	Si	+/-		<r>	+/-	N	+/-	f	+/-
LC	14.8	2.5	37.4	1.8	31.9	1.2	15.9	1.4	62.0	1.44	0.07	14.1	2.6	1.81	0.19
LD	10.3	2.4	46.9	3.6	22.5	2.5	20.3	1.8	55.4	1.96	0.14	7.3	1.0	2.11	0.23
LG	0.2	0.1	46.1	1.5	31.2	2.8	22.5	1.6	63.5	1.25	0.04	16.3	1.6	1.33	0.03
LH	5.0	0.2	40.7	1.5	35.6	2.4	18.6	1.1	64.9	1.33	0.05	15.2	2.4	1.48	0.03
LI	9.5	0.5	39.7	2.5	31.9	4.2	18.9	1.9	62.7	1.34	0.06	14.6	1.4	1.46	0.04
CM6	0.1	0.0	52.5	1.2	35.5	1.9	11.9	0.5	58.9	1.52	0.06	19.54	1.5	2.82	0.14

* *Nominal Fe assumed to be an artifact, but provided for alternative interpretations.*

Table 2.6. Matrix compositions at very high ϕt_e (ATR1).

Alloy	Cu	+/-	Ni	+/-	Mn	+/-	Si	+/-
LC	0.02	0.01	0.11	0.01	0.47	0.02	0.10	0.01
LD	0.03	0.01	0.18	0.01	0.57	0.07	0.08	0.01
LG	0.00	0.00	0.08	0.01	0.37	0.06	0.10	0.01
LH	0.02	0.01	0.11	0.01	0.57	0.04	0.11	0.01
LI	0.02	0.01	0.11	0.01	0.41	0.05	0.11	0.01
CM6	0.00	0.00	0.17	0.01	0.32	0.01	0.04	0.01

Figure 2.6 shows the relative precipitate Mn-Ni-Si compositions do not change much between medium and very high ϕt_e. For example, the average fractional compositional difference for the medium Ni content steels (LG, LH, LI, LC) is 0.02 Mn, -0.01 Ni and -0.01 Si in going from medium to very high ϕt_e. Further, the Mn-Ni-Si precipitate compositions are generally similar in the medium Ni content steels at very high ϕt_e (LG, LH, LI, LC) with fractional averages and standard deviations of: 0.35±0.03 Mn, 0.44±0.02 Ni and 0.20±0.02 Si. The precipitate Mn fraction is lower and Ni is higher in the high Ni-Cu content steel (LD) at 0.25 Mn, 0.52 Ni, and 0.23 Si. The corresponding composition of the highest Ni content, Cu-free steel (CM6) is 0.36 Mn, 0.52 Ni and 0.12 Si. Thus the precipitate compositions clearly reflect changes in the bulk alloy Ni and Si chemistry.

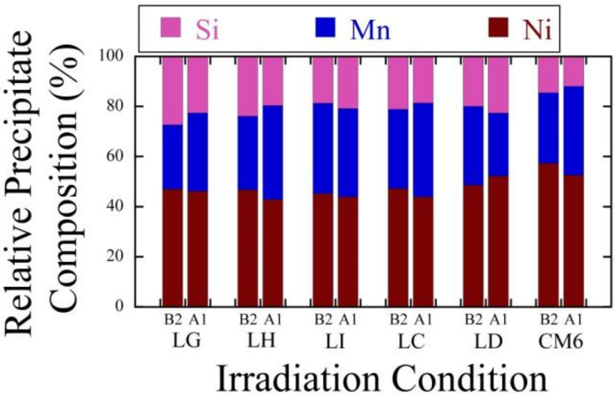

Figure 2.6. The average precipitate Mn-Ni-Si compositions at medium and very high ϕt_e.

Figure 2.7 illustrates the evolution of the morphology of precipitates with increasing ϕt_e in the high Ni-Cu content (LD) steel. Figure 2.7a shows a cross section of a precipitate at medium ϕt_e, where there appears to be a Mn-Ni-Si shell surrounding a Cu-rich core, consistent with previous experimental results and Lattice Monte Carlo simulations [5–8]. Figure 2.7b shows a precipitate at very high ϕt_e, where there is a Cu-rich core-shell structure, similar to that at medium ϕt_e, but this feature is associated with a nearly "pure" Mn-Ni-Si co-precipitate appendage. Such appendages have also been seen in irradiated surveillance steels [9].

In summary, the evolution between medium and very high ϕt_e is dominated by the continued flow of Mn-Ni-Si to the precipitates. In Cu-free steels it is likely that the precipitates evolve from matrix feature solute-defect clusters initially formed in displacement cascades. At higher supersaturated Cu contents, Cu precipitates form and become rapidly enriched in Mn, Ni and Si. While initially the Mn, Ni and Si form a shell around the Cu-rich core, an almost pure Mn-Ni-Si co-precipitate appendage continues to grow on the CRP at higher ϕt_e.

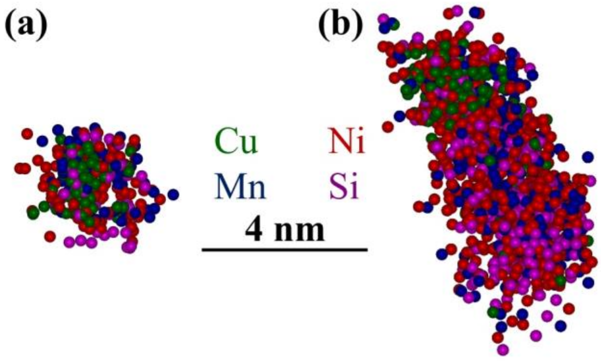

Figure 2.7. APT maps of typical precipitates in the high Ni-Cu content steel (LD): (a) at medium ϕt_e, and (b) at very high ϕt_e.

2.5 APT Precipitate Compositions vs Mn-Ni-Si Intermetallic Phases

As Figure 2.6 demonstrated, the Mn-Ni-Si compositions of the precipitates in Cu-free steels are similar to those in the co-precipitates formed in Cu-bearing steels at very high ϕt_e. These compositions can be compared to known intermetallic phases in the corresponding Mn-Ni-Si ternary and Mn-Ni-Si-Fe quaternary systems. As described in detail in [10], recent Calphad-Thermocalc computational modeling studies carried out at the University of Wisconsin (UW), in collaboration with UCSB, have shown there are a variety of equilibrium Mn-Ni-Si intermetallic phases in the Fe-Mn-Ni-Si quaternary system at low RPV operating temperatures. Briefly, this model was based on thermodynamic parameters from a commercial database, which predicts varying fractions of Γ_2 ($Mn(Ni_xSi_{1-x})_2$, T6) and G ($Mn_6Ni_{16}Si_7$, T3) phases, depending on the alloy Mn-Ni-Si composition. In this case, the bulk composition of the alloy was determined from the average APT values measured in this study.

Figure 2.8 shows the APT Mn-Ni-Si precipitate compositions, from the very high ϕt_e ATR1 condition, (filled symbols) plotted on the Mn-Ni-Si ternary phase diagram for both the medium (circles) and high (squares) Ni content steels compared to the predicted average compositions for the CALPHAD model. The model predicts 100% Γ_2 (T6) (open cyan square) for the highest Ni content, Cu-free (CM6) steel, which is very consistent with the APT data (filled cyan square). The model predicts ≈ 73% G (T3) and ≈ 27% Γ_2 (T6) phases (open red square) for the high Ni-Cu content (LD) steel, again very close to the measured value (filled red square). The medium Ni content alloys cluster around the Si-rich end of the Γ_2 phase field (filled circles), shown by the heavy green line at ≈ constant Mn, while the commercial database predicts the presence of either G or Γ_2 phases (open circles).

The precipitates in the Cu-free, medium Ni content steel (LG, filled blue circle) have slightly less Mn and higher Ni than the other three medium Ni content steels that contain various amounts of Cu. This might be interpreted to suggest that there is some effect of Cu on the dominantly Mn-Ni-Si phases. However, these differences are actually highly consistent with variations in the bulk alloy Ni contents, that trade off with Mn in the precipitates, at approximately constant Si. For example, the medium Ni content alloy with the greatest fraction of Mn in the precipitates (LH), which is furthest to the right of the Γ_2 line in the Mn-Ni-Si ternary (filled green circle), has a bulk Mn/Ni of 1.6. On the other hand, the alloy furthest to the left of the Γ_2 line (LG, filled blue circle) has much less bulk Mn, with a bulk Mn/Ni of 1.2.

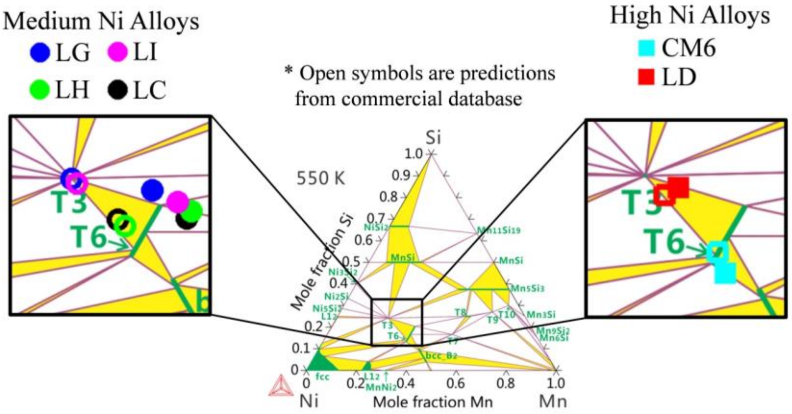

Figure 2.8. A Gibbs triangle showing APT Mn-Ni-Si precipitate compositions (filled symbols) at very high ϕte compared to UW CALPHAD predictions for a commercial database (open symbols) [10]. Note that the T3 and T6 phases are referred to in the text as G and Γ2, respectively.

While the relatively good agreement between Thermocalc average composition predictions and the APT measurements is encouraging, there are also important differences that should be noted. In particular, the commercial database predicts the presence of multiple near-stoichiometric phases in some alloys. In contrast, the APT measurements show that there is a unimodal distribution of MNSP precipitate compositions that decreases in extent with increasing precipitate size, converging to a relatively narrow range of Mn-Ni-Si at the largest r_p, seen in Figure 2.9. The corresponding average compositions also appear to vary somewhat with r_p. The variation and spread in compositions with r_p is an example of the additional insight available from APT measurements, though the large spread at small sizes is predominantly caused by counting statistics due to the low efficiency of the LEAP.

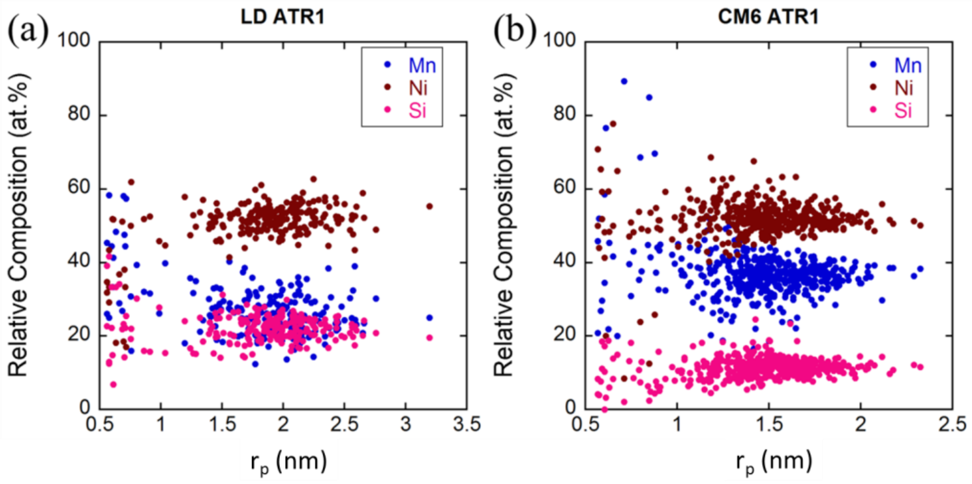

Figure 2.9. Precipitate relative MNS composition for the high Cu-Ni steel (LD) and Cu-free, highest Ni content steel (CM6) form the very high ϕt_e condition.

2.6 *Precipitate Structure*

The very close agreement between equilibrium thermodynamic predictions and APT precipitate compositions and f_v present a very strong case that the precipitates are in fact intermetallic phases. While not within the scope of this thesis, it should be noted that Sprouster et. al. at Brookhaven National Laboratory (BNL), in collaboration with UCSB, used X-ray diffraction measurements at the National Synchrotron Light Source II to determine the crystal structure of the precipitates from the ATR1 condition [11]. XRD patterns for LD before and after irradiation are shown in Figure 2.10, from [11].

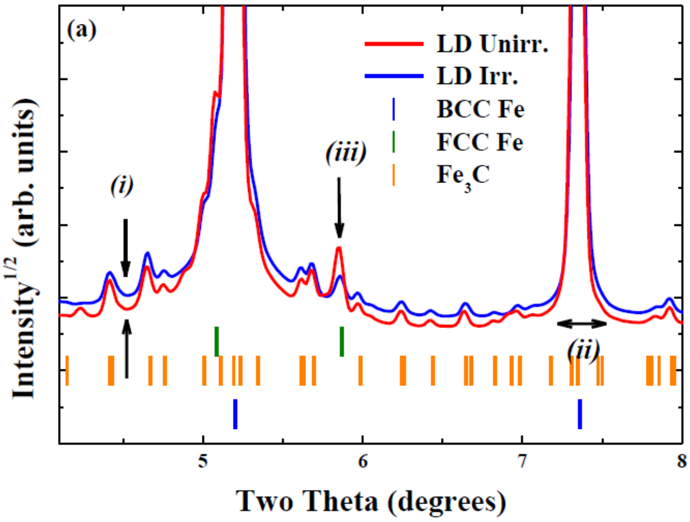

Figure 2.10. XRD pattern for LD in the baseline and ATR1 irradiated conditions showing an increase in the structured scattering background following irradiation, from [11].

The G phase, referred to as the T3 phase in Figure 2.8, is a complex intermetallic phase with the $Mg_6Cu_{16}Si_7$-type structure and the stoichiometric composition of $Mn_6Ni_{16}Si_7$. It belongs to the space group Fm-3m and has a lattice constant of 1.1158 nm [12, 13]. The Γ2 phase, referred to as the T6 phase in Figure 2.8, has a finite phase field with a composition of $Mn(Ni_xSi_{1-x})_2$ [10]. It has the Cu_2Mg structure and belongs to the Fd-3m space group with a lattice parameter of 0.6687 nm [12].

The peaks from the Mn-Ni-Si phases, which are significantly broadened due to the nm-scale of the precipitates, are thought to be the cause of the increase in the background of the irradiated samples. Thus, the Rietveld refinement incorporated either the G ($Mn_6Ni_{16}Si_7$) or Γ_2 ($Mn(Ni_xSi_{1-x})_2$) phases and used a fixed size for the Mn-Ni-Si precipitates, but allowed the f_v and lattice parameter to vary. Interestingly, when incorporating the G phase into the refinement, the best fit f_v and lattice parameter were very consistent with the APT results and the theoretical lattice parameter for all alloys except CM6. On the other hand, CM6 returned non-physical parameters when refined with the G phase, but resulted in f_v and lattice parameters consistent with APT and theory when fit with the Γ_2 phase [11].

Table 2.7. Summary of experimental and modeling predictions from the ATR1 irradiated condition.

Alloy	Nominal Composition (at.%)		Likely Phase		
	Bulk Cu	Bulk Ni	APT Composition	Thermocalc Prediction	XRD Structure
CM6	0.02	1.57	Stoichiometric Γ_2	Γ_2	Γ_2
LD	0.33	1.16	Stoichiometric G	G	G
LC	0.36	0.81	Si rich end of Γ_2	G	G
LI	0.17	0.69	Si rich end of Γ_2	Γ_2	G
LH	0.09	0.69	Si rich end of Γ_2	G	G
LG	0.00	0.69	Si rich end of Γ_2	Γ_2	G

A summary of APT, XRD and CALPHAD predictions based on the Thermocalc database is shown in Table 2.7. Two alloys, CM6 and LD, have very consistent agreement among both experimental techniques and the equilibrium predictions. The medium Ni alloys all show precipitate compositions near the Si-rich end of the Γ_2 phase, though XRD shows the precipitates to have the G phase structure. The models predict either the G or Γ_2 phases for these 4 alloys. The reason for this variation in predicted phase for alloys with nominally the same Ni, Mn and Si is because the models were calibrated using the measured APT compositions, which showed wider variations in Ni and Mn for the alloys. It is unclear why APT shows compositions closer to one phase, while XRD shows the structure of another, but the likely reason is the very small nature of the precipitates. With such high surface area compared to the total volume for the nm-scale precipitates, any interfacial chemistry changes, possibly driven by the surface energy between the MNS phase and Fe matrix, would have a large result on the average precipitate composition. Unfortunately, accurately determining whether the precipitate has, for example, Mn enrichment at the interface is not possible due to resolution limits of APT. In addition, the phase diagram shown in Figure 2.8 has not been experimentally verified, because reaching equilibrium at such low temperatures is not feasible due to the low kinetics. Thus, it may be that the phase field for the G phase is much larger than predicted and does not require exact stoichiometry. Last, the role of radiation induced segregation should not be ruled out.

2.7 Role of Ni at Very High ϕt_e

As was shown in Figure 2.3, at medium ϕ_e Cu is the dominant variable dictating both the total and MNSP f_v. Alternatively, at very high ϕt_e condition, large f_v of MNSP form even in steels that contain no Cu. Figure 2.11 shows the MNSP f_v, again with the Cu mole fraction being subtracted from the total f_v as in Figure 2.3 for the medium ϕt_e condition, as a function of a) Cu and b) Ni. The medium Ni steels, labelled as blue circles in Figure 2.11a, all have ≈ the same MNSP f_v, even with bulk Cu contents varying from 0 to 0.35%. This is because the very high ϕt_e is well beyond the range where Cu is needed to catalyze Mn-Ni-Si precipitation. Indeed, the small increase in the Mn-Ni-Si f_v with increasing Cu is largely due to the fact that slightly higher Ni contents happen to accompany the increase of Cu in this case. In contrast to the effect of Cu, higher Ni contents cause a significant increase in Mn-Ni-Si f_v in the higher Ni content alloys (LD and CM6) seen in the green in Figure 2.11a. The role of Ni can be seen much more clearly in Figure 2.11b, where there is a strong correlation between the bulk Ni content of the alloys and the MNS f_v. This is drastically different at medium ϕt_e, seen in Figure 2.3b, where there is little correlation between the bulk Ni and MNS f_v.

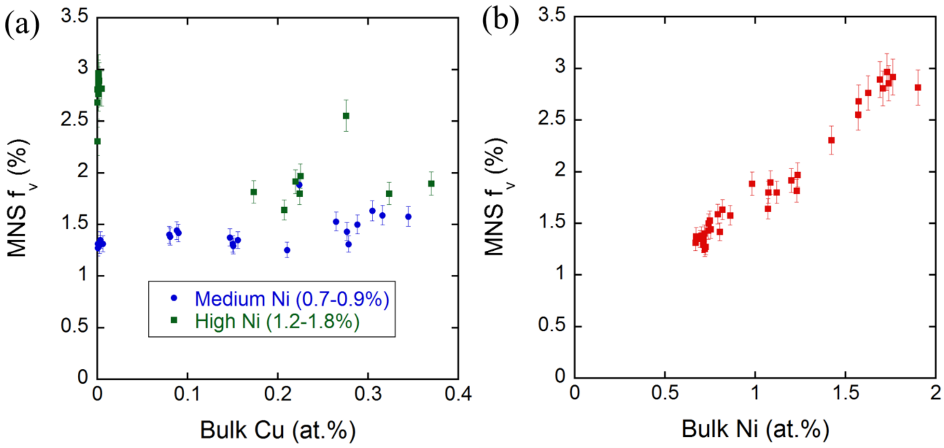

Figure 2.11. MNS f_v from the very high ϕt_e condition as a function of a) Cu and b) Ni.

As noted previously, the total APT local chemistries vary from tip to tip, allowing characterization of the effects of both smaller single-alloy and larger alloy-to-alloy changes in composition. Figure 2.12 shows the precipitate individual solute f_v as a function of local composition for Cu (a), Ni (b), Mn (c), and Si (d). The plots of f_v versus bulk solute for Cu and Ni form a tight band in both cases, with least square fit slopes of 0.95 and 0.89, combined with thresholds of ≈ 0.01% Cu and ≈ 0.05% Ni, respectively (Fig. 10 a and b). In the case of Mn, all the alloys fall into one tight band, except for the highest Ni content, Cu-free (CM6) steel (Fig. 10c). The least square fit slope for the 0.8-1.2% Ni steels is 0.36 with an intercept of Mn ≈ -0.32%. The corresponding least squares fit Mn slope for the highest Ni content, Cu-free alloy is 0.80 with an intercept of Mn ≈ 0.17%. There are also two bands for the effect of Si on f. The medium Ni content steels with varying Cu content (LG, LH, LI, LC) fall along a line with a least square fit slope of 0.80 and a threshold of Si ≈ 0.07%, while the least square fit slope is 0.63 with an intercept of Si ≈ -0.14%, for the highest Ni content, Cu-free and high Ni-Cu content steels (CM6 and LD). Note the high Ni content fits are less reliable in the cases of Mn and Si since they are for only 1 and 2 alloys, respectively.

The very systematic behavior in precipitate f_v as a function of alloy composition will be used to develop physically based chemistry factors for advanced ΔT embrittlement models. The most significant observation is that the precipitation behavior is consistent with two Mn-Ni-Si intermetallic phases at ≈ 550K that are found in Thermocalc evaluations. Further at very high ϕt_e, Ni has a dominant role in precipitation, compared to Mn and Si, in terms of both the strength of the effect itself, and the wider range of Ni content in the steels studied here. These results are also very consistent with previous observations on the effect of Ni and Mn on both the precipitates and hardening and also help clarify the role of Si [3, 5–7, 14–23]. However, since developing robust physically based chemistry factor will require evaluation of a wider range of alloy compositions and irradiation conditions; this will not be discussed further.

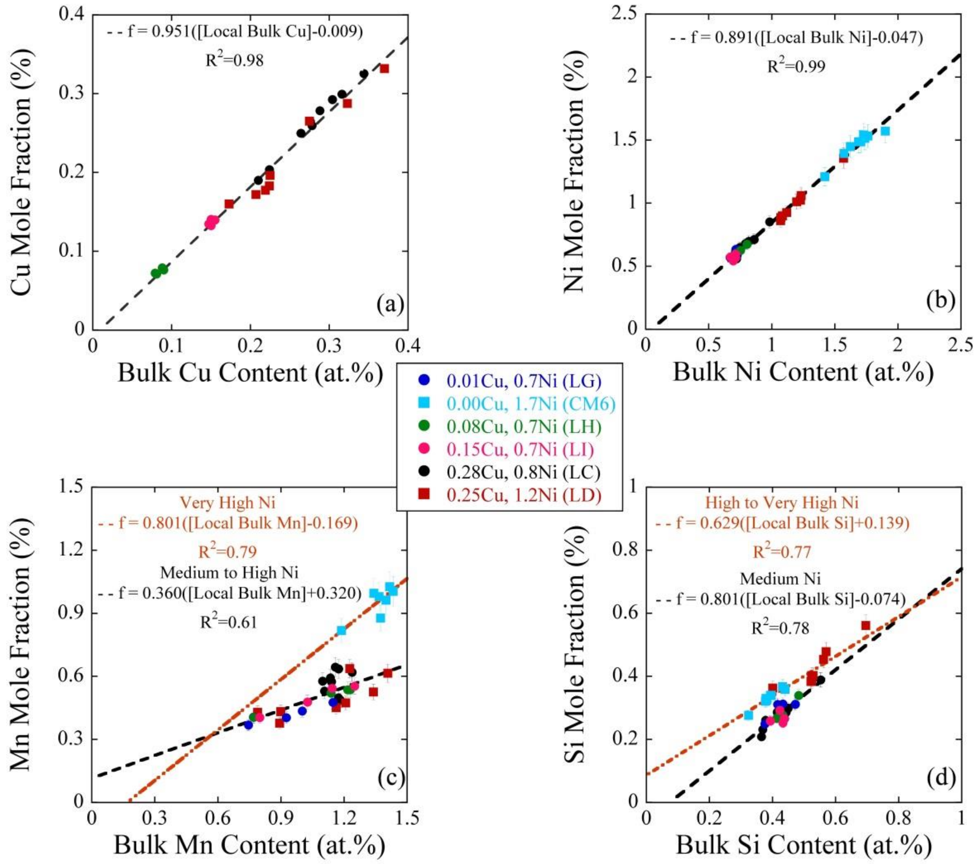

Figure 2.12. The precipitate f_v for individual elements as a function of their corresponding bulk solute compositions.

2.8 Effect of low Ni

The strong effect of Ni at very high ϕt_e was clearly demonstrated in section 2.6. Two high Cu (0.4%) alloys with 0.00% and 0.18% Ni were also included in the very high ϕt_e ATR1 irradiation and allow for the study of Cu, Mn and Si precipitation when the Ni is significantly reduced or even removed.

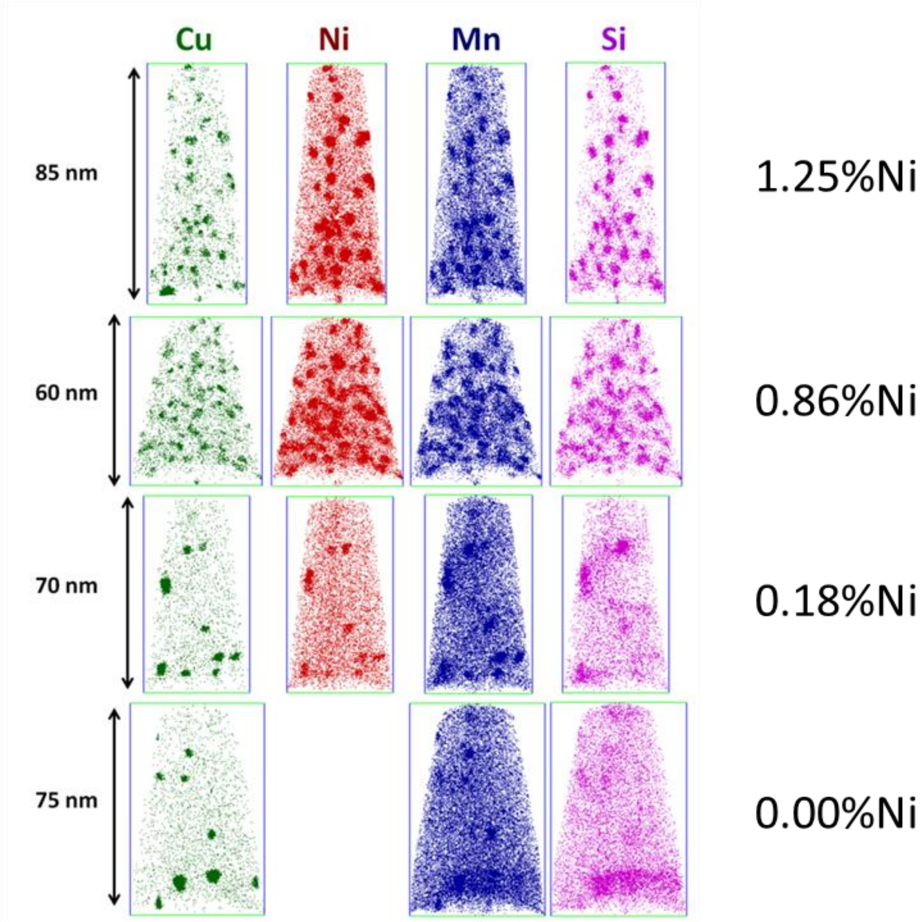

Figure 2.13. Atom maps from the 4 high Cu steels with a) 1.25% Ni, b) 0.86% Ni, c) 0.18% Ni, and d) 0.00% Ni.

Atom maps from the 4 high Cu (0.3-0.4%) steels with varying Ni contents from 0.00% to 1.25% can be seen in Figure 2.13. Note that results from the top two samples, LD and LC, were discussed in significant detail in sections 2.4 - 2.6. The atom maps demonstrate a number of differences at low vs high Ni. The Mn and in particular Si are much more diffuse around the Cu clusters in the lower Ni steels and the precipitate N is significantly reduced. This reduction in number density, coupled with a constant amount of precipitated Cu in all cases, results in larger precipitates in the low Ni steels, as seen quantitatively in Figure 2.14. The reason for the increase in <d> and reduction in N when going from 0.8 to 1.2% Ni is likely due to the earlier coarsening that is occurring in the highest Ni steel. A reduction in precipitate number density with decreases in bulk Ni content has been reported previously for thermally aged steels [24]. Mn and Ni have been shown to reduce the Fe-Cu interfacial interface energy by forming a shell around the Cu-rich core [5, 18, 25, 26]. The nucleation step for Cu-rich precipitates is likely more difficult at lower Ni contents, resulting in a reduced number density.

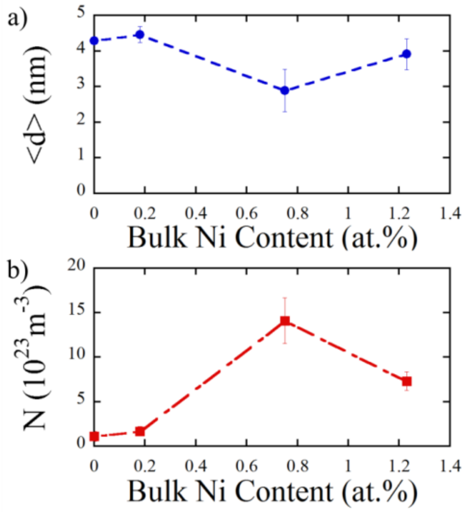

Figure 2.14. Average precipitate size and number density as a function of Ni for the 4 high Cu steels.

Figure 2.15 shows the total f_v for the 4 high Cu steels. The differences in Cu mole fraction are caused by differences in bulk Cu of the measured APT tips. The more important point is that the Mn and Si which have precipitated are significantly reduced at lower Ni contents.

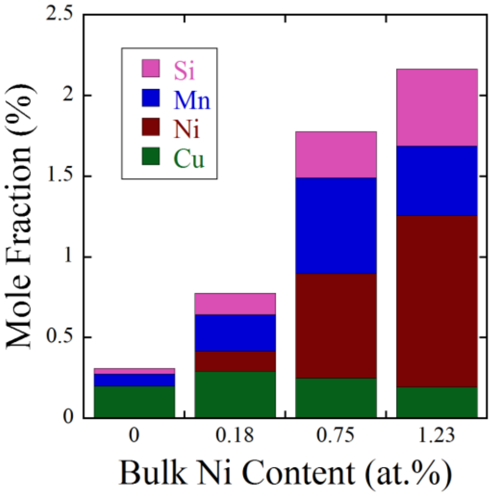

Figure 2.15. Precipitate f_v vs bulk Ni for steels all containing 0.3-0.4% nominal Cu.

As results from the two higher Ni steels have already been discussed, the two lower Ni steels will now be examined in more detail. First, as shown in Figure 2.15, the precipitates in the two lower Ni steels are dominated by Cu. The precipitates are ≈ 65% and ≈ 40% Cu in the Ni-free and 0.18% Ni steel, respectively. The balance of the precipitates is made up of Mn, Ni and Si, with Mn making up ≈ 2-3x that of the Si. Precipitates from the Ni free steel can be seen in more detail in Figure 2.16. One example is given of precipitates likely on a dislocation and one example of a precipitate not on a dislocation are shown in a) and b), respectively. While APT cannot detect dislocations themselves, they can observe them if the dislocations are enriched in solutes. In the case of Figure 2.16a, Mn and Si can be seen to be enriched along a line, with two large Cu precipitates also on the same line.

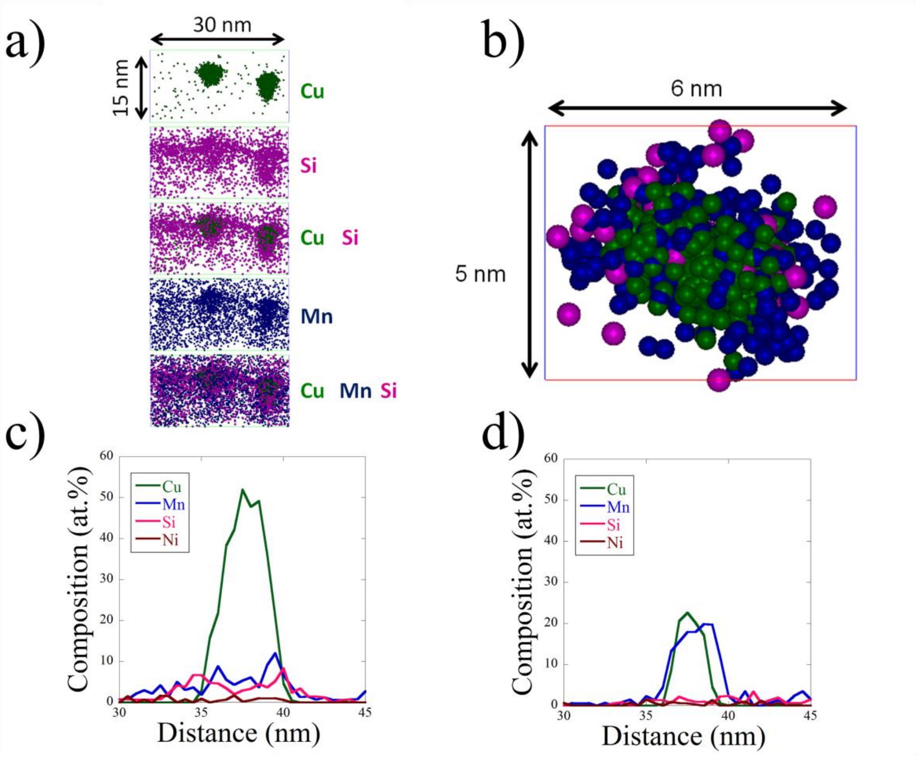

Figure 2.16. Blown up pictures of precipitates from the Ni steel (LA) showing a) precipitates and Si enrichment along a dislocation and b) a precipitate in the matrix.

A line compositional profile through one of the precipitates in Figure 2.16a is seen in Figure 2.16c. In this case, Si is enriched up to ≈ 7% with peaks on both sides of the precipitate, forming what appears to be a shell. On the other hand, the line compositional profile through the precipitate in Figure 2.16b, shown in Figure 2.16d, shows very little Si enrichment to the Cu-rich cluster. Thus, Si only appears to associate with the Cu-rich precipitates if they nucleate along dislocations, where Si would likely segregate with or without a precipitate present. For precipitates not on dislocations, there is very little Si enrichment when Ni is not present. In either case, Mn segregates to the Cu-rich clusters and in some case, as seen in Figure 2.16b and d, can exist in equal amounts as the Cu.

The 0.18% Ni steel shows very similar trends to the 0.00%Ni steel. Two precipitates, and corresponding line compositional profiles through them, from the 0.18% Ni steel are shown in Figure 2.17. Figure 2.17a and Figure 2.17c show a smaller precipitate and the corresponding line compositional profile showing very little Ni enrichment. In this case, there is again significant Mn enrichment that appears to form a shell, but also shows significant enrichment through the core of the precipitate. The Ni composition peaks at ≈ 6% with even less Si. A separate, much larger precipitate, seen in Figure 2.17b contains a Cu-rich portion and a Mn-Ni-Si rich portion, similar to that found in

Figure 2.7. In this case, the Ni is approximately equal to the Mn in the Mn-Ni-Si portion of the precipitate, even though it is present in a very dilute amount of 0.18% vs 1.4% for Mn. In addition, the Si is significantly enriched in the Mn-Ni-Si portion, representing 27% of the Mn, Ni and Si, with the Ni and Mn being approximately equivalent. In the Cu-rich portion of the precipitate, the Mn is much more enriched compared to the Ni and Si.

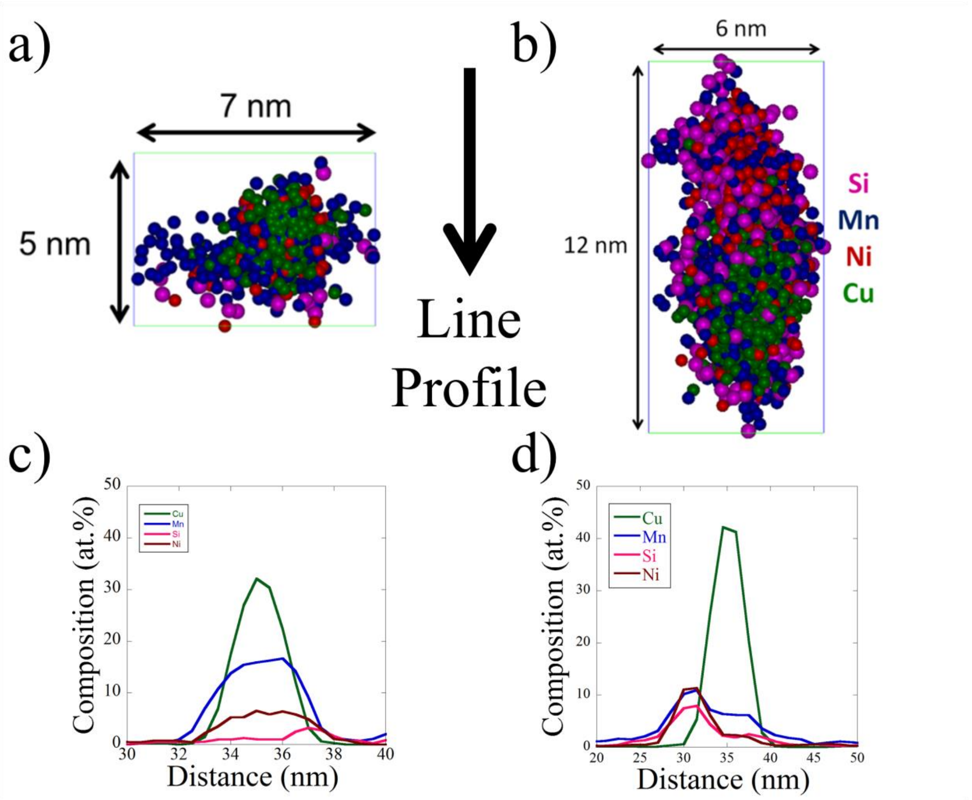

Figure 2.17. Line profiles through precipitates in the 0.18% Ni steel (LB) showing a small precipitate with little Ni and b) a larger precipitate with a Mn-Ni-Si appendage.

While the precipitates in the Ni free steel are likely just Cu precipitates that have been enriched in Mn and Si, the 0.18% Ni steel clearly contains some precipitates with a Mn-Ni-Si appendage. Interestingly, comparing the relative Mn-Ni-Si in just the MNS appendage to the results from the medium Ni (0.7-0.8%) steels presented in section 2.5, shows very similar results, as seen in Table 2.8, though the Ni is less enriched and Si more enriched in LB than in the medium Ni steels (LC, LG, LH, LI)..

Table 2.8. Relative Mn-Ni-Si in the precipitates for the various steels at very high ϕt_e.

Steel	Measured APT Bulk Ni	Mn	+/-	Ni	+/-	Si	+/-
LB (MNS Appendage)	0.18	35.5	*	37.0	*	27.4	*
LC	0.80	37.5	1.8	43.9	1.2	18.6	1.1
LG	0.71	31.3	2.9	46.2	1.5	22.5	1.6
LH	0.73	37.5	2.4	42.9	1.4	19.6	1.1
LI	0.70	35.3	4.4	43.9	2.5	20.9	1.9

*Note that the uncertainty cannot be measured for the LB appendage because only1 was measured.

One final interesting point to note in the lower Ni steels is the presence of a high density of dislocation loops, which are enriched in Mn, Ni and Si and also appear to act as nucleation sites for Cu precipitates. An example run of the 0.18% Ni steel with a high loop density, along with a higher magnification image of one of the loops are seen in Figure 2.18 and Figure 2.19, respectively. It should be noted that 4 loops were observed in this small run, while 1 loop was observed in every ≈ 5-10 runs for the medium and high Ni steels. Unfortunately, only several APT samples were taken from these two alloys, which makes it difficult to determine whether they actually have a higher loop density or whether the APT randomly sampled a small region containing more loops. Post irradiation annealing results show that the hardening features in the low Ni steels are much more stable than the higher Ni steels at annealing temperatures of 400-450°C. Whether or not the loop density is in fact higher, the reason behind the higher density, and the high temperature stability of the loops are ongoing investigations and will not be discussed further.

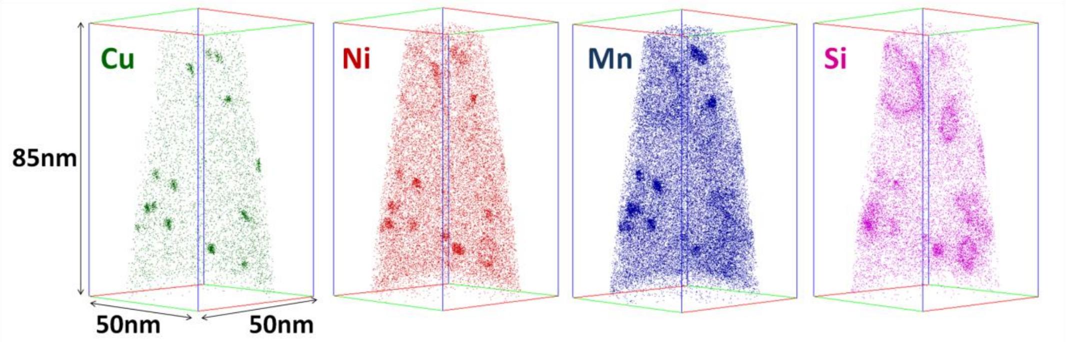

Figure 2.18. Atom maps from the high Cu, 0.18% Ni steel with a high density of dislocation loops.

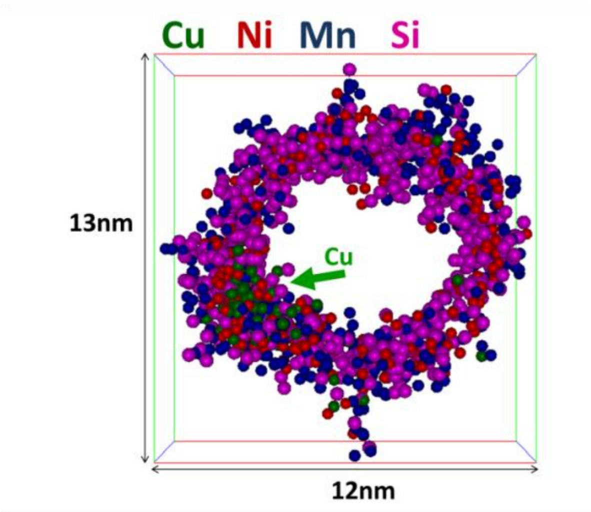

Figure 2.19. Magnified view of a dislocation loop from the tip seen in Figure 2.18 showing Mn, Ni and Si enrichment along the entirety of the loop along with a Cu-rich precipitate.

2.9 Results from Surveillance Program Irradiation

In addition to the high flux test reactor irradiations, material from a surveillance irradiation was also examined. This material, from the Ringhals reactor in Sweden, was provided by Oak Ridge National Lab and was irradiated at a flux of 1.5×10^{11} n/cm^2-s to a ϕt of 6.1×10^{19} n/cm^2. The flux in this case was > 3 orders of magnitude lower than the test reactor irradiations. The measured bulk APT composition of the low-Cu steel is given in Table 2.9.

Table 2.9. Measured APT bulk composition for the Ringhals surveillance specimen.

Specimen	Cu	+/-	Ni	+/-	Mn	+/-	Si	+/-
Ringhals	0.03	0.01	1.43	0.08	1.12	0.18	0.26	0.06

Atom maps from one of the Ringhals steel can be seen in Figure 2.20. Even though this steel is low in Cu, containing ≈ 0.03%, Cu can still be seen in some of the clusters. The Mn, Ni and Si is clearly clustered and P is also seen to be enriched in some of the clusters. In addition, two dislocations can be seen that are enriched in Ni, Mn, Si and P.

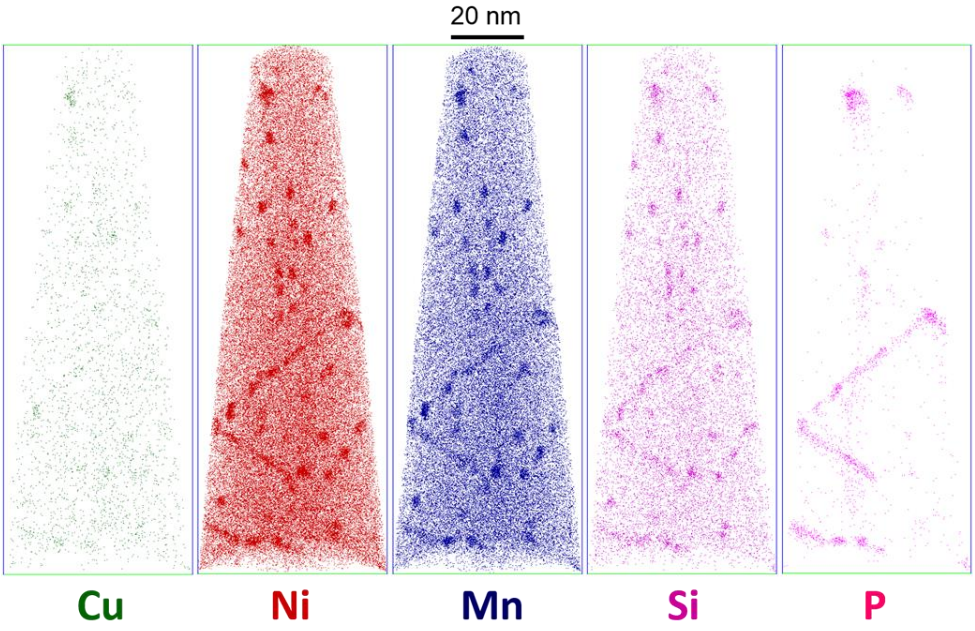

Figure 2.20. Atom maps from the Ringhals surveillance irradiated specimen.

The most comparable UCSB steel is CM6, which nominally contains 0.02%Cu and 1.74%Ni. Figure 2.21 shows the measured f_v for the Ringhals steel, (blue circle) and various conditions of CM6 (all other points) as a function of ϕt_e. The different colors and shapes represent conditions with different ϕ, showing a ϕ range from 0.1x10^{12} n/cm^2-s (Ringhals) to 230x10^{12} n/cm^2-s (ATR1). In addition, the relative precipitate compositions for the Ringhals and CM6 ATR1 conditions are shown in Table 2.10.

Table 2.10. Relative amount of Mn, Ni and Si in the clusters for the Ringhals N180 condition and the CM6 ATR1 condition.

Steel	Condition	Mn	Ni	Si
Ringhals	N180	32.9	55.2	11.9
CM6	ATR1	35.5	52.6	11.9

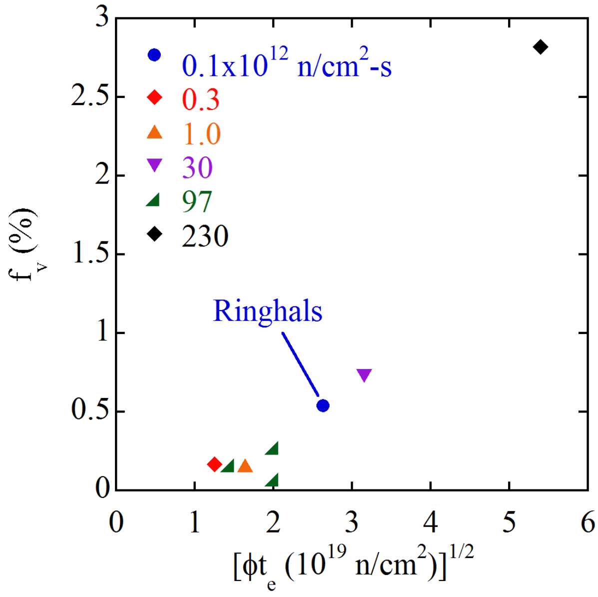

Figure 2.21. f_v as a function of ϕt_e for Ringhals N180 (blue circle) and various conditions of CM6 (all others).

The very consistent precipitate compositions and f_v between the Ringhals and CM6 precipitates, again with ϕ differences between the Ringhals and ATR1 condition of 4 orders of magnitude, offer further evidence that the precipitates in these irradiated steels are thermodynamic phases and are not significantly altered at high ϕ.

2.10 Hardening

Relating the precipitates to hardening will briefly addressed here to show the enormous amount of hardening present in the very high ϕt_e test reactor irradiated steels. The Russell-Brown model relates changes in yield stress ($\Delta\sigma_y$) to the precipitate radius (r) and volume fraction (f_v) of precipitates using the following relation, $\Delta\sigma_y \propto \sqrt{f_v}/r$ [27]. $\Delta\sigma_y$ vs $\sqrt{f_v}/r$ is plotted in Figure 2.22 for the 6 UCSB steels with Ni contents > 0.7% presented in this report (LC, LD, LG, LH, LI, CM6). Included with the ATR1 and TU data are data from previous UCSB irradiations including data from BR2, which includes the G1 condition, and the IVAR program. Note that the IVAR and some of the BR2 microstructure and hardening data were taken by past staff and students of the UCSB MRPG group. The correlation between the precipitates and hardening is very clear and makes a compelling case that the hardening is primarily caused by the precipitates. In addition, the ATR1 irradiation shows enormous hardening of up to almost 700 MPa. The typical relation for converting $\Delta\sigma_y$ to ΔT is given by [28]

$$\Delta T(°C) \approx 0.68\Delta\sigma_y(MPa) \tag{2.1}$$

Using this relation results in a ΔT of ≈ 460°C for the Cu-free, highest Ni steel (CM6) in the ATR1 condition. It should again be stressed that the ATR1 condition, even when adjusted for ϕ, has a ϕt_e well above any which would be experienced by an in-service vessel at 80 years. These data is presented not to suggest actual vessels will experience such a large $\Delta\sigma_y$ and ΔT, but to show the importance of including these phases in embrittlement prediction models for extended life.

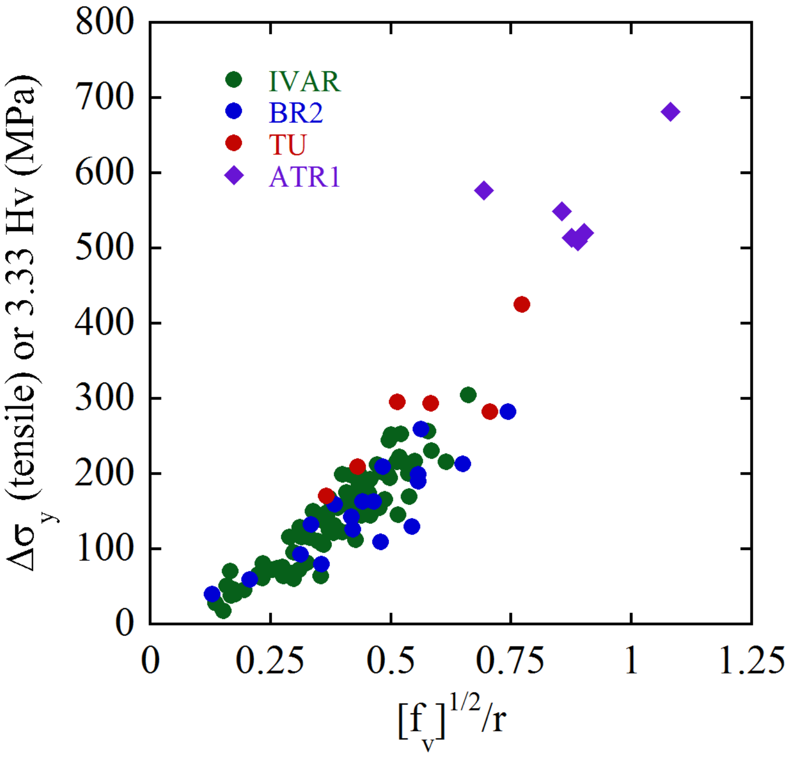

Figure 2.22. Yield stress increase after irradiation vs $\sqrt{f_v}/r$ for steels in a number of different irradiation conditions.

2.11 *Summary and Conclusions*

Large mole fractions of Mn-Ni-Si dominated LBP precipitates form in both Cu-free and Cu-bearing RPV steels at very high ϕt_e. Consistent with longstanding predictions:

- In Cu-free steels the MNSP likely evolve from defect-solute cluster matrix feature precursors that constitute only a small $f_v \approx 0.1\%$ at medium ϕt_e, but subsequently grow to much larger mole fractions at very high ϕt_e.

- Cu catalyzes the initial formation of MNSP. This is especially the case of rapidly forming precipitates at the high supersaturations of Cu. Thus at the high flux-high ϕt condition in this study, Cu and Ni are the primary compositional variables leading to large mole fractions of MNSP.

- However, since the precipitates are dominated by Mn-Ni-Si, Cu has a much weaker effect at very high ϕt_e, while Ni has the major influence on the f.

- The relative amounts of Mn, Ni and Si are very consistent with known intermetallic phases. The precipitates in the high Ni-Cu content (LD) steel are close to G phase ($Mn_6Ni_{16}Si_7$), while they are close to the Γ_2 phase ($Mn(Ni_xSi_{1-x})_2$) in the highest Ni content, Cu-free (CM6) steel. Thermocalc predictions for these two steels are very consistent with the experimentally found compositions. The precipitate compositions in the other medium Ni content alloys were in reasonably good agreement with the Si-rich end of the Γ_2 phase field although the Thermocalc predictions vary somewhat from these compositions in this case.

- Cu-rich precipitates still formed in the Ni-free and low Ni steels, though at a much lower number density than the medium and high Ni steels. In addition, while Mn was found to enrich the Cu-rich precipitates in all cases, the Si was only associated with them if they were nucleated along a dislocation. An addition of only 0.18% Ni resulted in a Mn-Ni-Si appendage forming on one of the Cu-rich precipitates.

- A low Cu surveillance steel irradiated to a fluence of $6.1\text{x}10^{19}$ n/cm2 contained large f_v of MNSP with compositions very similar to those found in the Cu-free, high Ni steel (CM6) in the ATR1 condition. Thus, ϕ does not appear to significantly alter the character of MNSPs.

- The increase in precipitate mole fractions leads to correspondingly large increases in hardness; hence, also leads to severe embrittlement.

2.12 References

1. Eason ED, Odette GR, Nanstad RK and Yamamoto T. "A physically based correlation of irradiation-induced transition temperature shifts for RPV steels," Oak Ridge National Lab, 2007; ORNL/TM-2006/530.
2. Eason ED, Odette GR, Nanstad RK and Yamamoto T. "A physically-based correlation of irradiation-induced transition temperature shifts for RPV steels", J. Nucl. Mater. 2013;433:240–254.
3. Odette GR and Lucas GE. "Recent Progress in Understanding Reactor Pressure Vessel Steel Embrittlement", Radiat. Eff. Defects Solids 1998;144(1-4):189–231.
4. Odette GR and Lucas GE. "Recent Advances in Predicting Embrittlement of Reactor Pressure Vessel Steels", In: Proceedings of the 2nd International Symposium on Environmental Degradation of Materials for Nuclear Power Systems-Water Reactors, ANS; 1986. p. 295.

5. Liu CL, Odette GR, Wirth BD and Lucas GE. "A lattice Monte Carlo simulation of nanophase compositions and structures in irradiated pressure vessel Fe-Cu-Ni-Mn-Si steels", Mater. Sci. Eng. A 1997;238(1):202–209.

6. Miller MK and Russell KF. "Embrittlement of RPV steels: An atom probe tomography perspective", J. Nucl. Mater. 2007;371(1-3):145–160.

7. Miller MK, Russell KF, Sokolov MA and Nanstad RK. "APT characterization of irradiated high nickel RPV steels", J. Nucl. Mater. 2007;361:248–261.

8. Wirth BD, Odette GR, Pavinich W, Lucas GE, et al. "Small Angle Neutron Scattering Study of Linde 80 RPV Welds", In: 18th ASTM International Symposium on the effects of radiation on materials, ASTM STP-1325; 1999. p. 102.

9. Miller MK, Powers KA, Nanstad RK and Efsing P. "Atom probe tomography characterizations of high nickel, low copper surveillance RPV welds irradiated to high fluences", J. Nucl. Mater. 2013;437(1-3):107–115.

10. Xiong W, Ke H, Wells PB, Barnard L, et al. "Thermodynamic models of low temperature Mn-Ni-Si precipitation in reactor pressure vessel steels", MRS Commun. 2014;4(3):101–105.

11. Sprouster DJ, Sinsheimer J, Dooryhee E, Ghose SK, et al. "Structural Characterization of Nanoscale Intermetallic Precipitates in Highly Neutron Irradiated Reactor Pressure Vessel Steels", Scr. Mater. 2016;113:18–22.

12. Gupta KP. "The Mn-Ni-Si (Manganese-Nickel-Silicon) System", J. Phase Equiilibria Diffus. 2006;27(5):529–534.

13. Hu B, Xu H, Liu S, Du Y, et al. "CALPHAD : Computer Coupling of Phase Diagrams and Thermochemistry Experimental investigation and thermodynamic modeling of the Mn – Ni – Si system", CALPHAD Comput. Coupling Phase Diagrams Thermochem. 2011;35(3):346–354.

14. Odette GR. "Radiation Induced Microstructural Evolution in Reactor Pressure Vessel Steels", Mater. Res. Soc. Symp. Proc. 1995;373:137–148.

15. Odette GR and Wirth BD. "A computational microscopy study of nanostructural evolution in irradiated pressure vessel steels", J. Nucl. Mater. 1997;251:157–171.

16. Odette GR. "Modeling of Irradiation Embrittlement in Pressure Vessel Steels", In: Irradiation Effects on Pressure Vessel Steels, IAEA IRRWG-LMNPP-98-3; 1998. p. 438.

17. Mader E. "Kinetics of irradiation embrittlement and the post-irradiation annealing of nuclear reactor pressure vessel steels" [PhD Thesis]. University of California, Santa Barbara, 1995.

18. Odette GR, Liu CL and Wirth BD. "On the Composition and Structure of Nanoprecipitates in Irradiated Pressure Vessel Steels", Mater. Res. Soc. Symp. Proc. 1997;439:457–469.

19. Hyde JM, Ellis D, English CA and Williams TJ. "Microstructural Evolution in High Nickel Submerged Arc Welds", In: 20th ASTM International Symposium on effects of radiation on nuclear materials, ASTM STP 1405; 2001. p. 262.

20. Hyde JM, Sha G, Marquis E a., Morley a., et al. "A comparison of the structure of solute clusters formed during thermal ageing and irradiation", Ultramicroscopy 2011;111(6):664–671.

21. Styman PD, Hyde JM, Wilford KB and Smith GDW. "Quantitative methods for the APT analysis of thermally aged RPV steels", Ultramicroscopy 2013;132:258–264.

22. Carter RG, Soneda N, Dohi K, Hyde JM, et al. "Microstructural characterization of irradiation-induced Cu-enriched clusters in reactor pressure vessel steels", J. Nucl. Mater. 2001;298(3):211–224.

23. Buswell JT, Phythian WJ, McElroy RJ, Dumbill S, et al. "Irradiation-induced microstructural changes, and hardening mechanisms, in model PWR reactor pressure vessel steels", J. Nucl. Mater. 1995;225:196–214.

24. Osamura K, Okuda H, Asano K, Furusaka M, et al. "SANS Study of Phase Decomposition in Fe-Cu Ally with Ni and Mn Addition", ISIJ Int. 1994;34(4):346–354.

25. Zhang C and Enomoto M. "Study of the influence of alloying elements on Cu precipitation in steel by non-classical nucleation theory", Acta Mater. 2006;54(16):4183–4191.

26. Wirth BD. "On the Character of the Nano-Scale Features in Reactor Pressure Vessel Steels" [PhD Thesis]. University of California, Santa Barbara, 1998.

27. Russell KC and Brown L. "A dispersion strengthening model based on differing elastic moduli applied to the iron-copper system", Acta Metall. 1972;20(7):969–974.

28. Odette GR and He MY. "Cleavage toughness master curve model", J. Nucl. Mater. 2000;283-287:120–127.

3. POST IRRADIATED ANNEALING STUDIES

3.1 Introduction

One potential barrier to extending nuclear light water reactors lifetimes to 80 years is embrittlement of their massive reactor pressure vessel (RPV) [1]. Embrittlement is primarily due to the formation of nm-scale precipitates, which cause hardening and a corresponding increase in the ductile to brittle transition temperature [2, 3]. A major effect of irradiation is to increased solute mobility due to radiation enhanced diffusion (RED). RED leads to hardening by Cu-rich precipitates (CRP) at low to intermediate neutron fluence (ϕt) in steels with more than ≈ 0.07% Cu [4]. Cu is highly insoluble at RPV service temperatures (T_i) of ≈ 290°C and quickly precipitates as coherent bcc clusters that are also enriched in Mn, Ni and Si. Solute-defect cluster complexes, known as stable matrix features, thought to form in displacement cascades, also cause modest hardening, increasing roughly with the square root of ϕt, in the low to intermediate ϕt range and in both low Cu and Cu bearing steels [3].

A main objective RPV life extension is predicting embrittlement at low service flux (ϕ) and high ϕt, where new embrittlement mechanisms may emerge. Notably, large volume fractions (f_v) of what are thought to be intermetallic Mn-Ni-Si precipitates (MNSPs), long ago predicted by Odette [5], form at very ϕt in high ϕ test reactor irradiations, both in low Cu and Cu-bearing steels [6]. They have also been observed in much lower ϕ test reactor irradiations [7–9] However, MNSPs are not currently treated in US embrittlement prediction models [1]. As modeled by Odette, MNSPs are enhanced in low alloy RPV steels by low ϕ, low T_i, high Ni and even trace amounts of Cu. The Cu concentration of dissolved Cu in RPV steels range from ≈ 0.01 to 0.25 at.%. The corresponding concentrations of Mn + Ni + Si typically range from 2 to 4%. These solutes continue to slowly precipitate long after the matrix Cu is depleted. The MNSPs form as a separate appendage phase on the CRPs in Cu bearing steels, as also observed in thermal ageing studies [10], low flux power reaction surveillance irradiations [7], and high flux test reactor irradiations [6]. Although the existence of MNSPs is not in question, there are a number of unresolved issues regarding their detailed character and formation mechanisms.

Some have argued that MNSPs are not thermodynamically stable phases, but are rather non-equilibrium solute clusters primarily formed by a radiation induced segregation (RIS) mechanism [11–14]. Specifically these models suggest either than Mn-Ni clusters are not thermally stable in Fe [11, 12], or that they are only stable at very low temperatures and high solute concentration and thus require RIS to form at irradiation induced dislocation loops [13, 14]. In contrast, equilibrium thermodynamic models predict that RED results in large MNSP f_v at the low RPV operating temperatures of ≈ 290°C [15]. Notably the predicted equilibrium precipitate f_v and compositions are in good agreement with recently acquired very high fluence atom probe tomography (APT) data that is hypothesized to be close to saturation [6]. Recent X-ray diffraction and scattering experiments confirm thermodynamic predictions that the MNSPs have Γ_2 or G-phase intermetallic crystal structures [16].

Post irradiation annealing (PIA) can provide significant additional insight into the nature of the MNSPs. For example, clusters that form through a RIS mechanism should not be stable during PIA even at ≈ 290°C. However, very slow thermal diffusion kinetics precludes conducting meaningful experiments at such low annealing temperatures (T_a). Unfortunately, while diffusion rates increase with higher T_a the equilibrium MNSP phase fractions are also reduced. Thus dissolution of what are argued to be RIS formed Mn-Ni-(Si) clusters following short term anneals at T_a from 450-500°C [17, 9], or in low solute content model alloys at T_a = 400°C [18], does not prove that they are thermodynamically unstable at lower service T_i. In addition, due to their small radii (r) of ≈ 0.75-1.5 nm, and the Gibbs Thomson effect, even if MNSPs are bulk equilibrium phases, they will dissolve if they are below the critical radius in a solute depleted matrix. This is discussed further in Section 3.4.2.

Because of the slow diffusion rates below ≈ 450°C very long time (t_a) PIA is required to distinguish kinetic from thermodynamic effects, and to map MNSP phase boundaries for comparison to thermodynamic models. It must be emphasized that it is absolutely critical to compare the PIA data to predictions of models that properly account for thermodynamics and dissolution kinetics. Note, achieving these fundamental objectives also supports refining predictive Mn-Ni-Si precipitation and PIA models, including for application to guiding embrittlement predictions and remediation treatments.

3.2 Materials and Methods

Two essentially Cu-free split-melt, bainitic RPV steels were studied. Their compositions are shown in Table 1. The split melt alloy microstructures and properties are fully representative of actual in service RPV steels. The two steels have similar compositions, with the exception of Ni, that nominally ranged from ≈ 0.69 at.% (medium) to 1.57 at.% (high). They were irradiated in the Advanced Test Reactor (ATR) to a very high $\phi t \approx 1.1 \pm 0.2 \times 10^{21}$ n/cm^2 at a high flux $\phi \approx 2.3 \pm 0.4 \times 10^{14}$ n/cm^2-s (E > 1MeV) nominally at ≈ 320 ±15°C [19]. The ϕt is ≈ 10 times higher than that expected for RPVs at extended life, while the corresponding ϕ is ≈ 5750 times higher than in typical RPV levels of $\phi \approx 4 \times 10^{10}$ n/cm^2-s. It is well established that higher ϕ delays precipitation to higher ϕt, with a ϕ-adjusted effective fluence (ϕt_e) roughly scaling as $\phi t_e \approx \phi t(\phi_r/\phi)^p$, where p ranges from ≈ 0.15 to 0.25 [2, 5, 6, 20–22]. Thus the effective ATR ϕt_e is estimated to be only ≈ 1.25 to 3 times the corresponding ϕt_e at 80 year vessel extended life [6]. In any event, the main purpose of the ATR irradiation was to generate significant quantities of MNSPs that could be readily characterized and modeled. As expected, atom probe tomography (APT) studies of the as-irradiated (AI) condition showed significant volume fractions of MNSPs [6]. The two steels were also characterized by APT or Energy Dispersive X-ray Spectroscopy (EDS) following PIA at 425°C for times of 1, 7, 17, 29 and 57 weeks. The goal was to observe the precipitate evolution over time while ensuring that any apparent precipitate stability is not caused by a slow solute diffusion and kinetics. Due to the limited amount of irradiated material, the PIA was performed on 1.5 mm punched discs, precluding direct microhardness measurements.

Table 3.1. Nominal steel compositions (at.%)

Alloy	Cu	Ni	Mn	Mo	P	C	Si	Fe
LG	0.01	0.69	1.36	0.31	0.009	0.73	0.43	bal.
CM6	0.02	1.57	1.50	0.31	0.012	0.68	0.33	bal.

3.2.1 Atom Probe Tomography

APT was used to measure the MNSP composition, size distribution and average size (<r>), number density (N) and mole fraction (f), in the as-irradiated condition and following each anneal for all conditions but the longest annealing time at 57 weeks. The APT was carried out at the Center for Advanced Energy Studies (CAES) located in Idaho Falls, ID, with support from the Idaho National Laboratory managed Nuclear Scientific User Facilities Program. APT tips were FIBed using an FEI Quanta 3D FEG using 5kV and 2kV cleanup steps to reduce Ga damage. The tips were run in a CAMECA LEAP 4000X HR in voltage mode at a 20% pulse fraction at 50K. Note one sample of the high Ni steel (CM6), annealed for 27 weeks, was run in laser mode with a pulse energy of 75 pJ, a repetition rate of 250 kHz and a temperature of 40K, in anticipation that only a very low number density of MNSPs would remain at this condition, so a larger sample volume was needed to increase the probability of measuring them. However, an MNSP with similar size and composition was observed in a shorter voltage mode run as well. A full description of the APT analysis procedures can be found in [6].

APT reconstructions and analysis were performed using the CAMECA Integrated Visualization and Analysis Software (IVAS). The clusters were defined by the density based scanning method described elsewhere [23] with order = 5, d_{max} = 0.6 nm, N_{min} = 20-30, envelope = 0.6 nm. A constant d_{max} was used for all conditions. Decreases in d_{max} results in a lower f_v and <r>. Thus, measuring changes in f_v and <r> using a different d_{max} at each annealing interval, could introduce artificial biases. The main consequence of choosing a d_{max} that is too large is that random solute density variations in the matrix could be identified as clusters. Note in the AI condition, the solutes are highly depleted from the matrix, hence, the probability of identifying random fluctuations as clusters is negligible. However, significant precipitate dissolution occurs after long term annealing at 425°C, resulting in a much higher matrix solute contents. In these cases, all measured precipitates $N >> N_{min}$, so no random solute density fluctuations were incorrectly identified as precipitates.

The MNSP f_v was defined as the number of solute atoms in the clusters divided by the total number of atoms in the analyzed volume. Note procedure yields a mole fraction, that is not identical to the volume fractions, that are about 1% smaller or 5% higher for the G and Γ_2 phases, if their correct atomic densities were to be used. Most approaches to estimating cluster radii are based on spatial extent of the solutes, such as the Guinier radius. However, the low evaporation field of the precipitates results in a reduction in the local radius of curvature near the precipitate. This change in the local magnification factor results in a focusing of matrix atoms into the precipitate region on the detector, and is signaled by higher than physical atom densities within the clusters in the reconstructed dataset [24, 25]. These artifacts also result in the distortions of the shape and size of precipitates [26], including MNSPs, as well as their compositions, specifically the measured Fe content. Using the number of solute atoms to define the cluster size minimizes these field evaporation distortions. The number of solute atoms associated with each precipitate, corrected for efficiency, was determined and multiplied by the atomic volume of Fe. The precipitate r was then defined as the radius of a sphere encompassing the total solute volume. While these precipitates are thought to be intermetallic phases, differences in their average atomic volume versus Fe results in variations in r of less than ± 3%. The MNSP number density (N) was calculated by dividing the number of clusters in the dataset by the total volume of atoms in the tip. Precipitates on the edge of the tip are not included in the size distributions, or average <r>, but are counted as one half in the estimation of N.

3.2.2 Energy Dispersive X-ray Spectroscopy

At longer annealing times, a significant reduction in the precipitate number density was observed. While APT has very high spatial resolution and measures the detailed chemical nature of the precipitates, it has a very small sampling volume making it difficult to measure precipitates when they are present at very low number density ($< \approx 10^{22}$ m^{-3}). Thus, at the longest annealing time (57 weeks), Energy Dispersive X-ray Spectroscopy (EDS) was performed using an FEI TALOS F200x S/TEM in the Low Activation Materials Development and Analysis Laboratory at Oak Ridge National Laboratory.

3.3 Thermodynamic and Cluster Dynamics Modeling

Thermodynamic models, based on the Thermocalc enabled CALPHAD method, were used to guide the experimental design and to help analyze the annealing data [15]. The model predictions of the equilibrium f have been reported previously and compare favorably to the high ϕt ATR data [6]. The corresponding CALPHAD f for the two low Cu steels as a function of T_a are shown in Figure 3.1. CALPHAD predicts that only the Γ_2 phase (Mn_2Ni_3Si) is stable in the high Ni (CM6) steel, while the G phase ($Mn_6Ni_{16}Si_7$) persists only up to ≈ 390°C in the medium Ni (LG) steel; but at higher T_a, Γ_2 is more stable. Note that this calculation does not include non-equilibrium effects such as the interface energies of the small precipitates. Thus the f for the medium Ni steel is the sum of the Γ_2 and G phases at a given T_a. A very recent XRD study of the precipitates in the as irradiated condition found G phase precipitates in the medium Ni steel, while the high Ni steel contains the Γ_2 phase as predicted [16].

Figure 3.1 shows that the MNSPs in the medium Ni steel (LG) should completely dissolve above ≈ 415°C, while the Γ_2 phase in high Ni steel (CM6) are predicted to fully dissolves at ≈ 500°C. Again, because lower T_a results in lower solute diffusion rates, the isothermal annealing was carried out at an intermediate temperature of 425°C with the thermodynamic model predicting full dissolution in LG (medium Ni) and the possibility of some MNSPs remaining in CM6 (high Ni). Note that the complete MNSP dissolution of the phase in the medium Ni steel also acts as a kinetic marker to help estimate the effective diffusion distances at various annealing times that approximately apply to both alloys.

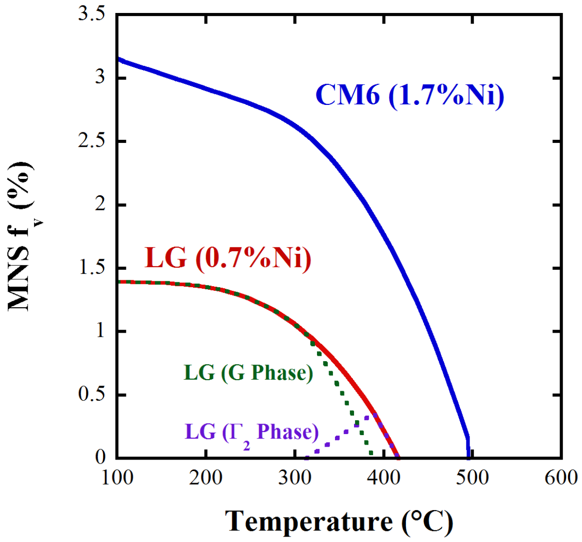

Figure 3.1. CALPHAD predictions of Mn-Ni-Si precipitate volume fraction as a function of annealing temperature for two Cu-free steels with varying Ni content.

Cluster dynamics (CD) modeling was also carried out to predict and interpret the MNSP dissolution and coarsening processes. Briefly, CD models the evolution of the MNSPs in discrete n-1, n and n+1 cluster sizes, where n is the number of atoms. Thus n ranges from 2 to n_{max} in a coupled set of n_{max} - 1 ordinary differential equations that incorporate n-dependent effective solute impingement and emission transition rate coefficients. In this case the solutes are treated as stoichiometric molecules of the pertinent phase. The CD method applied to modeling precipitation under irradiation is described elsewhere [27] and briefly summarized in the supplemental information. The CD model for annealing used here assumes thermal diffusion controlled kinetics, and requires only 4 key experimental input parameters: a) the effective thermal solute diffusion coefficient (D) derived from the literature; b) the effective solute equilibrium solubility (X_e), as determined by the free energy difference between the dissolved and precipitated effective solute states or the equilibrium phase diagram, determined from the Thermocalc database; c) the MNSP-Fe interface energy (γ) assumed to be the same is in the precipitation model; and, d) the as-irradiated MNSP size distribution, taken directly from the APT measurements. Thus the only fitted value is γ, which was derived independently from this annealing study and was also shown to be consistent with first principles calculations [27]. Thus the as-irradiated MNSP size distributions, bulk alloy composition and T_a fully mediate the MNSP evolution with T and t_a.

3.4 Results

3.4.1 Isothermal Annealing

Atom maps from the medium Ni steel (LG) in the AI and 425°C PIA conditions are shown in Figure 3.2. The clusters appear very diffuse following a one-week anneal with the Si near the MNSPs being the most diluted. The solutes in the medium Ni steel appear nearly entirely dissolved after the seven week anneal as predicted in Figure 1, with only weak indications of a small amount of solute clustering. While not measured, the solutes are very likely to be fully dissolved in the medium Ni LG steel after the 29 week anneal, given that the diffusion distances are about twice as large as those at seven weeks.

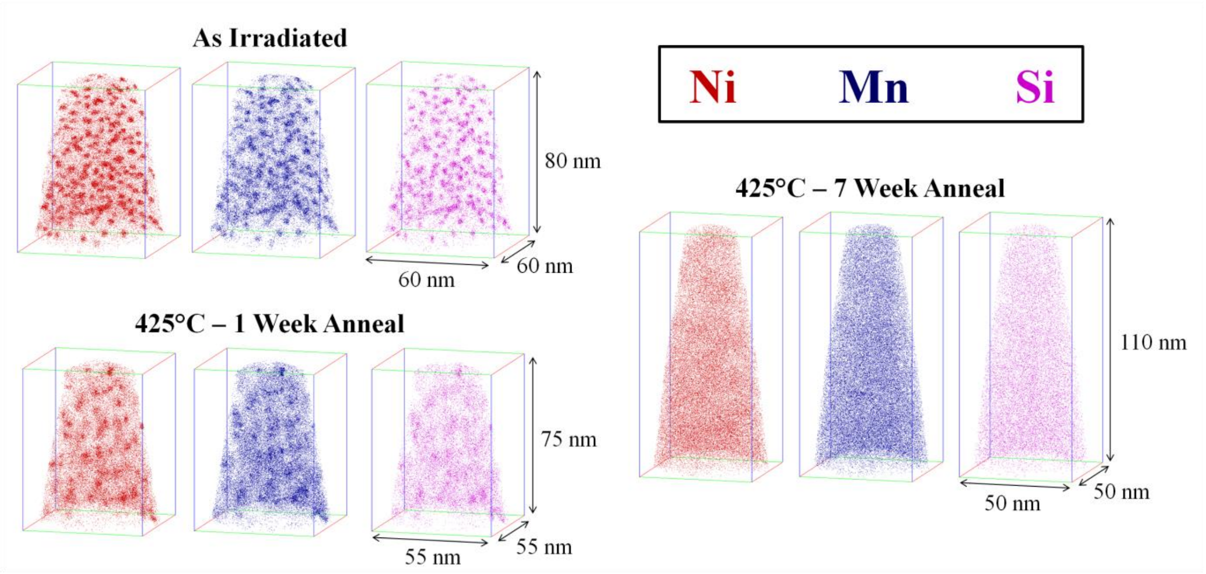

Figure 3.2. Atom maps for the Cu-free, medium Ni steel (LG) in the (a) AI condition, (b) 425°C - 1 week annealed condition, and (c) 425°C annealed - 7 week condition.

Atom maps for the low Cu, high Ni steel (CM6) in Figure 3.3 show much greater MNSP stability, with well-defined precipitates still remaining after PIA for 29 weeks. The <r>, N, and f_v are summarized in Table 3.2 and Figure 3.4. The lines in Figure 3.4 are the CD PIA predictions which will be discussed in Section 3.4.2. Both N and f decrease rapidly with the increasing t_a. There is a corresponding increase in <r>, that is primarily due to the dissolution of the smallest MNSPs, rather than significant coarsening, manifested as growth of the largest MNSPs. The average fractional precipitate compositions are also shown in Table 3.2. Note that while the standard IVAS reconstructions, as usual, suggest that there is a significant amount of Fe in all of the MNSPs, and while it is thought to be an APT artifact, the measured Fe content is included for those that wish to interpret the data differently. The Fe reconstructed in the MNSP region is mainly due to trajectory aberrations that focus matrix atoms into the precipitate, also leading to non-physically high atom densities, typically by factors of up to 2-3 [26].

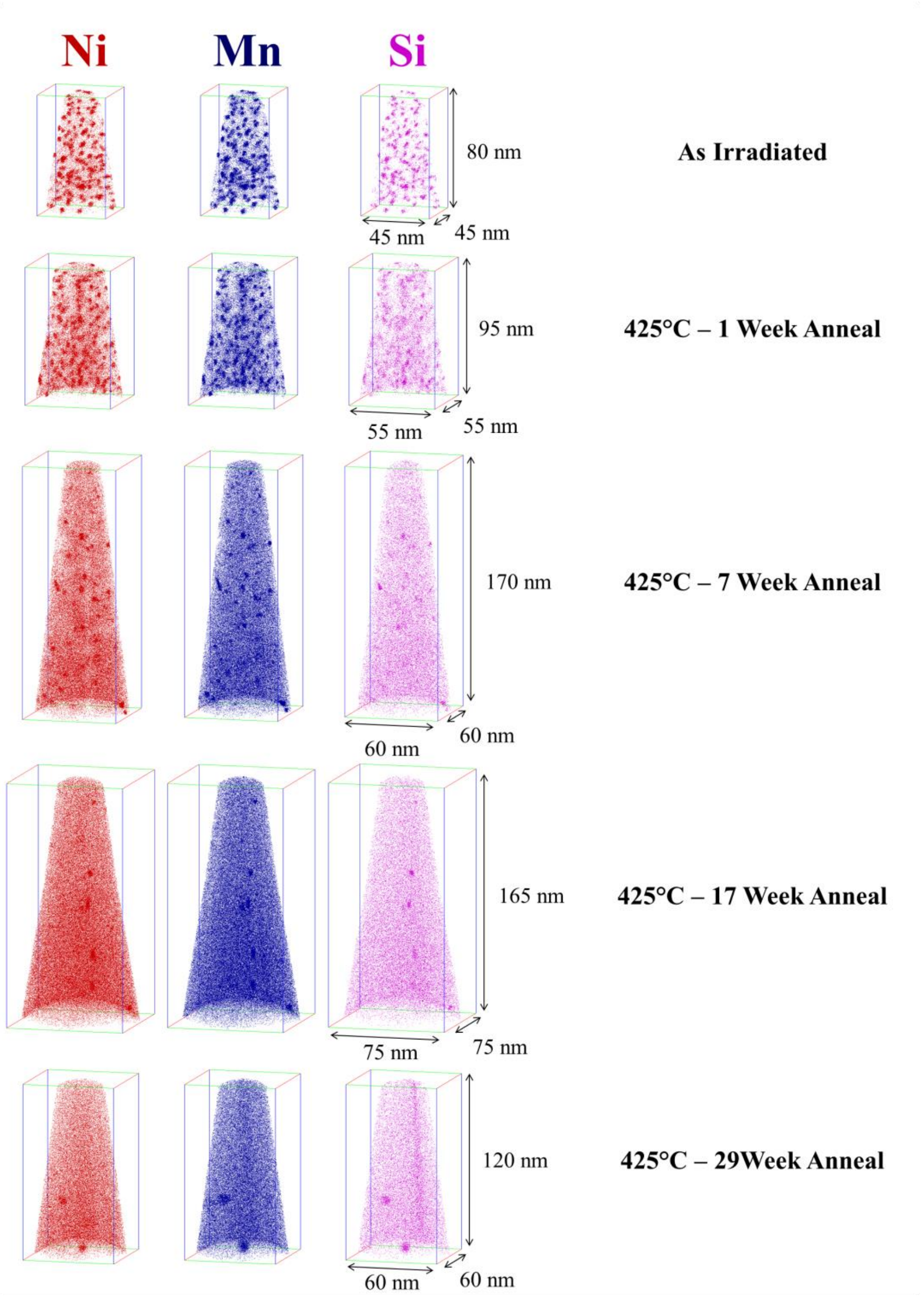

Figure 3.3. Atom maps for the low Cu, high Ni steel (CM6) in the (a) AI condition and 425°C annealed conditions at times of (b) 1 week, (c) 7 weeks, (d) 17 weeks and (e) 29 weeks.

Table 3.2. Precipitate summary for the high Ni steel (CM6) from the AI and 425°C annealed conditions.

				Precipitate Composition (at.%)							
t_a (wk)	<d> (nm)	N (10^{23}/m^3)	f_v(%)	Fe	Cu	Ni	Mn	Si	Mo	C	P
0	3.05	19.50	2.82	58.9	0.0	21.3	14.4	4.8	0.2	0.2	0.0
1	2.83	11.80	1.43	62.1	0.1	20.1	13.4	3.8	0.3	0.1	0.1
7	3.26	2.19	0.38	57.6	0.0	22.4	16.1	3.3	0.4	0.1	0.1
17	4.25	0.30	0.10	55.8	0.0	23.2	16.6	3.1	0.7	0.4	0.1
29	5.49	0.14	0.11	37.5	0.0	22.3	22.1	8.9	5.4	3.2	0.4

*Note that Fe is found in all the MNSPs, but it is thought to be an artifact

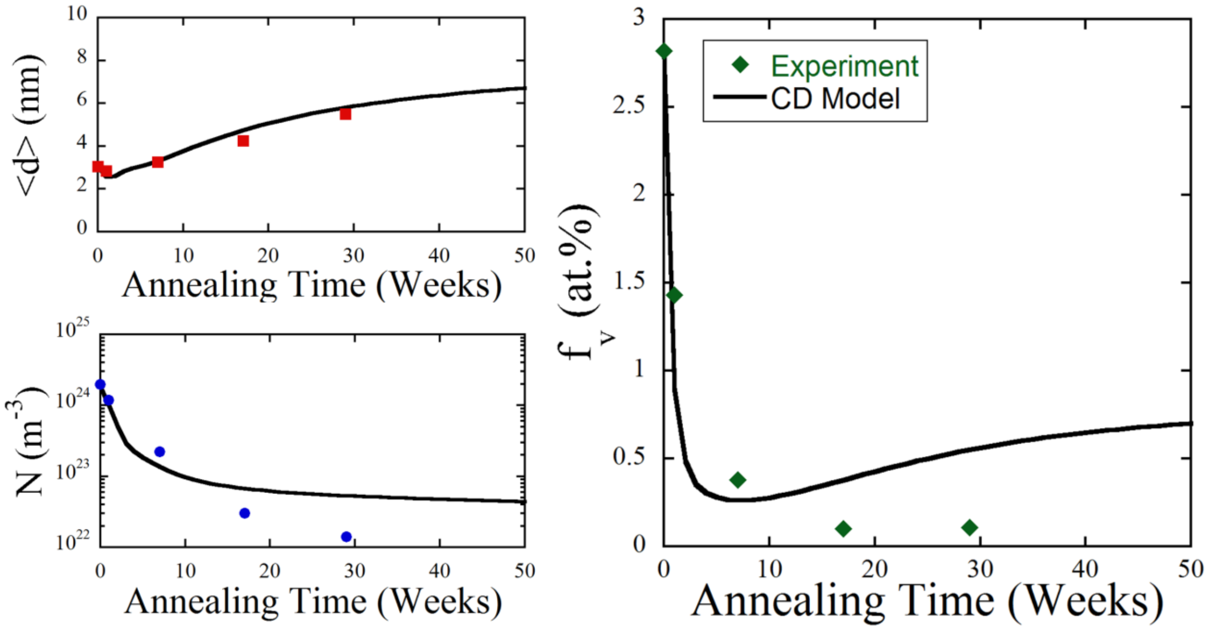

Figure 3.4. Precipitate <d> (nm), N (m-3) and f (at.%) after annealing from APT (points) and CD predictions (lines) for the high Ni steel (CM6).

It is useful to compare the MNSP compositions to the closest known Mn-Ni-Si intermetallic phases as shown in Table 3. This comparison suggests that the Γ_2 phase is closest to the composition in the AI condition, but the MNSPs are somewhat poor in Si. Annealing for intermediate times lowers the Si further, perhaps because it has the lowest chemical potential difference in the MNSPs relative to the matrix and also diffuses faster. At the longest t_a, the Mn fraction increases and Ni decreases, which may mark an incomplete transition between the Γ_2 and T_7 phases, e.g., Mn_2Ni_3Si partially transforming to Mn_3Ni_2Si; or, as is discussed below, the potential formation of a Mn enriched shell around the clusters.

Table 3.3 Relative amount of Mn, Ni and Si in the precipitates and compared with known Mn-Ni-Si phases.

t_a (wk)	Mn/Ni/Si*	Closest Phase
0	0.35/0.53/0.12	Γ_2:Mn_2Ni_3Si
1	0.36/0.54/0.10	Γ_2:0.33/0.5/0.17
7	0.38/0.54/0.08	Γ_2:0.33/0.5/0.17
17	0.39/0.54/0.07	Γ_2:0.33/0.5/0.17
29	0.41/0.42/0.17	Γ_2 -> T_7

It has previously shown that tip-to-tip variability can be exploited to assess the effects of local compositional variations on precipitation [6]. For example, while MNSPs were still found in all the tips from the high Ni steel (CM6) in the AI, 1 week and 7 week t_a, they were only found in tips containing more than ≈ 1.6%Ni and 1.4%Mn (close to the nominal alloy composition) for longer t_a. Thus only tips that contained clusters were included in plots of size distributions and N.

Finally, C and Mo are co-segregated to the MNSPs following the 29 week anneal at solute concentrations of ≈ 3 at.% and 5 at%, respectively. Other studies have shown these elements are depleted in the MNSPs in the AI condition [7, 24, 28], but previous higher temperature (> 400°C) aging studies of duplex stainless steels have shown a G phase precipitate association with Mo [29–31] and C [32] . Though these precipitate are not thought to be G-phase, there is no data on the literature on the Γ_2 phase in ferrite. It is unclear whether the lack of Mo and C association with the Mn-Ni-Si precipitates in the AI condition is caused by the irradiation itself, or the fact that it was performed at a much lower temperature (≈ 310°C) than the annealing studies (425°C).

APT data on the 29 week annealed high-Ni sample showed a significant reduction in the number density of the MNSPs. In addition, a number of tips did not contain any remaining precipitates, though these were in regions with lower dissolved Ni and Mn contents. Thus, EDS characterization on an FEI TALOS F200x S/TEM in the LMBDA facility at ORNL was carried out on the 57 week PIA condition to significantly increase the sampling volume. The EDS results are qualitatively very consistent with the 29 week APT data in that there were large regions with no precipitates and some regions with precipitates still remaining. In addition, one grain was found to contain very large Mn-Ni precipitates on the order of 20-30 nm long, but these did not appear to be significantly enriched in Si. An example of regions with smaller Mn-Ni-Si precipitates and the large Mn-Ni precipitates is shown in Figure 3.5. The main conclusion of the TALOS EDS results is that the precipitates remain stable at very long annealing times, even up to ≈ 8 times the t_a required for full dissolution of the MNSPs in the lower Ni alloy. In addition, one region contained much larger Mn-Ni enriched precipitates than ever observed in an irradiated RPV steel. Note that the EDS maps do not show significant Si enrichment to these large precipitates. It is unclear why this only occurred in a single grain, though it may be it had a much higher local concentration of Mn and/or Ni.

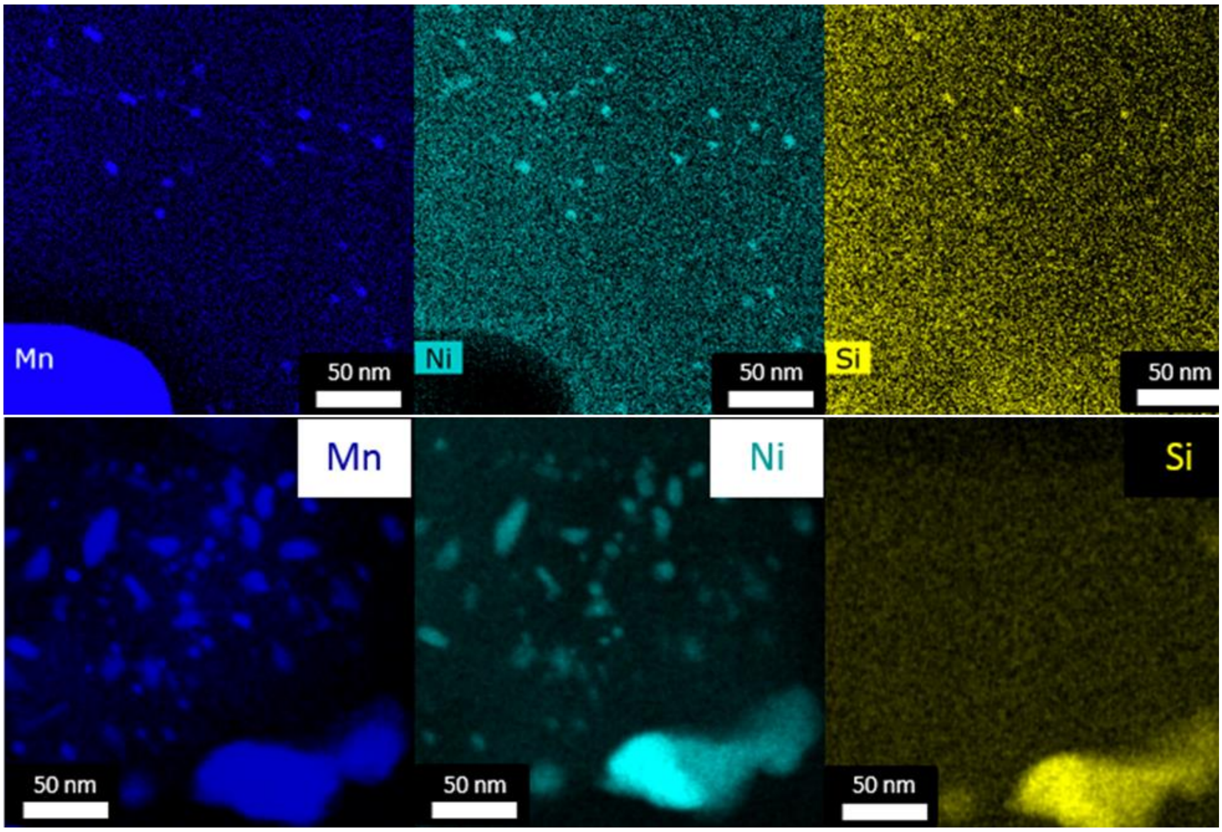

Figure 3.5. EDS maps showing Mn-Ni-Si precipitates remaining in the high Ni steel after annealing for 57 weeks at 425°C.

3.4.2 Cluster Dynamics Modeling

As shown above, the CALPHAD model correctly predicts complete dissolution of MNSPs in the medium Ni steel (LG), observed at 7 weeks of PIA at 425°C. On the other hand, the high Ni steel (CM6) is predicted to have an equilibrium MNSP f of ≈ 1.4%. This is significantly higher than the measured f_v at 29 weeks of 0.11%. A cluster dynamics (CD) model was used to predict MNSP evolution in the high Ni steel (CM6) at 425°C assuming a bulk composition of 1.63%Ni, 1.38%Mn and 0.34%Si which was close to the local compositions found in the tips containing MNSPs at 17 and 29 weeks. The other input to the PIA model was the AI MNSP size distribution, γ and D. Note, γ was fit to the MNSP evolution in a series of irradiated steels and was not altered to better fit the annealing data here [27]. That is, the PIA model has no independently adjusted fit parameters. The predicted f as a function of t_a in Figure 3.4 are in very good agreement with the experimental results, except that the CD model predicts an increase in f at longer annealing times, while those conditions observed with APT do not. While the <d> is very accurately predicted by the CD model, the number of stable precipitates is overestimated, which results in the overestimation of f. The main important conclusion of this model is that precipitates can dissolve even if the bulk phase is stable due to the Gibbs-Thomson effect, where driving force for growth of the precipitates cannot overcome the large effect of the interfacial energy at very small sizes. In this case, the precipitates were nucleated at the much lower $T_{irr} \approx 310°C$, where the r* was much smaller. At the higher $T_a = 425°C$ and the very solute depleted matrix, r* is expected to be much larger.

The size distributions for all t_a in Figure 3.6 show a decrease in the N for all MNSP sizes except for those with $r > 2.25$ nm. Note that no clusters with $r < 2.25$ nm were found in the 29 week annealed condition. The largest MNSP in the AI condition was r = 2.3 nm, while the 3 precipitates found after the 29 week PIA all had $r > 2.6$ nm. While this may seem to be a small difference, the number of atoms in a cluster scales with r^3. Thus the largest MNSP in the AI condition had ≈ 4500 Mn+Ni+Si atoms, while the 3 clusters found after the 29 week PIA contained 6500, 7200 and 8100 MNS atoms, respectively. The precipitates with $r > 2.25$ nm are not only stable at this long annealing time, but appear to be growing, confirming the hypothesis that the MNSPs in irradiated RPVs are equilibrium phases.

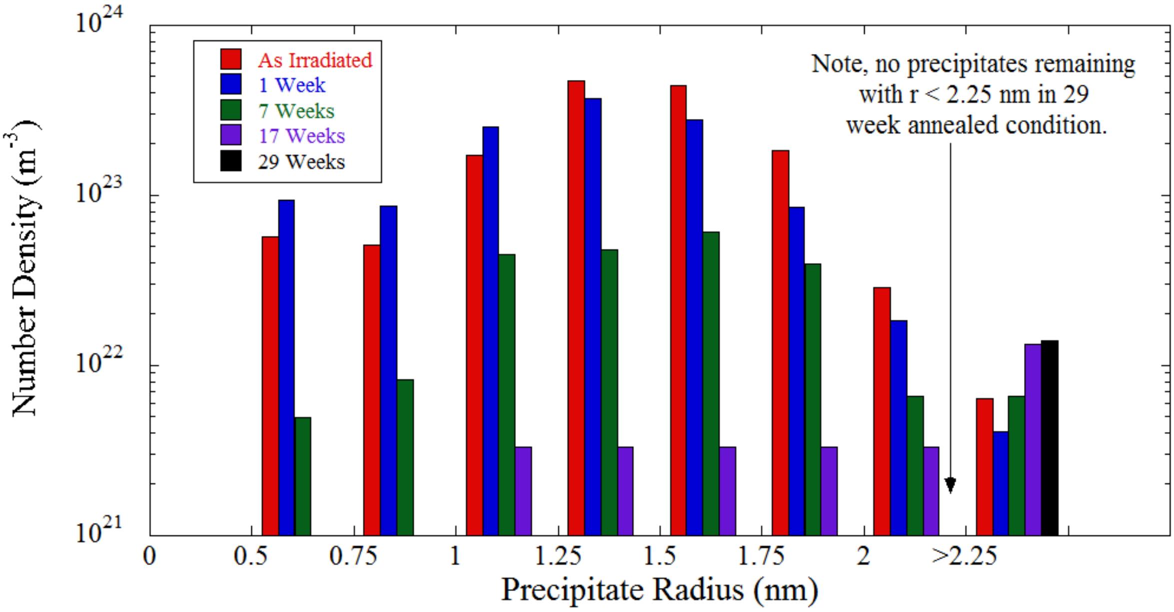

Figure 3.6. Size distribution of precipitates in the high Ni steel (CM6) for the AI and annealed conditions.

3.5 Discussion

The full dissolution in the medium Ni steel (LG) at 7 weeks suggests that at a 57-week t_a kinetics alone is sufficient to dissolve the MNSPs in the high Ni steel (CM6) if they are truly non-equilibrium solute clusters. The combination of APT results and CD model suggests that the significant reduction in the precipitate N is consistent with the nano-scale size of the MNSPs, which are predominantly below the critical radius (r_c) at 425°C in the initially solute depleted AI matrix. The critical radius is $r_c = 2\gamma/\Delta G_v$ where the free energy is the difference between the instantaneous concentration of dissolved solutes versus those in the MNSP. As the small MNSPs dissolve, the corresponding increase in the matrix solute concentration is sufficient to stabilize the larger precipitates. The fact that MNSPs with $r > 2.3$ nm are stable in a matrix that is only slightly solute depleted (≈ -0.11%) compared to the total in the AI condition, suggests that they are not induced by radiation, consistent with thermodynamic predictions. While the CD models over predict the number of stable precipitates that should remain, this PIA data can be used to fine tune both precipitation and annealing models. PIA at lower temperatures is ongoing to further investigate the r_c at different temperatures.

3.6 Conclusions

Post irradiation annealing (PIA) was used to investigate the formation mechanism of Mn-Ni-Si precipitates (MNSPs) in neutron irradiated RPV steels. The annealing, conducted at 425°C for long times, resulted in complete dissolution of MNSPs in medium Ni (0.74%) steel after only 7 weeks. In contrast, some MNSPs still remained at the longest annealing time of 57 weeks in the high Ni steel. APT showed that the local regions with the highest precipitate stability contained at least 1.6% Ni and 1.4% Mn, although even in these regions a significant reduction in N and f were observed. The significant reduction in N and f was rationalized by CD model, which accurately predicts the evolution of <d>, though overestimates N and correspondingly f. The reduction in N in the CD model is caused by the large r* at 425°C and the initially solute depleted matrix. As the precipitates dissolve and enrich the matrix, r* is decreased enough to stabilize the remaining larger precipitates. Over time, the model then predicts that these precipitates will continue growing in both <d> and f until an equilibrium f is reached. Finally, EDS results at 57 weeks showed one grain with mostly Mn-Ni precipitates up to 30 nm in length, suggesting that this region had a much higher Mn and/or Ni concentration than the rest of the analyzed liftout.

The number density of clusters with radius greater than 2.25 nm does not decrease significantly in any PIA conditions, but all clusters below that size dissolve after long times. The size distributions of precipitates in the various conditions show that the critical radius at 425°C and at the high Ni content is likely around 2.25 nm. The Mn-Ni-Si atoms per MNSP in the three found at 29 weeks is almost 50% higher than the largest cluster found in the AI condition, which is an indication of modest coarsening. In summary, long term PIA of precipitates shows stable, growing precipitates that have compositions in the core of the precipitates very close to the G2 phase that are predicted to form by CALPHAD. Thus, it is highly unlikely that the Mn-Ni-Si features formed at ≈ 105°C below the PIA temperature non-equilibrium solute clusters induced by radiation.

3.7 References

1. Odette GR and Nanstad RK. "Predictive reactor pressure vessel steel irradiation embrittlement models: Issues and opportunities", JOM 2009;61(7):17–23.
2. Eason ED, Odette GR, Nanstad RK and Yamamoto T. "A physically based correlation of irradiation-induced transition temperature shifts for RPV steels," Oak Ridge National Lab, 2007; ORNL/TM-2006/530.
3. Eason ED, Odette GR, Nanstad RK and Yamamoto T. "A physically-based correlation of irradiation-induced transition temperature shifts for RPV steels", J. Nucl. Mater. 2013;433:240–254.
4. Odette GR. "On the dominant mechanism of irradiation embrittlement of reactor pressure vessel steels", Scr. Metall. 1983;17(10):1183–1188.
5. Odette GR. "Radiation Induced Microstructural Evolution in Reactor Pressure Vessel Steels", Mater. Res. Soc. Symp. Proc. 1995;373:137–148.
6. Wells PB, Yamamoto T, Miller B, Milot T, et al. "Evolution of manganese–nickel–silicon-dominated phases in highly irradiated reactor pressure vessel steels", Acta Mater. 2014;80:205–219.
7. Miller MK, Powers KA, Nanstad RK and Efsing P. "Atom probe tomography characterizations of high nickel, low copper surveillance RPV welds irradiated to high fluences", J. Nucl. Mater. 2013;437(1–3):107–115.
8. Edmondson PD, Miller MK, Powers KA and Nanstad RK. "Atom probe tomography characterization of neutron irradiated surveillance samples from the R . E . Ginna reactor pressure vessel", J. Nucl. Mater. 2016;470:147–154.
9. Styman PD, Hyde JM, Parfitt D, Wilford K, et al. "Post-irradiation annealing of Ni–Mn–Si-enriched clusters in a neutron-irradiated RPV steel weld using Atom Probe Tomography", J. Nucl. Mater. 2015;459:127–134.
10. Styman PD, Hyde JM, Wilford K, Morley a., et al. "Precipitation in long term thermally aged high copper, high nickel model RPV steel welds", Prog. Nucl. Energy 2012;57:86–92.
11. Ngayam-Happy R, Becquart CS, Domain C and Malerba L. "Formation and evolution of MnNi clusters in neutron irradiated dilute Fe alloys modelled by a first principle-based AKMC method", J. Nucl. Mater. 2012;426(1–3):198–207.
12. Ngayam-Happy R, Becquart CS and Domain C. "First principle-based AKMC modelling of the formation and medium-term evolution of point defect and solute-rich clusters in a neutron irradiated complex Fe-CuMnNiSiP alloy representative of reactor pressure vessel steels", J. Nucl. Mater. 2013;440(1–3):143–152.
13. Bonny G, Terentyev D, Bakaev a., Zhurkin EE, et al. "On the thermal stability of late blooming phases in reactor pressure vessel steels: An atomistic study", J. Nucl. Mater. 2013;442(1–3):282–291.

14. Bonny G, Terentyev D, Zhurkin EE and Malerba L. "Monte Carlo study of decorated dislocation loops in FeNiMnCu model alloys", J. Nucl. Mater. 2014;452(1–3):486–492.

15. Xiong W, Ke H, Wells PB, Barnard L, et al. "Thermodynamic models of low temperature Mn-Ni-Si precipitation in reactor pressure vessel steels", MRS Commun. 2014;4(3):101–105.

16. Sprouster DJ, Sinsheimer J, Dooryhee E, Ghose SK, et al. "Structural Characterization of Nanoscale Intermetallic Precipitates in Highly Neutron Irradiated Reactor Pressure Vessel Steels", Scr. Mater. 2016;113:18–22.

17. Miller MK, Chernobaeva AA, Shtrombakh YI, Russell KF, et al. "Evolution of the nanostructure of VVER-1000 RPV materials under neutron irradiation and post irradiation annealing", J. Nucl. Mater. 2009;385(3):615–622.

18. Meslin E, Radiguet B, Pareige P, Toffolon C, et al. "Irradiation-Induced Solute Clustering in a Low Nickel FeMnNi Ferritic Alloy", Exp. Mech. 2011;51(9):1453–1458.

19. Nielsen JW. "As-Run Physics Analysis for the UCSB-1 Experiment in the Advanced Test Reactor," 2015; INL/EXT-15-34225.

20. Odette GR and Lucas GE. "Recent Progress in Understanding Reactor Pressure Vessel Steel Embrittlement", Radiat. Eff. Defects Solids 1998;144(1–4):189–231.

21. Odette GR and Wirth BD. "A computational microscopy study of nanostructural evolution in irradiated pressure vessel steels", J. Nucl. Mater. 1997;251:157–171.

22. Odette GR, Yamamoto T and Klingensmith D. "On the effect of dose rate on irradiation hardening of RPV steels", Philos. Mag. 2005;85(4–7):779–797.

23. Stephenson LT, Moody MP, Liddicoat P V. and Ringer SP. "New techniques for the analysis of fine-scaled clustering phenomena within atom probe tomography (APT) data.", Microsc. Microanal. 2007;13(6):448–463.

24. Miller MK and Russell KF. "Embrittlement of RPV steels: An atom probe tomography perspective", J. Nucl. Mater. 2007;371(1–3):145–160.

25. Marquis EA and Hyde JM. "Applications of atom-probe tomography to the characterisation of solute behaviours", Mater. Sci. Eng. R Reports 2010;69(4–5):37–62.

26. Cunningham NJ. "Study of the Structure, Composition, and Stability of Y-Ti-O nm-Scale Features" [PhD Thesis]. University of California, Santa Barbara, 2012.

27. Ke H, Wells PB, Barnard L, Odette GR, et al. "Cluster dynamics modeling of Mn-Ni-Si precipitates in low-Cu reactor pressure vessel steels", In Prep.

28. Miller MK, Russell KF, Sokolov MA and Nanstad RK. "APT characterization of irradiated high nickel RPV steels", J. Nucl. Mater. 2007;361:248–261.

29. Li S, Wang Y, Wang X and Xue F. "G-phase precipitation in duplex stainless steels after long-term thermal aging: A high-resolution transmission electron microscopy study", J. Nucl. Mater. 2014;452(1–3):382–388.

30. Mateo A, Llanes L, Anglada M, Redjaimia A, et al. "Characterization of the intermetallic G-phase in an AISI 329 duplex stainless steel", J. Mater. Sci. 1997;32(17):4533–4540.

31. Danoix F and Auger P. "Atom probe studies of the Fe-Cr system and stainless steels aged at intermediate temperature: a review", Mater. Charact. 2000;44(1–2):177–201.

32. Chung HM and Chopra OK. "Characterization of Advanced Materials", In: Characterization of Advanced Materials. 1. Springer US, 1991. p. 123–147.

4. MECHANICAL PROPERTY MEASUREMENTS ON NEW IRRADIATED ALLOYS

4.1 Introduction

UCSB ATR-2 fills a critical gap in embrittlement data and understanding, especially since current models systematically underpredict TTS at high fluence [1-2]. This report will focus on mechanical testing (tensile tests) of a small subset of the extensive matrix of new alloys and irradiation conditions in UCSB ATR-2 experiment. A particular focus is a class of very high 3.5% Ni steels, which is nearly 5 times more than in most US RPV steels. These steels have excellent unirradiated strength and toughness properties, along with a very low transition temperature. Irradiation hardening increases synergistically with Cu, Ni and Mn and at high fluence MNSP LBPs make a major contribution to embrittlement. Limited data suggests that high levels of embrittlement can be avoided if Mn content in the steels is lowered, although the reason for this has not been well understood. While Mn is a traditional alloying element, in part to getter Sulfur, it is possible to reduce its concentrations in so-called super clean steels with low impurity contents. The high Ni matrix and corresponding sponsored PIE, is aimed at testing the high-Ni low -Mn hypothesis, or "Mn starvation", and to develop a better general understanding of the role of Mn (and Si) in steels with a very wide range of Ni contents up to 3.5%.

4.2 Materials and Methods

Tensile tests were performed on a series of RPV model steels from ATR-2. This matrix contains superclean steels with a very wide range of solute contents in order to determine the effect of various solutes on hardening and precipitation. The alloys were irradiated to a peak fluence of $\Phi t \approx 13 \times 10^{19}$ n/cm^2 at 290C with varying Mn and Ni with single C and P variants. All alloys have ≈ ≈ 0.06wt%Cu and ≈ 0.2wt% Si. Figure 1 shows the expanded Ni and Mn solute contents of ATR-2 alloys versus those from previous UCSB test reactor experiments.

4.3 Results

Figure 2a shows the hardening after irradiation as a function of bulk alloy Ni content at two different bulk Mn contents. Figure 2b shows the hardening plotted as a function of bulk Mn content. The results show that embrittlement increases with increasing Ni content of typical RPV alloys. At high Mn (1.5%), the irradiation induced hardening increases linearly with increasing bulk Ni content (black diamonds). This same trend is seen at low Mn (0.25%) when increasing bulk Ni from 0.4 to 1.6%, but there is not a significant increase in $\Delta\sigma_y$ when going from 1.6 to 3.5% Ni. This lack of additional hardening with increasing Ni at low Mn is thought to be caused by so-called "Mn starvation." Normal phase selection requires 1 Mn + Si for every 1 precipitated Ni. Thus, at such a high Ni content of 3.5 wt.%, Ni cannot fully precipitate at such a low Mn content of 0.25 wt.%.

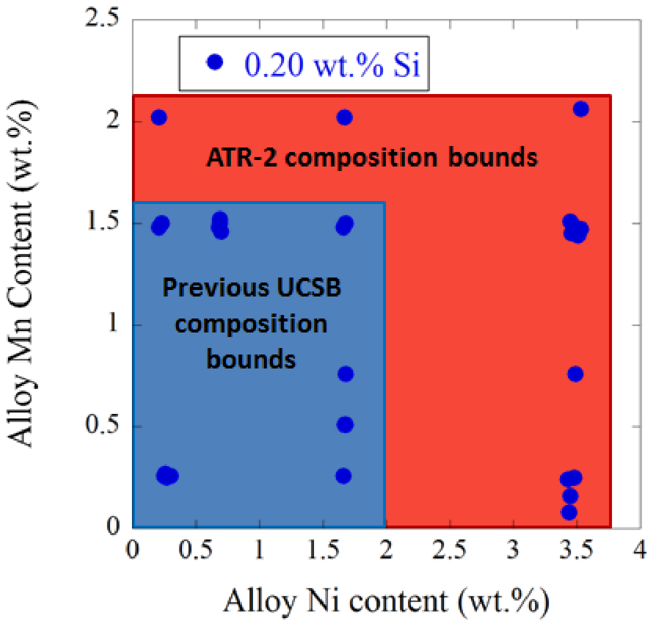

Figure 4.1. Ni and Mn bulk solute contents of expanded compositional range (red box) of ATR-2 versus previous UCSB test reactor experiments (blue box). Blue dots indicate specific alloy compositions.

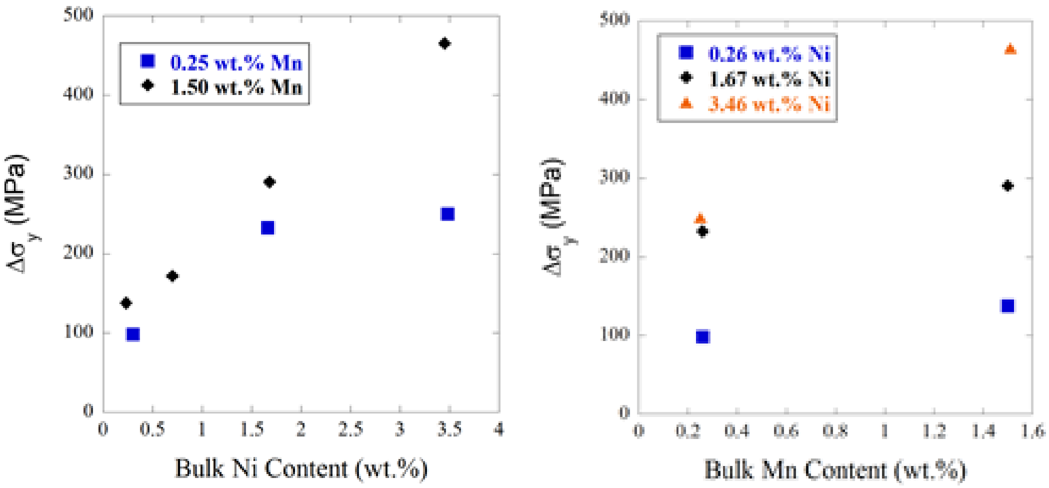

Figure 4.2. Ni and Mn bulk solute contents of expanded compositional range (red box) of ATR-2 versus previous UCSB test reactor experiments (blue box). Blue dots indicate specific alloy compositions.

4.4 Conclusions

Initial tensile testing was used to investigate the effect of Mn starvation on hardening and embrittlement in neutron irradiated RPV steels. The irradiation hardening within this new matrix of RPV alloys increased synergistically with both Ni and Mn bulk solute content. These preliminary $\Delta\sigma_y$ results provide a preview of a much large matrix of alloy compositions neutron irradiated in the UCSB ATR-2 experiment. Further mechanical testing will be performed at UCSB using hardness testing and shear punch testing. Ongoing microstructural work will characterize the precipitates in the rest of the samples and correlate the precipitation in each alloy with the measured yields stress increases. A particular focus will be on the effect of compositional variations on precipitate volume fraction, size, number density and composition.

4.5 References

1. Odette GR and Nanstad RK. "Predictive reactor pressure vessel steel irradiation embrittlement models: Issues and opportunities", JOM 2009;61(7):17–23.
2. Eason ED, Odette GR, Nanstad RK and Yamamoto T. "A physically based correlation of irradiation-induced transition temperature shifts for RPV steels," Oak Ridge National Lab, 2007; ORNL/TM-2006/530.

5. AVRAMI MODELLING

5.1 Introduction

The data presented in the previous reports demonstrates that reliable embrittlement prediction models of RPV ΔT at extended lifetimes must include the effects of MNSPs. While the creation of a new model will ultimately require the fitting of the large surveillance ΔT database, as well as likely data from the UCSB ATR-2 experiment, the framework for a potential model is proposed here. First, it is shown that the measured hardening after irradiation can be directly correlated to the precipitate f_v. Next a simple Avrami type model is used to predict $f_v(\phi t_e)$. The parameters in the Avrami model were determined through fitting the large f_v database generated by researchers at UCSB.

Since $\Delta\sigma_y$ can be determined from f_v, the $f_v(\phi t_e)$ Avrami model is then converted to $\Delta\sigma_y(\phi t_e)$. The $\Delta\sigma_y$ predictions are then compared with actual measured mechanical property measurements to show very good agreement with the large UCSB test reactor database. To further evaluate the accuracy of this proposed model, the $\Delta\sigma_y$ predictions are compared with the first set of available tensile samples from the UCSB ATR-2 irradiation. The model again shows good agreement, which is of particular importance because no microstructure data from the ATR-2 experiment was used to determine the best fit parameters. Finally, a conversion factor is used to translate $\Delta\sigma_y(\phi t_e)$ to $\Delta T(\phi t_e)$, which is used to compare the Avrami model with two current models used to predict RPV embrittlement. The residuals for the Avrami type model are shown to be on the same order as the models statistically fit to large mechanical property databases. While the final model will require fitting to actual mechanical property databases, the general framework proposed here shows great promise in predicting extended life ΔT.

5.2 Microstructure to Property Correlation

In order to create a physically informed model predicting $\Delta T(\phi t_e)$, a correlation must first be developed between the microstructure changes that occur under irradiation and the resultant mechanical property changes. The EONY model contains two microstructure features, matrix defects and Cu-rich precipitates. A first order model will attempt to correlate only the precipitates with $\Delta\sigma_y$.

The principle of superposition is used to determine the total σ_y from the combination of the various hardening features in an alloy. Here, the normalized MNSP hardening efficiency ($\sigma_{yp}/\sqrt{f_v}$) was determined through calibrating a modified Russell-Brown type model to a series of irradiated low Cu steels where both microstructure and mechanical property data were available. In addition, the Cu-bearing steels from the ATR1 condition, which contain significant f_v of MNSPs were also included in the fit, shown in Figure 5.1. A peak hardening of $\approx$ 5700 MPa/$\sqrt{f_v}$ occurs for $\langle r \rangle \approx 1.2$ nm. This shows fairly good agreement with a previous fit of hardening efficiency for CRPs [1], which found a peak hardening of ≈ 4800 MPa/$\sqrt{f_v}$. The comparison is even closer when considering that the model in that case subtracted off a set amount of hardening for what were considered to be matrix features, which is the reason for the reduction of CRP hardening efficiency when compared to the fit here.

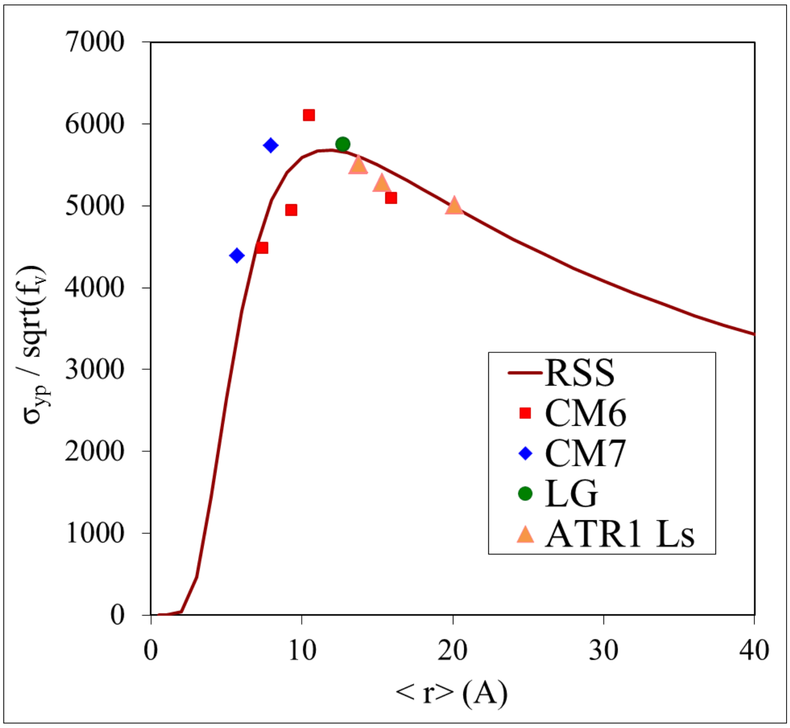

Figure 5.1. Modified Russell-Brown fit to determine the precipitate hardening efficiency.

The large microstructure and mechanical property database collected by researchers at UCSB can be used to test the accuracy of this model. The hardening efficiency ($\sigma_{yp}/\sqrt{f_v}$) was determined for the measured <r> and then multiplied by $\sqrt{f_v}$ to determine σ_{yp}. Superposition was then used to combine σ_{yp} with the strength contributions of existing features predict $\Delta\sigma_y$ for a given alloy/condition. Mechanical property changes for a given condition were measured using either tensile tests to measure $\Delta\sigma_y$ (MPa) or hardness testing converted to $\Delta\sigma_y$ from the correlation $\Delta\sigma_y = 3.3*\Delta H$ [2].

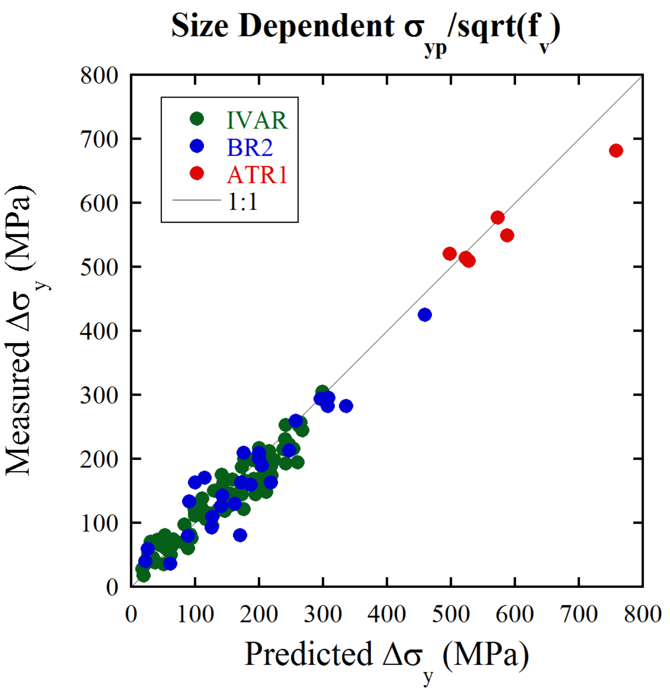

Figure 5.2. Measured vs predicted $\Delta\sigma_y$ where the predictions were made from a size dependent precipitate hardening efficiency.

Figure 5.2 shows that the agreement between the predicted and measured $\Delta\sigma_y$ is excellent. It should be noted that the calibration of the hardening efficiency, $\sigma_{yp}/\sqrt{f_v}$, was performed using only a handful of conditions, but it appears to be very accurate for all the alloy/conditions studied. Since the total $\Delta\sigma_y$ seems to be reliably predicted from the precipitate data, further analysis will assume they are the only hardening feature, or at least that any other features present cause a negligible increase to the total hardening.

The motivation behind calibrating the precipitate hardening efficiency is ultimately to model $f_v(\phi t_e)$ and convert it to $\Delta\sigma_y(\phi t_e)$. As was shown in Figure 5.1, the precipitate hardening efficiency is affected by <r>. Unfortunately, accurately predicting $\langle r\rangle(\phi t_e)$ is much more difficult than predicting $f_v(\phi t_e)$, especially when considering that the effect of ϕ on <r> is not well understood. The precipitates that form over the ϕt_e relative to reactor lifetimes have typically been shown to be on the order of <r> ≈ 1-2 nm, which have a relatively narrow $\sigma_{yp}/\sqrt{f_v}$ of ≈ 5300 MPa from Figure 5.2. Instead of using a size dependent $\sigma_{yp}/\sqrt{(f_v)}$, the prediction shown in Figure 5.3 uses a constant = 5300 MPa for $\sigma_{yp}/\sqrt{(f_v)}$. In this case, the overall agreement does not significantly change. Thus, if $f_v(\phi t_e)$ can be accurately predicted, then $\Delta\sigma_y(\phi t_e)$ should also be reasonably well predicted.

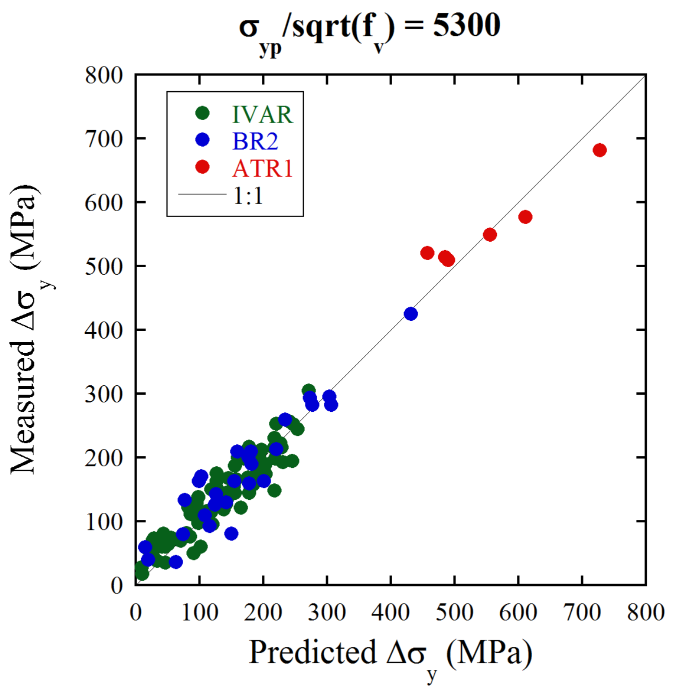

Figure 5.3. Measured vs predicted Δσy where the predictions were made using σyp/√(fv) = 5300 MPa.

5.3 *Volume Fraction Prediction*

5.3.1 *Effective Fluence*

Increasing ϕ delays precipitation to a higher ϕt. Thus, f_v predictions must be made for a specific reference flux, ϕ_r and compared to data either taken at or scaled to the same ϕ_r. Here, an effective fluence, ϕt_e, is defined for each condition to compare data taken across a range of ϕ using

$$\phi t_e = \phi t \left(\frac{\phi_r}{\phi}\right)^p \tag{5.1}$$

where ϕ and ϕt are the actual flux and fluence for the condition, ϕ_r is a defined reference flux and p is a scaling parameter that varies with ϕ. Here, ϕ_r was selected to match that of the lowest ϕ IVAR condition, $\phi_r = 3\text{x}10^{11}$ n/cm^2-s. The best fit p was determined for the 6 core alloys (LC, LD, LG, LH, LI, CM6) and all showed p to vary between 0.25 and 0.3. Here p = 0.25 was used. Future work will focus on using the high ϕt, medium ϕ UCSB ATR-2 experiment to further refine p.

5.3.2 *Avrami Model*

Since $\Delta\sigma_y$ can be predicted from a given f_v, a model predicting $f_v(\phi t_e)$ must be developed to ultimately predict $\Delta\sigma_y(\phi t_e)$. Previous studies have shown that the precipitate f_v can be modelled with an Avrami equation [1, 3, 4], a type of which is given by

$$f(\phi t_e) = f_{max}\left\{1 - \exp\left[-\left(\frac{\phi t_e}{\phi t_0}\right)^{\beta}\right]\right\} \qquad (5.2)$$

where f_{max} is the saturation f_v, ϕt_e is the effective fluence, ϕt_0 is the fluence requires to reach 63% of f_{max} and β is a parameter that depends on the rate controlling precipitation kinetic mechanisms [1, 3, 4]. For example, $\beta = 3/2$ corresponds to the case of diffusion controlled growth, where the growth of the precipitate is limited by the diffusion rate of atoms across the precipitate/matrix interface. $\beta = 3$ corresponds to the case when the interface mobility is rate controlling [1]. $df/d\phi t_e$ is slow in the early stages of precipitates due to the difficult step of nucleation, increases during the growth stage and slows again at longer times when most of the solute has been depleted from the matrix. In Cu-bearing alloys, the CRPs grow to saturation much before MNSPs, so in these cases, a two part Avrami model, CRP and MNSP, is used. Each portion of the model uses three parameters, f_{max}, β and ϕt_0. It is difficult to fit all three parameters simultaneously because they are interrelated. For example, the ϕt_0 is higher if f_{max} is increased. In addition, β doesn't necessarily need to be included in the fits because it is dictated by the physics relating to the nucleation and growth processes, as was described above. Thus, to simplify the fitting procedure, $f_{max,CRP}$, $f_{max,MNSP}$, β_{CRP} and β_{MNSP} were fixed and only $\phi t_{0,CRP}$ and $\phi t_{0,MNSP}$ were varied to find the best fit to the microstructural database for the 6 alloys.

The selection of $f_{max,CRP}$ for each alloy was determined based on each individual alloy's bulk Cu and Ni contents. In this case, $f_{max,CRP}$ was typically set to be ≈ 0.05-0.20% greater than the amount of Cu in solution. The CRP saturation was set above the available bulk Cu because the CRPs become enriched in Mn and Ni over time, something that would happen whether MNSPs form or not, so the total CRP f_v may be larger than the available Cu. $f_{max,MNSP}$ was selected so that the total f_v (CRP+MNSP) at saturation was ≈ that found in the ATR1 condition. While the assumption that the ATR1 condition has reached saturation has not been conclusively proven, it appears to be a relatively reasonable assumption for a number of reasons. First, the LD sample appears to have begun coarsening by this high ϕt_e, which would occur only after saturation has been reached. Second, the LG sample, which contained ~ 0.1% fv in the G1 condition, has ≈ the same MNSP f_v as all the other medium Ni alloys in the ATR1 condition. Since it contained a much smaller volume fraction than the other alloys in the G1 condition, either the rate of precipitate formation was much faster in LG than in the other alloys, or more likely, it continued growing after the other alloys reached saturation.

Before performing the final fitting of ϕt0, β_{CRP} and β_{MNSP} were varied to qualitatively observe the best fit values and compare these with the expected theoretical values in each case. CRPs nucleate as BCC crystals before transforming to FCC at a larger size. Because the small CRPs have the same crystal structure as the Fe matrix, the interface movement is controlled by the diffusion of atoms across the interface. In addition, Thus, it is expected that in the case of CRPs, β = 3/2, corresponding to diffusion controlled 3D growth. In actuality, the best fit β for CRPs has previously been shown to be slightly different than the theoretical value with $\beta_{CRP} = 1.1$ [1]. Here, the best fit was found to be $\beta_{CRP} = 1$. For MNSPs, the best fit β was determined to be $\beta_{MNSP} = 2.5$. This corresponds to diffusion controlled growth of precipitates with a constant nucleation rate.

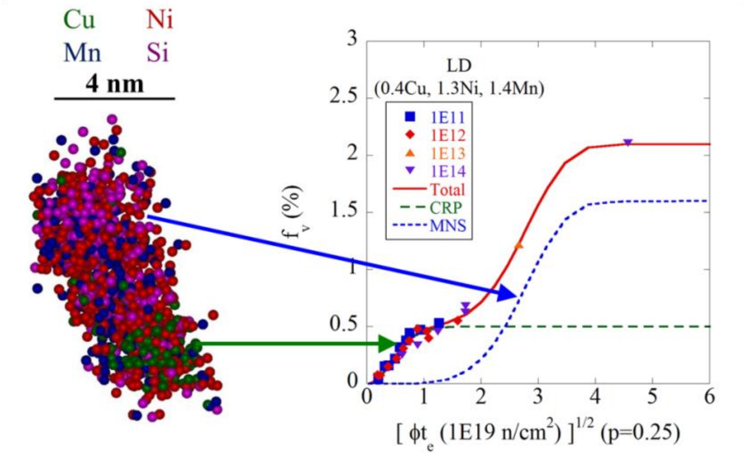

Figure 5.4. Illustration of a two part Avrami fit for high Cu steels, where the total fv is the sum of the CRP f_v and MNS f_v.

Thus, the only fit parameters were ϕt_0 for both portions, CRP and MSNP. These were least square fit to determine the best fit ϕt_0 by minimizing the error between the predicted and measured total f_v. An example of the two feature Avrami fit is shown in Figure 5.4. The final fits for all alloys can be seen in Figure 5.5.

Overall, the two feature Avrami model appears to capture the total measured f_v very well, as can be seen from Figure 5.6 which plots the measured vs Avrami predicted f_v for all alloy/conditions. The best fit parameters for the various Avrami models are shown in Table 5.1. The first thing to note is that the MNSP ϕt_0 is ≈ 5-30 times higher than that for the CRPs. This very slow evolution is MNSPs is the reason they were first called “Late Blooming Phases” over 20 years ago [5]. The MNSP ϕt_0 is slightly higher for the medium Ni steels, but there doesn’t appear to be a significant trend among the medium Ni steels with varying Cu. While a systematic trend would be expected based on the chemistry of the alloys, with higher Cu and Ni contents accelerating the formation of MNSPs, it should be stressed that there are very few high ϕt data points where significant quantities of MNSPs were observed. Thus, the limited data is expected to result in some uncertainty in the fitted ϕt_0.

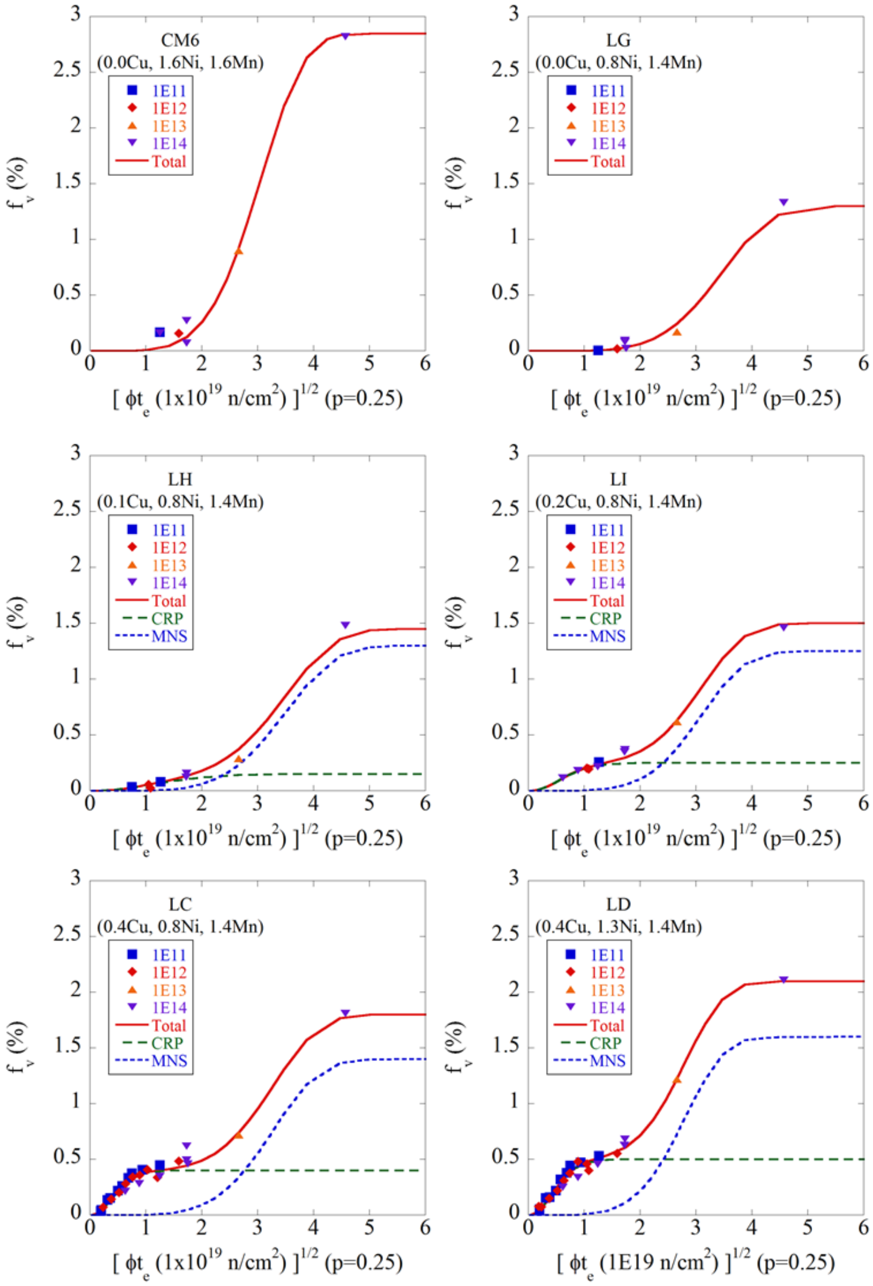

Figure 5.5. Avrami f_v fits for the 6 core alloys with conditions at different ϕ labelled in different colors. Note the units of ϕ are in n/cm^2-s.

Finally, no large conclusions should be drawn from the absolute values of ϕt_0, as they are largely affected by the choice of the p exponent when performing the ϕ correction. For example, varying p from 0.2 to 0.3 results in a shift of ϕt_0 for MNSPs in LG from 17.2x10^{19} n/cm2 to 10.0x10^{19} n/cm^2. This large shift is likely due to the fact that there is essentially no microstructure data available for the low ϕ conditions because MNSPs aren't seen until higher ϕt. Again, the ATR-2 experiment, which contains a large number of high ϕt conditions over a range of medium ϕt, will be very valuable in refining the best fit $\phi t_{0,MNSP}$.

Table 5.1. Summary of best fit Avrami parameters for CRPs and MNSPs with p=0.25.

Alloy	CRP Parameters			MNSP Parameters		
	β	f_{max} (%)	ϕt_0 ($1x10^{19}$ n/cm^2)	β	f_{max} (%)	ϕt_0 ($1x10^{19}$ n/cm^2)
CM6	-	-	-	2.5	2.85	10.2
LC	1	0.4	0.3	2.5	1.40	11.8
LD	1	0.5	0.4	2.5	1.60	8.6
LG	-	-	-	2.5	1.30	13.2
LH	1	0.15	2.4	2.5	1.30	13.5
LI	1	0.25	0.6	2.5	1.25	10.6

Table 5.2. Summary of best fit Avrami parameters for CRPs and MNSPs.

Alloy	CRP ϕt_0 ($1x10^{19}$ n/cm^2)			MNSP ϕt_0 ($1x10^{19}$ n/cm^2)		
	P=0.20	P=0.25	P=0.30	P=0.20	P=0.25	P=0.30
CM6	-	-	-	12.8	10.2	10.0
LC	0.3	0.3	0.3	14.9	11.8	9.2
LD	0.4	0.4	0.4	10.8	8.6	7.0
LG	-	-	-	17.2	13.2	10.0
LH	2.8	2.4	2.1	17.9	13.5	10.1
LI	0.8	0.6	0.5	13.1	10.6	8.6

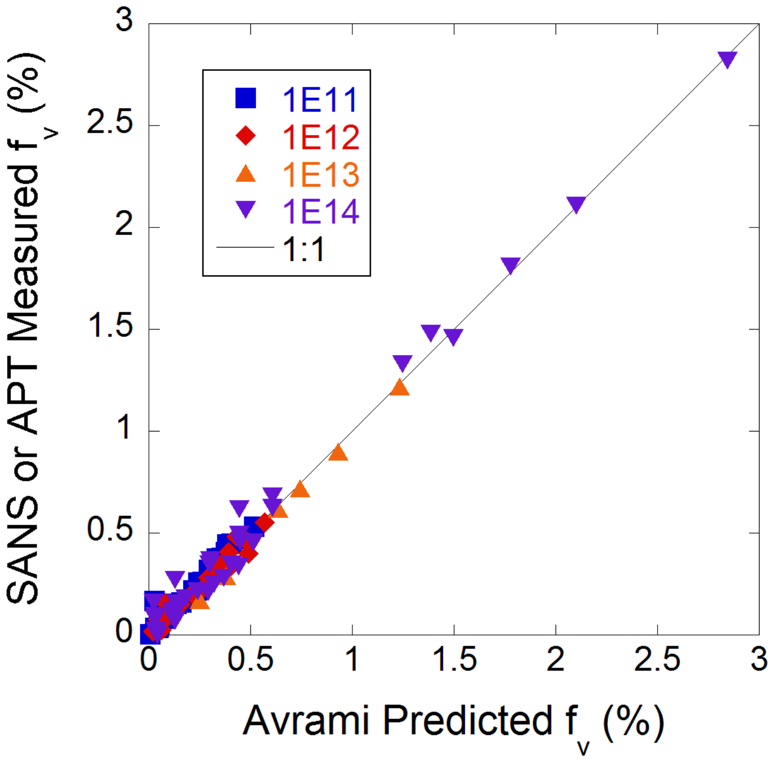

Figure 5.6. Measured vs predicted f_v from the Avrami model fits.

5.4 *Predicting Mechanical Properties from Microstructure*

The $f_v(\phi t_e)$ Avrami model can be converted to $\Delta\sigma_y(\phi t_e)$ simply by using the correlation established in section 5.2, which found $\Delta\sigma_{yp} = 5300\sqrt{f_v}$. Then, using the principle of superposition, $\Delta\sigma_y$ can be determined. This $\Delta\sigma_y(\phi t_e)$ is compared with actual mechanical property measurements for the large UCSB test reactor database, as is seen in Figure 5.7. There appears to be an under prediction at low fluence for most every alloy, though the overall magnitude of this under prediction is fairly small. Figure 5.8 shows the measured vs predicted $\Delta\sigma_y$ to more clearly view the accuracy of the model. Figure 5.9 shows the same data as in Figure 5.8, but at a different scale to better see the under prediction at lower $\Delta\sigma_y$.

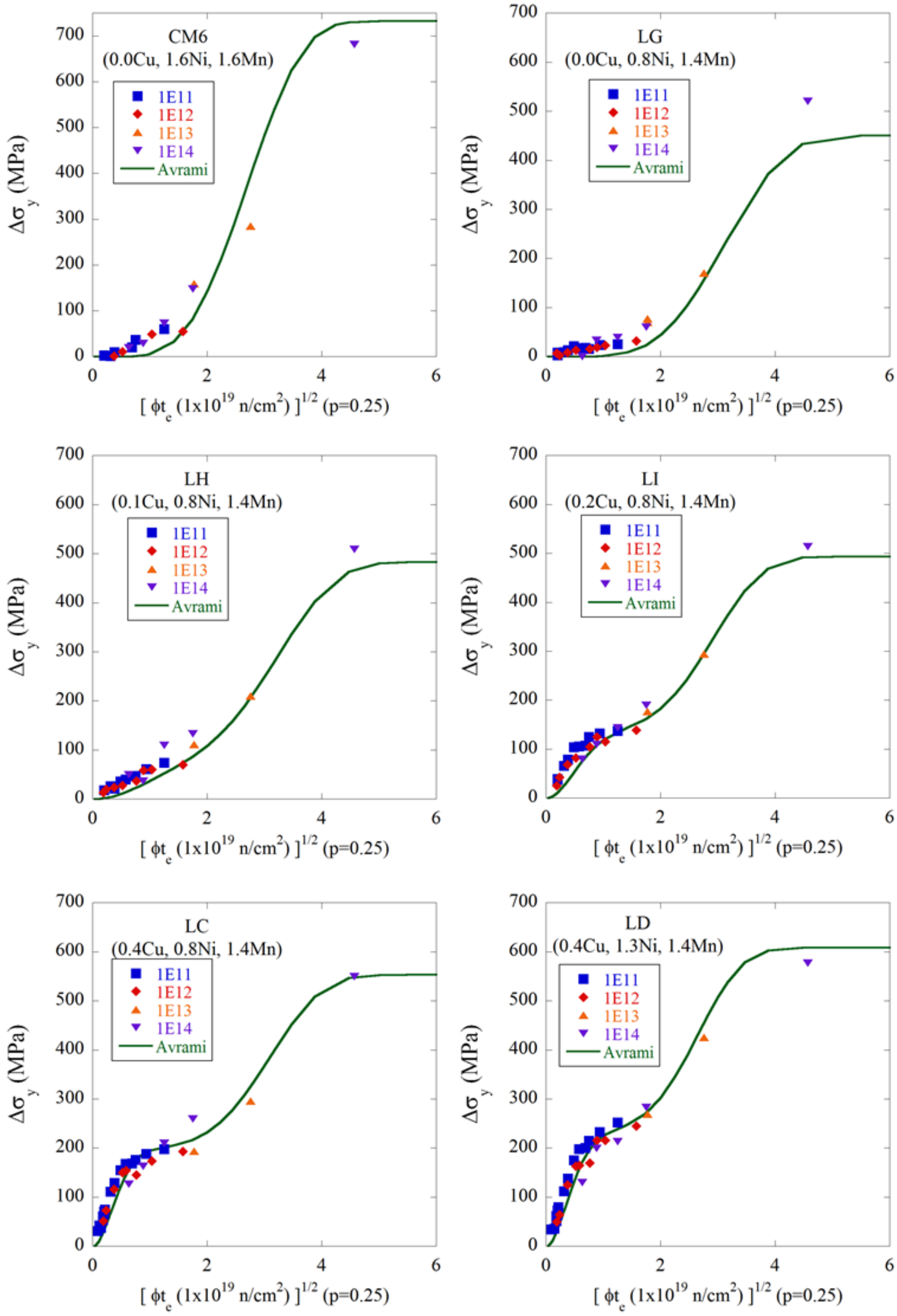

Figure 5.7. Avrami $\Delta\sigma_y(\phi t_e)$ model compared to the UCSB test reactor database with conditions at different ϕ labeled in different colors. Note the units of ϕ are in n/cm^2-s.

This under prediction is largely caused by the lower Cu steels, which have measurable hardening at low ϕt_e, but not much predicted hardening due to the slowly nucleating MNSPs. In addition, since $\Delta\sigma_y$ model was derived from fitting the available microstructure database, it may be that clusters are present that were unable to be detected by SANS. Thus, the microstructure model may not be as accurate in the case of the lower Cu steels since the early stages of clustering are difficult to detect in SANS. In any event, the low ϕt_e hardening is only under predicted by ≈ 25 MPa and the model shows very good agreement at higher ϕt_e.

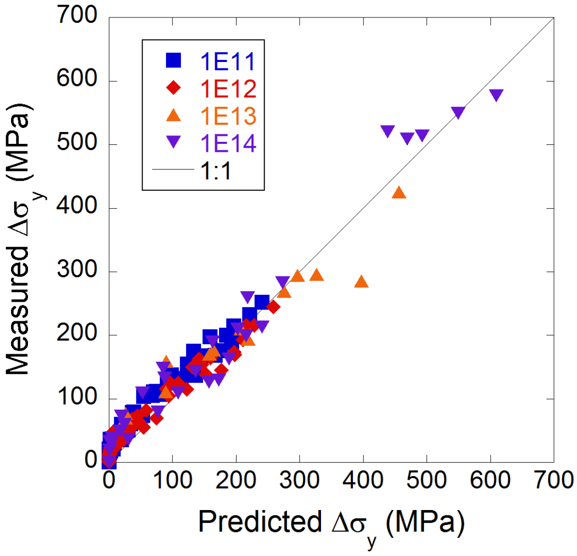

Figure 5.8. Measured vs Predicted $\Delta\sigma_y$ where the predictions are from the $\Delta\sigma_y(\phi t_e)$ Avrami model.

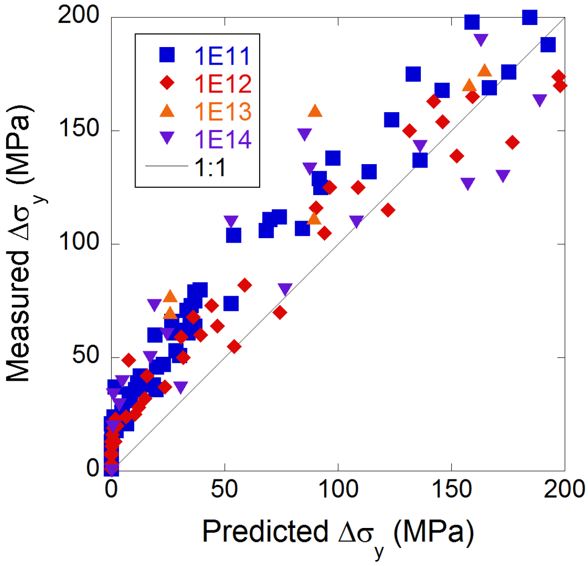

Figure 5.9. Higher magnification view of Figure 5.8 to more clearly seen the predictions at lower $\Delta\sigma_y$.

5.5 ATR2 Irradiation

The large scale UCSB ATR2 irradiation is designed to investigate RPV embrittlement at extended life fluences. The first batch of tensile specimens from this irradiation were recently received and tested at UCSB. The irradiation condition for the core 6 alloys is shown below. The ϕt_e is calculated using p = 0.25 and $\phi_r = 3x10^{11}$ n/cm^2-s.

Table 5.3. UCSB ATR-2 irradiation condition.

Condition	Neutron ϕ* (n/cm2/s)	Neutron ϕt* (n/cm2)	Neutron ϕte* (n/cm2)	Dose Rate (dpa/s)	Dose (dpa)	Tirr (°C)
ATR2	3.6E+12	1.2E+20	6.5E+19	5.4E-09	0.18	290

*For neutron energies > 1 MeV

Two examples of unirradiated and irradiated σ-ε curves for the Cu-free, high Ni steel (CM6) and high Cu/Ni steel (LD) are given in Figure 5.10 and Figure 5.11, respectively.

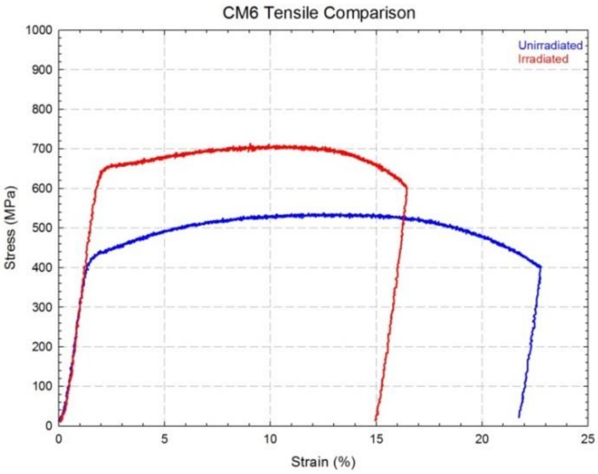

Figure 5.10. Unirradiated (blue) and irradiated (red) σ-ε curves for the Cu-free, high Ni steel (CM6) in the ATR-2 condition.

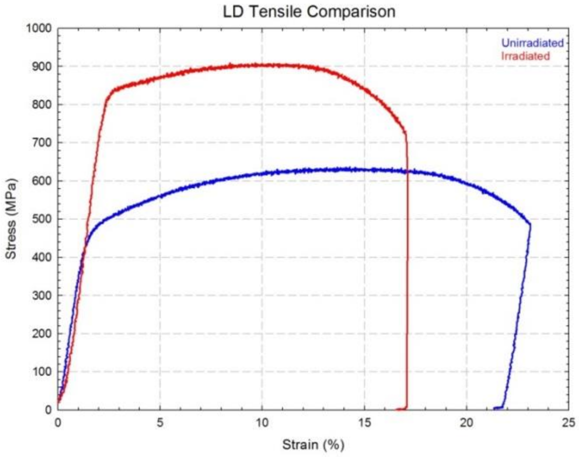

Figure 5.11. Unirradiated (blue) and irradiated (red) σ-ε curves for the high Cu/Ni steel (LD) in the ATR-2 condition.

Significant hardening has clearly occurred in both steels. The $\Delta\sigma_y(\phi t_e)$ model was used to predict the $\Delta\sigma_y$ for the steels in the ATR-2 condition, with the measured vs predicted $\Delta\sigma_y$ data shown in Figure 5.12. The actual prediction numbers were made using p = 0.25, but the uncertainty in the prediction as determined by also making predictions at p = 0.2 and 0.3 to determine the sensitivity of the prediction to varying p. Only one alloy, CM6, was > 50 MPa from the predicted Δσy. This is not surprising considering that data on < 10 conditions was available for the f_v fit. The overall consistency is very encouraging, again considering that the ATR-2 property predictions were made from microstructure fits of a database that didn't even include ATR-2 data.

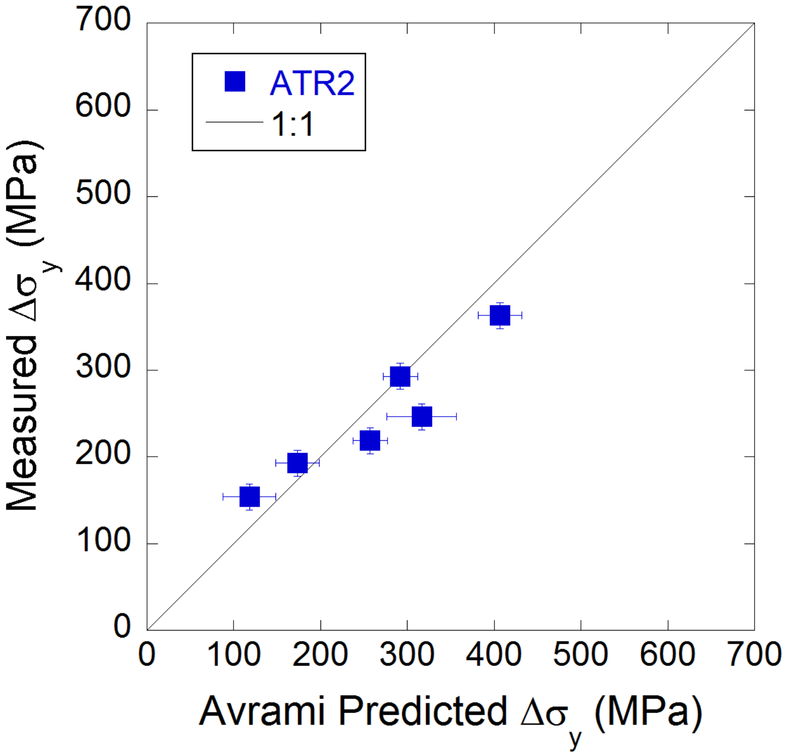

Figure 5.12. Measured vs predicted $\Delta\sigma_y$ for the ATR2 condition, where the predicted $\Delta\sigma_y$ come from the $\Delta\sigma_y(\phi t_e)$ Avrami model.

5.6 Comparisons to regulatory models

In order to compare the Avrami model with models used by the NRC (EONY) and ASTM (PE900), the $\Delta\sigma_y(\phi t_e)$ Avrami model must first be converted to $\Delta T(\phi t_e)$. This is done using a simple scaling relationship that has been established as $\Delta T=0.68\Delta\sigma_y$ [6]. The two models which will be compared to the Avrami model are the Eason-Odette-Nanstad-Yamamoto (EONY) model and the PE900 model. EONY is currently used by the NRC for failure analysis related to pressurized thermal shock. While it was statistically fit to the large surveillance ΔT database, it was motivated and structured based on an understanding of the physics leading to RPV embrittlement. On the other hand, PE900, which was recently accepted as a standard by the ASTM, is purely a statistical model that was fit to the surveillance database. As has previously been explained, EONY does not contain a term for MNSPs and because of this, significantly under predicts high ϕt_e ΔT. The PE900 model included recent surveillance data from the Ringhals reactor, which contains MNSPs at high fluence, and large corresponding ΔT. Thus, while PE900 does not explicitly treat MNSPs, it does predict significant ΔT at high ϕt_e for high Ni steels.

Figure 5.13 shows ΔT predictions for the three models compared to the UCSB test reactor database for the high Ni, Cu-free steel (CM6) and high Cu/Ni steel (LD). These EONY and PE900 plots were made using the ASTM E10 Embrittlement Database Plotter prepared by M. Erickson-Kirk [7]. The EONY model (blue lines) under predicts the high ϕt_e data for both alloys. On the other hand, while the PE900 model significantly under predicts LD at higher ϕt_e, it is reasonably accurate for the highest ϕt_e CM6 data points, though it largely over predicts at lower ϕt_e. The reason for the high accuracy of the PE900 model for CM6 is that it was directly fit to a high ϕte condition from the Ringhals reactor, which showed large f_v of MNSPs. In addition, the Ringhals RPV and CM6 have a very similar composition, which means the PE900 also fairly accurately predicts CM6 as well.

To better evaluate the accuracy of all three models, the residuals (predicted - measured ΔT) as a function of ϕt_e are shown in Figure 5.13. The left portion of the figure shows the residuals for the entire database and the right figure excludes the highest ϕte data points to better see the lower ϕt_e residuals. The Avrami model slightly under predicts at low ϕte, which was also shown in Figure 5.9, but is within ≈ 60°C to all data points at higher ϕte, while the two other models largely under predict by > 50°C. The PE900 over predicts in a few high ϕt cases, again for the CM6 steel.

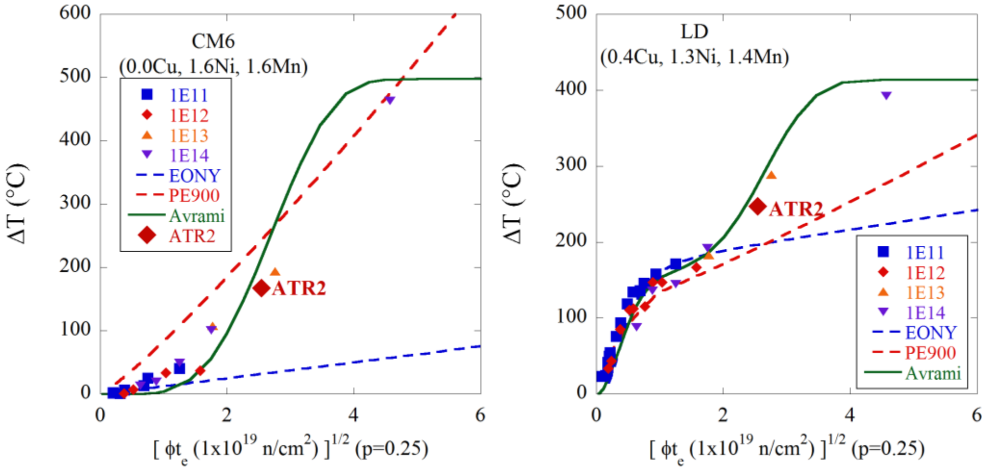

Figure 5.13. ΔT data for the high Ni, Cu-free steel (CM6-left) and high Cu/Ni steel (LD-right) compared to the three prediction models: Avrami (green), EONY (blue), PE900 (red). Note the different color data points correspond to different ϕ, with units in n/cm^2-s.

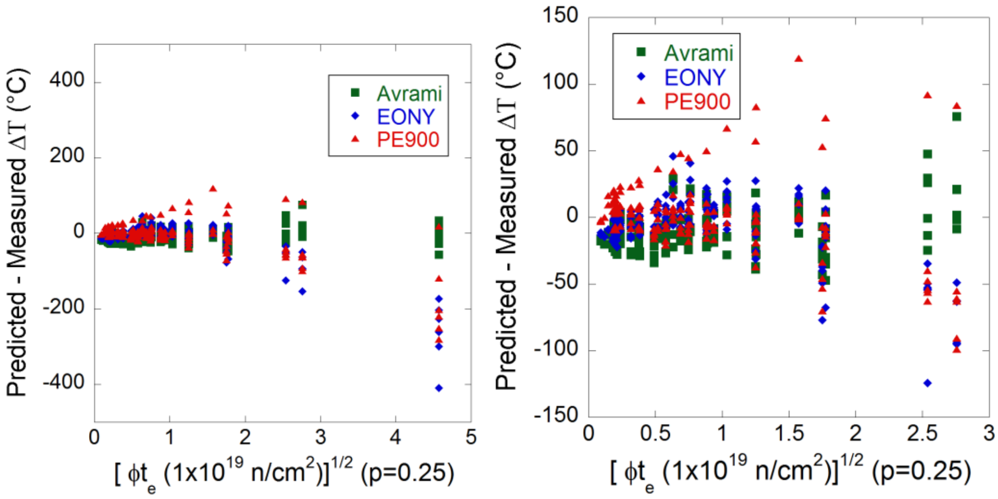

Figure 5.14. Predicted - measured ΔT vs ϕt_e for the three models: Avrami (green), EONY (blue), PE900 (red). Note that both figures show the same data, but the figure on the right is zoomed in on the lower ϕt_e data to better see the residuals.

The goodness of fit for each model was evaluated by determining the bias, or mean residual, as well as the root mean square difference for the residuals using the following equations

$$Bias = \frac{\sum_{i=1}^{n} r_i}{n} \tag{5.3}$$

$$RMSD = \sqrt{\frac{\sum_{i=1}^{n} (r_i)^2}{n}} \tag{5.4}$$

where r_i is the residual, or predicted – measured ΔT, for the i'th data point and n is the total number of data points. Essentially, the bias measures whether a given model on average over or under predicts and the RMSD measures the overall accuracy of the model. The bias and RMSD for all three models are shown in Table 5.4. These values were calculated for all data points and also for all data except the ATR1 condition, since this is the only condition past the highest expected extended life ϕt_e. The PE900 shows the smallest Bias both when including and excluding the ATR1 data. On closer inspection, the reason for the low bias is because it under predicts most all data, except CM6, which it significantly over predicts. This results in the PE900 model having the largest RMSD when excluding the ATR1 data. The EONY model has the largest RMDS when including the ATR1 data because it significantly under predicts this condition. Finally, the Avrami model has a slightly larger bias than the PE900 data, but the smallest RMSD. The bias occurs especially at low fluence, where the Avrami model largely under predicts.

Table 5.4. Bias and RMSD for the three models for all data, and for all data except ATR1.

Model	All Data		Excluding ATR1	
	Bias (MPa)	RMSD (MPa)	Bias (MPa)	RMSD (MPa)
Avrami	-10.3	20.0	-10.1	19.5
EONY	-18.1	58.5	-9.1	28.3
PE900	-7.0	48.0	-0.8	29.9

5.7 Avrami Prediction for Surveillance Data

Recent high ϕt_e surveillance data from a low Cu, high Ni weld also has shown large f_v of MNSPs and larger than expected ΔT, as has been published by other groups [8]. For further examination of the accuracy of the EONY model, data from these two reactors, Ringhals 3 and Ringhals 4, are plotted along with CM6 in Figure 5.15. The compositions for the three alloys are given in Table 5.5. The data are all plotted using the effective fluence scaling parameters established in section 5.3.1, with $\phi_r = 3\text{x}10^{11}$ n/cm^2-s and p = 0.25. Note that the Ringhals 3 ΔT at a given ϕt_e are higher than the Ringhals 4 ΔT. This is likely because Ringhals 3 has a slightly higher Cu content, which accelerates MNSP formation. Furthermore, while the CM6 model does slightly over predict near the expected end of life ϕt_e of 10^{20} n/cm^2, or 3.3 on this scale, the data falls right in line with the UCSB test reactor database. This is especially important because it confirms that the ϕ correction used to compare the high ϕ test reactor data with the much lower ϕ surveillance data on the ϕt_e scale appears to be relatively accurate. Overall, the model shows remarkable agreement and while it slightly over predicts the highest ϕt_e data, it slightly under predicts the medium ϕt_e data.

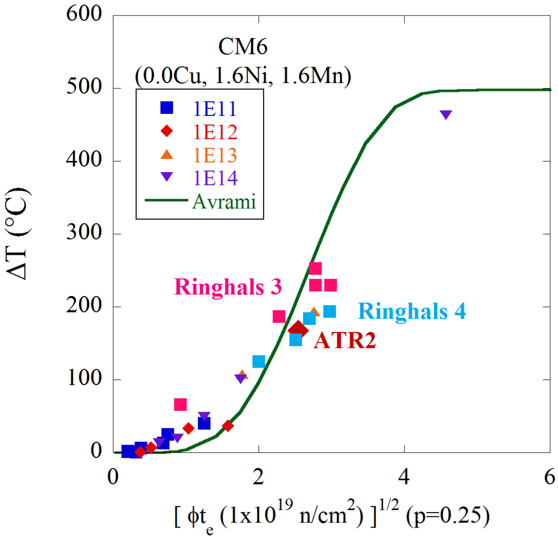

Figure 5.15. Avrami model prediction compared with CM6 data from UCSB test reactor database and data from the Ringhals surveillance program.

Table 5.5. Composition (wt.%) for the low Cu, high Ni steels shown in Figure 5.15.

Alloy	Alloy Composition (wt.%)					
	Cu	Ni	Mn	Si	P	C
CM6	0.02	1.68	1.67	0.15	0.003	0.13
Ringhals 3	0.08	1.58	1.46	0.21	0.009	0.052
Ringhals 4	0.05	1.66	1.35	0.14	0.001	0.068

5.8 *Summary and Conclusions*

The general framework for a model which can predict $\Delta T(\phi t_e)$ was proposed here. First, a general correlation between the precipitate f_v and observed $\Delta\sigma_y$ was established. Second, a simple Avrami model was presented that consists of two parts, one for CRPs and one for MNSPs. The Avrami parameters were determined through a combination of the data presented here, the physics behind the precipitation process, and a fit of the UCSB test reactor microstructural database. Following this, the $f_v(\phi t_e)$ Avrami model was converted to $\Delta\sigma_y(\phi t_e)$ using the correlation established in section 5.2. This model was shown to be fairly accurate in predicting the $\Delta\sigma_y$ from the ATR-2 condition, which was not used in the microstructure fitting. Finally, the $\Delta\sigma_y(\phi t_e)$ model was converted to $\Delta T(\phi t_e)$ to show that the residuals for the Avrami model compare favorably with models statistically fit to large ΔT databases, especially at high ϕt_e, where the other two models largely under predict ΔT.

This information is not presented to suggest that this simple Avrami model can more accurately predict ΔT than the two other models, especially because it has yet to be applied to the large surveillance ΔT database. It should also be stressed that if the EONY and PE900 models were fit using the mechanical property data shown here, they would have much smaller residuals. The main point here is that the Avrami model was fit to a *microstructure* database and converted to $\Delta\sigma_y$ using very simplified relations. The fact that the ΔT residuals are even close to the statistically fit models demonstrates the great promise in the framework presented here. Furthermore, it seems to confirm the general hypothesis that the MNSPs are intermetallic phases that can accurately be modelled using a simple phase transformation model and that the precipitates are the dominant hardening feature. Future work will focus on refining the Avrami fit parameters, and especially in determining $\phi t_{o,MNSP}$ for various alloys, with an ultimate goal of creating a model that can determine $\phi t_{o,MNSP}$ as a function of alloy chemistry, namely Cu and Ni.

5.9 References

1. Eason ED, Odette GR, Nanstad RK and Yamamoto T. "A physically based correlation of irradiation-induced transition temperature shifts for RPV steels," Oak Ridge National Lab, 2007; ORNL/TM-2006/530.
2. He MY, Odette GR, Yamamoto T and Klingensmith D. "A universal relationship between indentation hardness and flow stress", J. Nucl. Mater. 2007;367-370 A(SPEC. ISS.):556–560.
3. Odette GR, Yamamoto T and Klingensmith D. "On the effect of dose rate on irradiation hardening of RPV steels", Philos. Mag. 2005;85(4-7):779–797.
4. Porter DA, Easterling KE and Sherif MY. "Phase Transformations in Metals and Alloys" Third Edit. CRC Press, 2009.
5. Odette GR. "Radiation Induced Microstructural Evolution in Reactor Pressure Vessel Steels", Mater. Res. Soc. Symp. Proc. 1995;373:137–148.
6. Odette GR and He MY. "Cleavage toughness master curve model", J. Nucl. Mater. 2000;283-287:120–127.
7. Erickson-Kirk M. "ASTM E10 Embrittlement Database," [no date];
8. Miller MK, Powers KA, Nanstad RK and Efsing P. "Atom probe tomography characterizations of high nickel, low copper surveillance RPV welds irradiated to high fluences", J. Nucl. Mater. 2013;437(1-3):107–115.